This work was presented at the Teaching and Research Unit
Geophysical Imaging and Monitoring
of RWTH Aachen University

MASTER OF SCIENCE IN APPLIED GEOPHYSICS
RESEARCH THESIS

Minimum entropy constraints for 3D structurally-coupled joint inversion of near-surface geophysical data acquired at the Rockeskyller Kopf, Germany

Anton Hellmuth Franz Ziegon

Aachen, 1st August 2023

Minimum entropy constraints for 3D structurally-coupled joint inversion of near-surface geophysical data acquired at the Rockeskyller Kopf, Germany

MASTER OF SCIENCE THESIS

for the degree of Master of Science in Applied Geophysics
by

Anton Hellmuth Franz Ziegon

1st August 2023

IDEA LEAGUE
JOINT MASTER'S IN APPLIED GEOPHYSICS

Delft University of Technology, The Netherlands
ETH Zurich, Switzerland
RWTH Aachen, Germany

Dated: 1st August 2023

Supervisors:

Prof. Dr. Florian Wagner
Geophysical Imaging and Monitoring, RWTH Aachen University

Dr. Marc Boxberg
Geophysical Imaging and Monitoring, RWTH Aachen University

Commitee Members:

Prof. Dr. Florian Wagner
Geophysical Imaging and Monitoring, RWTH Aachen University

Dr. Marc Boxberg
Geophysical Imaging and Monitoring, RWTH Aachen University

Prof. Dr. Deyan Draganov
Applied Geophysics & Petrophysics, TU Delft

Zentrales Prüfungsamt/Central Examination Office

Eidesstattliche Versicherung
Statutory Declaration in Lieu of an Oath

Ziegon, Anton

Name, Vorname/Last Name, First Name

438469

Matrikelnummer (freiwillige Angabe)
Matriculation No. (optional)

Ich versichere hiermit an Eides Statt, dass ich die vorliegende Arbeit/Bachelorarbeit/ Masterarbeit* mit dem Titel

I hereby declare in lieu of an oath that I have completed the present paper/Bachelor thesis/Master thesis* entitled

Minimum entropy constraints for 3D structurally-coupled joint inversion of near-surface geophysical data acquired at the Rockeskyller Kopf, Germany

selbstständig und ohne unzulässige fremde Hilfe (insbes. akademisches Ghostwriting) erbracht habe. Ich habe keine anderen als die angegebenen Quellen und Hilfsmittel benutzt. Für den Fall, dass die Arbeit zusätzlich auf einem Datenträger eingereicht wird, erkläre ich, dass die schriftliche und die elektronische Form vollständig übereinstimmen. Die Arbeit hat in gleicher oder ähnlicher Form noch keiner Prüfungsbehörde vorgelegen.

independently and without illegitimate assistance from third parties (such as academic ghostwriters). I have used no other than the specified sources and aids. In case that the thesis is additionally submitted in an electronic format, I declare that the written and electronic versions are fully identical. The thesis has not been submitted to any examination body in this, or similar, form.

Aachen, 01.08.2023

Ort, Datum/City, Date

Unterschrift/Signature

*Nichtzutreffendes bitte streichen

*Please delete as appropriate

Belehrung:
Official Notification:

§ 156 StGB: Falsche Versicherung an Eides Statt

Wer vor einer zur Abnahme einer Versicherung an Eides Statt zuständigen Behörde eine solche Versicherung falsch abgibt oder unter Berufung auf eine solche Versicherung falsch aussagt, wird mit Freiheitsstrafe bis zu drei Jahren oder mit Geldstrafe bestraft.

Para. 156 StGB (German Criminal Code): False Statutory Declarations

Whoever before a public authority competent to administer statutory declarations falsely makes such a declaration or falsely testifies while referring to such a declaration shall be liable to imprisonment not exceeding three years or a fine.

§ 161 StGB: Fahrlässiger Falscheid; fahrlässige falsche Versicherung an Eides Statt

(1) Wenn eine der in den §§ 154 bis 156 bezeichneten Handlungen aus Fahrlässigkeit begangen worden ist, so tritt Freiheitsstrafe bis zu einem Jahr oder Geldstrafe ein.

(2) Straflosigkeit tritt ein, wenn der Täter die falsche Angabe rechtzeitig berichtigt. Die Vorschriften des § 158 Abs. 2 und 3 gelten entsprechend.

Para. 161 StGB (German Criminal Code): False Statutory Declarations Due to Negligence

(1) If a person commits one of the offences listed in sections 154 through 156 negligently the penalty shall be imprisonment not exceeding one year or a fine.

(2) The offender shall be exempt from liability if he or she corrects their false testimony in time. The provisions of section 158 (2) and (3) shall apply accordingly.

Die vorstehende Belehrung habe ich zur Kenntnis genommen:
I have read and understood the above official notification:

Aachen, 01.08.2023

Ort, Datum/City, Date

Unterschrift/Signature

All Python scripts and figures available under:
https://github.com/ZiegAnt/APG-MSc-Project-Ziegon.
Access can be requested at: anton.ziegon@rwth-aachen.de.

Abstract

Geophysical methods are widely used to gather information about the subsurface as they are non-intrusive and comparably cheap during acquisition, however, the solution to the geophysical inverse problem is inherently non-unique which introduces considerable uncertainties. Therefore, independently acquired geophysical data sets can be jointly inverted to reduce ambiguities in the resulting multi-physical subsurface images. Zhdanov et al. (2022) introduce a novel cooperative inversion approach using joint minimum entropy constraints in the regularization term of the objective functionals to create more consistent multi-physical images with sharper boundaries. Here, this approach is implemented in an open-source software and its applicability on electrical resistivity tomography (ERT), seismic refraction tomography (SRT) and magnetic data is investigated. A synthetic 2D ERT and SRT data study is used to demonstrate the approach and to investigate the influence of the governing parameters. The findings showcase the advantage of the joint minimum entropy (JME) stabilizer over separate, conventional smoothness-constrained inversions. The method is then used to analyze field data from Rockeskyller Kopf, Germany. 3D ERT and magnetic data is combined and results confirm the expected volcanic diatreme structure with improved details. The multi-physical images of both methods are consistent in some regions as similar boundaries are produced in the resulting models, which have been lacking in previous studies. Because of its sensitivity to hydrologic conditions in the subsurface, observations suggest that the ERT method senses different structures than the magnetic method. However, these structures in the ERT result do not seem to be enforced on the magnetic susceptibility distribution, showcasing the flexibility of the approach. Both investigations outline the importance of a suitable parameter and reference model selection for the performance of the approach and suggest careful parameter tests prior to the joint inversion. With proper settings, the JME inversion is a promising tool for geophysical imaging, however, this thesis also lists some objectives for future studies and additional research to explore and optimize the method.

Acknowledgments

I would like to thank Prof. Dr. Florian Wagner and Dr. Marc Boxberg for the great supervision and guidance throughout my thesis. I really appreciate the time they took to help me if I was stuck and and all ideas that they contributed to the work. Additionally, I thank Florian Wagner for making the LaTeX template of this thesis available at https://github.com/florian-wagner/thesis-tex-template, and Marc Boxberg for making the field data available from his time at RUB.

In addition, I would like to express my gratitude towards the PhD members of the GIM, namely Andrea Balza Morales, Nino Menzel, and Hagen Söding for helping with pyGIMLi bugs, giving me feedback on my writing and guiding me through the theory of joint minimum entropy stabilizers. Of course I am also thankful for all lunch dates that helped me to reset my energy after many hours of heavy thinking and debugging.

Last, I would like to thank my fellow AGP students (Brianna Mueller, Tomasz Gluzinski, Simone Probst, Marilina Valatsou, Nadja Lindner, Thomas Simader) in Aachen alongside all GIM members (including Sofia Brisson) for making this important and partly stressful semester so enjoyable and memorable.

Contents

List of Figures

List of Tables

List of Symbols

$\lvert\cdot\rvert$	Absolute value (eq. 2.27)
$\lVert\cdot\rVert$	Euclidean norm (eq. 2.6)
$\times$	Cross product (eq. 2.1)
α	Smoothing factor (see Listing 3.2)
β	Numerical stabilizer (eq. 2.31)
χ^2	Measure of error weighted data misfit functional (eq. 2.18)
$\mathbf{c}$	Cell size vector (eq. 3.2)
$\mathbf{d}$	Data vector (eq. 2.4)
$\mathbf{d}_{\text{obs}}$	Observed data vector (eq. 2.5)
$\mathbf{d}_{\text{pre}}$	Predicted model vector (eq. 2.5)
$\text{diag}(\cdot)$	Diagonal matrix (eq. 2.16)
δ	Standard deviation (eq. 2.16)
$\mathscr{F}$	Forward operator (eq. 2.4)
$\mathbf{\Gamma}$	Residuals (eq. 2.5)
H	Entropy (eq. 2.25)
$\overrightarrow{H}$	Magnetic field (eq. 2.3)
I	Strength of electrical current (eq. 2.1)
$\overrightarrow{I}$	Electrical current vector (eq. 2.1)
$\mathbf{J}$	Jacobian matrix (eq. 2.11)
K	Geometrical factor (eq. 2.1)
k	Step size of Gauss-Newton update (eq. 2.15)
κ	Relative magnetic susceptibility. (eq. 2.3)
λ	Regularization parameter (eq. 2.20)
$\overrightarrow{M}$	Total magnetization (eq. 2.3)
$\overrightarrow{M}_{\text{ind}}$	Induced magnetization (eq. 2.3)
$\overrightarrow{M}_{\text{rem}}$	Remanent magnetization (eq. 2.3)
$\mathbf{m}$	Model vector (eq. 2.4)
$\mathbf{m}_0$	Starting model (eq. 2.8)
$\mathbf{m}_{\text{est}}$	Estimated model vector (eq. 2.5)
$\mathbf{m}_{\text{ref}}$	Reference model (eq. 2.20)
$\Delta\mathbf{m}$	Model update (eq. 2.8)
$\frac{\partial}{\partial \mathbf{m}}$	Partial derivative w.r.t. model parameters (eq. 2.7)
mw	Method weighting factor (see Listing 3.2)
$\mathscr{N}$	Number of data points (eq. 2.18)
∇	Gradient (eq. 2.1)
$\mathscr{O}$	Order of residual (eq. 2.11)
Ω	Model space (eq. 2.27)
ω_{qME}	Min. entropy weights of order q, diagonal of $\mathbf{W}_{\text{e}}$ (eq. 2.42)

ω_{qMEG}	Min. entropy gradient weights of order q, diagonal of $\mathbf{W}_{\mathrm{e}}$ (eq. 2.43)
ω_{qJME}	Joint min. entropy weights of order q, diagonal of $\mathbf{W}_{\mathrm{e}}$ (eq. 2.42)
ω_{qJMEG}	Joint min. entropy gradient weights of order q, diagonal of $\mathbf{W}_{\mathrm{e}}$ (eq. 2.43)
p	Probability density function (eq. 2.25)
p_{m}	Pseudo probability density function (eq. 2.27)
ϕ	Parametric functional (eq. 2.20)
ϕ_{d}	Data misfit functional (eq. 2.5)
ϕ_{dw}	Error weighted data misfit functional (eq. 2.17)
ϕ_{J}	Joint parametric functional (eq. 2.35)
ϕ_{JE}	Joint entropy parametric functional (eq. 2.46)
ϕ_{m}	Model misfit functional (eq. 2.20)
Q	Normalization factor related to some p_{m} (eq. 2.27)
q	Order of entropy expression (eq. 2.31)
$\mathbf{r}$	Point in space (eq. 2.1)
ρ_{app}	Apparent electrical resistivity (eq. 2.2)
S	Stabilizer (eq. 2.30)
S_{J}	Joint stabilizer (eq. 2.35)
S_{qME}	Min. entropy stabilizer of order q (eq. 2.31)
S_{qMEG}	Min. entropy gradient stabilizer of order q (eq. 2.33)
S_{qJME}	Joint min. entropy stabilizer of order q (eq. 2.36)
S_{qJMEG}	Joint min. entropy gradient stabilizer of order q (eq. 2.38)
σ	Electrical conductivity (eq. 2.1)
$\mathscr{T}$	Finite alphabet (eq. 2.25)
$T[\cdot]$	Transform (eq. 2.29)
$\cdot^T$	Transposed matrix or vector (eq. 2.7)
t	Element of a finite alphabet $\mathscr{T}$ (eq. 2.25)
τ	Cross-gradient functional (eq. 2.24)
U	Electrical potential (eq. 2.1)
ΔU	Electrical potential difference (eq. 2.2)
$\mathbf{W}_{\mathrm{d}}$	Data weighting matrix (eq. 2.16)
$\mathbf{W}_{\mathrm{m}}$	Regularization matrix (eq. 2.20)
$\mathbf{W}_1$	First-order finite-difference operator (eq. 2.21)
$\mathbf{W}_2$	Second-order finite-difference operator (eq. 2.21)
$\mathbf{W}_{\mathrm{e}}$	Entropy weighting matrix (eq. 2.40)
w_{e}	Model weights, inside integral (eq. 2.40)

1

Introduction

Contents

This chapter presents the importance and the challenges of geophysical imaging techniques and introduces the role of joint inversion approaches in this context (Section 1.1. Section 1.2 states the motivation and Section 1.3 outlines the frame of this work and presents its structure.

1.1 Geophysical imaging

The imaging of the subsurface is an important task in many fields of research including structural geology, geohazards, hydrology, resource exploration, or even forensics. Geophysical methods have been proven to be an invaluable tool for this purpose as they provide a non-invasive and comparably inexpensive way to gather information about the subsurface. Depending on the target, some methods might be more beneficial. An overview of commonly used geophysical methods with suggested applications is presented in Table 1.1. While passive, natural field methods like gravity, magnetics, or magnetotellurics are widely used for large scale and deep investigations of the interior of the Earth, active methods are commonly applied for local studies that require higher resolutions (Lowrie and Fichtner, 2020; Kearey et al., 2002). The geophysical community even presented adapted geophysical imaging techniques for medical imaging (Marty et al., 2021) or building integrity tests (Maack et al., 2022) that were able to resolve very small objects on the cm scale.

Table 1.1: Overview of geophysical methods with the respective physical properties that they are sensitive to (Kearey et al., 2002).

Method	Physical property	Possible Applications
Active		
Seismic	Seismic velocities (depending on density, elastic moduli)	Exploration for fossil fuels Glacial studies
Electrical resistivity	Electrical conductivity	Hydrologic investigations Permafrost studies
Induced polarization	Electrical capacitance	Engineering investigations Mineral exploration
Electromagnetics (FEM, TEM, EMI)	Electrical conductivity Inductance	Archaeology Hydrologic investigations
Ground penetrating radar	Dielectric constant Electrical conductivity	Archaeology Engineering investigations
Passive		
Gravity	Density	Bedrock depth investigations Mineral exploration
Magnetics	Magnetic susceptibility Magnetic remanence	Archaeology Mineral exploration
Electromagnetics (MT)	Electrical conductivity	Mineral exploration

Table 1.1 illustrates the versatility of geophysical methods which make them essential for many applications. Improving geophysical imaging techniques is therefore of great importance for the technical advances in many fields. However, geophysical methods have the drawback that they are generally prone to ambiguities, meaning there are several geophysical models that explain the data within their uncertainty arising from the inherent non-uniqueness of the inverse problem (Zhdanov, 2015; Menke, 2018). Noise and human errors during data acquisition in addition to assumptions and simplifications in the modelling and inversion frameworks introduce further uncertainties that might make interpretation of the results more difficult and less reliable (Kearey et al., 2002). To counteract ambiguity, it is common practice to combine different geophysical methods in a joint interpretation. Even though different geophysical methods sense the same subsurface features, the resulting images might indicate different structures. To address this issue, several approaches have been developed that couple several geophysical methods during the data inversion rather than in the interpretation phase. These joint inversion schemes are able to produce more consistent geophysical models as ambiguities during the data inversion are reduced by the enforcement of petrophysical or structural relationships (e.g. Gallardo and Meju (2004); Gallardo et al. (2005); Gallardo (2007); Moorkamp et al. (2011, 2016); Skibbe et al. (2021); Steiner et al. (2021)). However, the coupling of different geophysical methods is generally non-trivial and requires complex physical and mathematical formulations along with additional computational power. Due to the advances in high performance computing in the recent decade, the latter is no longer the obstacle (Wagner and Uhlemann, 2021; Moorkamp et al., 2016; Zhdanov, 2015). Wagner and Uhlemann (2021) and Moorkamp et al. (2016) give an extensive overview of the most common joint inversion approaches with a multitude of synthetic and field data examples.

One of the latest advances in the field of geophysical joint inversion is presented by Zhdanov et al. (2022), who introduce a structural coupling based on joint minimum entropy formulations. The authors demonstrate the new scheme in the context of magnetic and gravity data for large scale mineral exploration purposes with very promising results. However, since the magnetic and gravity methods are inherently ambiguous and have comparably low resolution, they are less common for small scale, near-surface applications. A validation of this approach in a more local context using seismic, electric or electromagnetic methods is yet to be presented.

1.2 Motivation

This work will use an implementation of the joint minimum entropy inversion approach (Zhdanov et al., 2022) to evaluate the concept using electrical resistivity tomography (ERT), seismic refraction tomography (SRT) as well as magnetics.

This will give insight in the applicability of this structural coupling approach for multi-physical imaging with non-potential field methods involved and therefore will make the approach more accessible for a wide range of applications. Ultimately, the findings of this project will contribute to the establishment of joint minimum entropy inversion in the toolbox of geophysical imaging techniques.

Besides the methodological aspect of this work, the method will be applied to a field data set consisting of ERT and magnetic data acquired at the Rockeskyller Kopf, Eifel, Germany. Several near-surface data sets were collected with the objective to image a possible volcanic diatreme structure. Multiple studies evaluated and interpreted individual data sets (Eilhard, 2009; Hauburg, 2016; Boxberg, 2011; Mues, 2013; Schneider, 2017; Plumpe, 2015; Gilberti, 2020). However, obtained subsurface images are not fully consistent with each other. Using this field data, the joint minimum entropy implementation will be tested. Furthermore, possible improvements of the imaging through the joint inversion of several data sets will be investigated.

To conclude this section the explicit research questions are presented in the list below:

- Can the approach be reproduced within the open-source library pyGIMLi (Rücker et al., 2017)?
- Can the joint minimum entropy approach be generalized for the ERT and SRT method?
- What are the challenges of the implementation?
- Can the approach be used to obtain more consistent multi-physics subsurface models at Rockeskyller Kopf?

1.3 Structure of this thesis

This thesis aims to investigate the applicability of the joint minimum entropy inversion approach in the context of near-surface geophysical methods. A short introduction to the theory of ERT, SRT and magnetics is given in section Section 2.1 (Geophysical methods) as these methods will be used for the demonstration of the approach in the subsequent chapters. Chapter 2 (Theory) introduces the underlying inversion theory as used in the code by Rücker et al. (2017) (section 2.2) as well as an overview of geophysical joint inversion techniques with a focus on the joint minimum entropy approach described by Zhdanov et al. (2022) (section 2.3). Chapter 3 (Method) presents the implementation of the joint minimum entropy approach within the open-source library pyGIMLi along with some simple illustrations of the methods to clarify the concept. Chapter 4 (Synthetic study) presents a synthetic 2D model study using ERT and SRT data to demonstrate the joint inversion scheme and investigate the effects of the governing parameters.

In Chapter 5 (Field study: Rockeskyller Kopf) the new method is used to improve subsurface imaging of a volcanic diatreme structure at the Rockeskyller Kopf in Rheinland-Pfalz, Germany. 3D ERT measurements are jointly inverted with a previously acquired magnetic data set to test the approach with field data. Note that pyGIMLi standard forward and inverse calculations are not discussed in this work. More detailed descriptions are provided in (Rücker et al., 2017).

All results and findings are evaluated and discussed in Chapter 6 (Discussion) and summarized in Chapter 7 (Conclusions and Outlook). The latter also provides concluding answers to the research questions as well as a short outlook for further developments and improvements.

2

Theory

Contents

This chapter gives a short overview over the theory behind the ERT, SRT and magnetic methods (2.1). It presents the non-linear inversion scheme, namely the Gauss-Newton method, and its extension to data weighting and regularization (2.2). A short overview of different joint inversion approaches is given with a focus on structural coupling approaches and a detailed presentation of structurally coupled joint inversion with joint entropy stabilizers (2.3).

2.1 Geophysical methods

On the following pages an overview of the basic theory behind the geophysical methods that are used in this study is presented. For the forward modelling the open-source library pyGIMLi is used and the details of the exact modelling procedures are not presented in this work but they can be found in Rücker et al. (2017) and Günther et al. (2006).

2.1.1 Electrical resistivity tomography (ERT)

Electrical resistivity tomography (ERT) is a geophysical method that injects a direct current into the ground using two electrodes and recovers the subsurface electrical resistivity distribution by measuring the differences in the electrical potential between two other electrodes. Therefore, this method can be used to detect changes in clay content or fluid saturation as well as any other phenomenon that involves a change in electrical resistivity (Kearey et al., 2002). Since the current injecting electrodes can be assumed as point sources they are also referred to as the current dipole. The electrical potential U is then described at any location in space with the Poisson equation:

$$\nabla\left[\sigma\left(\mathbf{r}\right)\nabla U\left(\mathbf{r}\right)\right] = -\nabla\overrightarrow{I}. \tag{2.1}$$

Here, r stands for the location, J for the injected electrical current, and σ for the electrical conductivity which is the inverse of the electrical resistivity ρ. Using eq. 2.1 in combination with an appropriate modelling software, the electrical potential at any place within the model discretization and the resulting potential differences between two electrode locations can be determined for each current injecting dipole (Johnson and Wellman, 2015). It is common use to transfer the potential differences ΔU between the two measurement locations M and N into apparent resistivities ρ_{app} according to Kearey et al. (2002):

$$\rho_{\text{app}} = \frac{2\pi}{\frac{1}{\overline{AM}} - \frac{1}{\overline{AN}} - \frac{1}{\overline{BM}} + \frac{1}{\overline{BN}}}\frac{\Delta U}{I} = K\frac{\Delta U}{I}. \tag{2.2}$$

I stands for the strength of the injected electrical current between the locations A and B. $\overline{AM}$ refers to the distance between an injection point, A, and a measurement point, M. The factor related to the acquisition geometry is called the geometrical factor K. As seen in eq. 2.1, the electrical potential is related to the subsurface resistivity structure and therefore the observed potential differences (or apparent resistivities) can be inverted using a non-linear inversion scheme to reconstruct the subsurface resistivity distribution. The inversion of the data will be explained in more detail in section 2.2. Within this work only dipole-dipole electrode configurations (Figure 2.1) are used. The current injecting dipole and the potential measuring dipole are located along a line next to each other with a certain dipole length a and some dipole separation that is a multiple n of the dipole length. This electrode configuration is beneficial as it allows for parallelization of the potential measurements for one injection dipole and therefore reduces acquisition time if the measurement device is a multi-channel instrument. Furthermore, the dipole-dipole configuration is more sensitive to lateral resistivity variations. However, it is less robust than other configurations as measurements of long dipole separation might be heavily affected by noise and therefore have a low signal-to-noise ratio (SNR) (Okpoli et al., 2013).

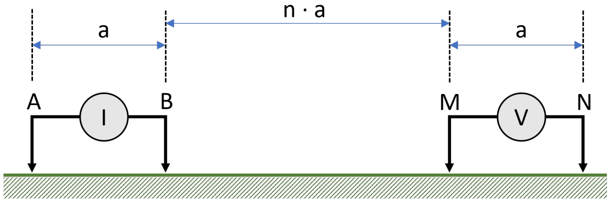

Figure 2.1: Sketch of dipole-dipole array. I denotes the current injecting dipole consisting of electrodes A and B, V represents the potential measuring dipole consisting of electrodes M and N. a indicates the dipole length and n is referred to as the level of the measurement.

2.1.2 Seismic refraction tomography (SRT)

Seismic refraction tomography (SRT), often called traveltime tomography, is a seismic method that uses times that a seismic wave needs to travel from a seismic source to a receiver to reconstruct the velocity structure of the subsurface. For a homogeneous subsurface, waves would solely travel along the surface if sources were located at the surface and the SRT method could not be performed successfully. In order to produce seismic refraction, the subsurface needs an increased velocity with increasing depth (see Figure 2.2). In such a case waves are travelling faster in the deeper high-velocity medium than the waves along the surface in the relative low-velocity medium. At the cross-over distance (x_{cros}) the refracted wave that travelled in the high-velocity medium reaches the receiver before the direct arrival. Therefore, the first arrival picks hold information about the refracted waves and can be used to invert travel times into a velocity structure Kearey et al. (2002). It is important to mention that low-velocity structures below a high-velocity medium are not recognized in the refracted wave as the faster path is through the high-velocity medium. This phenomenon is called *hidden layer* and introduces a limitation to the SRT method (Gupta, 1977). Since the raypaths are generally bending towards high-velocity regions and avoid low-velocity structures the SRT method is a non-linear problem. Therefore, data inversion requires the scheme described in section 2.2.

2.1.3 Magnetics

Convective movement in the generally electrically conductive outer core of the Earth produces a strong magnetic field. Due to the influence of magnetizations in the subsurface, variations of the Earth's magnetic field can be observed at the surface. In general, the magnetization M of a rock can be described as the sum of its remanent magnetization M_{rem} and the induced magnetization M_{ind} and can therefore be expressed as (Lowrie and Fichtner, 2020):

$$\vec{M} = \vec{M}_{rem} + \vec{M}_{ind} = \vec{M}_{rem} + \kappa \vec{H}. \tag{2.3}$$

Here, $\vec{H}$ represents the Earth's magnetic field and κ the relative magnetic susceptibility. As the remanent magnetization is generally much smaller than $\vec{M}_{ind}$, the relative magnetic susceptibility

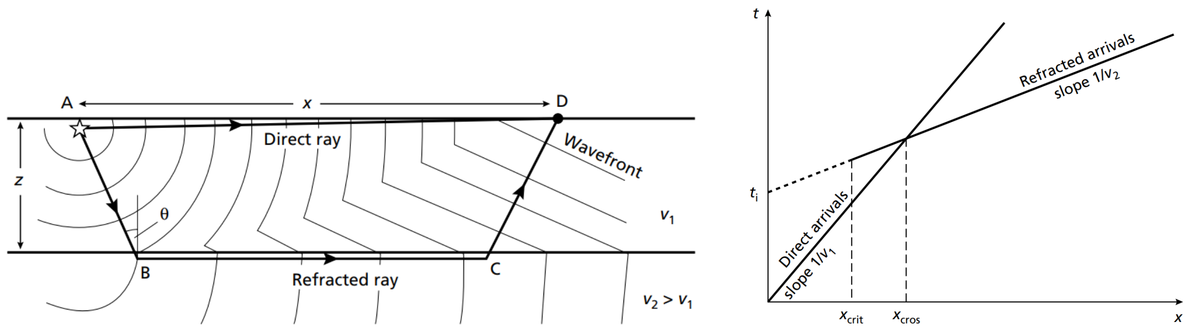

(a) Sketch of the principle of seismic refraction.

(b) Schematic t-x-diagram.

Figure 2.2: Sketch illustrating the principle of seismic refraction. (a) shows the seismic wave propagation with the ray path of the direct and refracted wave. The corresponding traveltimes are presented in (b) in a t-x-diagram. x_{cros} refers to teh cross-over distance, while x_{crit} describes the distance, where the critically reflected wave appears (Kearey et al., 2002).

κ is the main physical property that creates a significant anomaly. Even though most minerals are non-magnetic ($\kappa \approx 0$), some sedimentary rocks contain enough ferrous minerals like hematite or magnetite such that their magnetic susceptibility produces a significant magnetic anomaly. As seen in Figure 2.3, the biggest natural magnetic permeabilities are occurring in igneous rocks (Hinze et al., 2013; Lowrie and Fichtner, 2020; Kearey et al., 2002). To measure the magnetic field, a proton magnetometer is used which exploits the spiralling of hydrogen nuclei around the direction of the magnetic field. With a coil, the frequency of the spiraling protons can be determined which is directly related to the external magnetic field strength. Note that the ionospheric influence usually introduces temporal changes that affect magnetic field observations. Therefore, a suitable correction of the temporal variations typically has to be performed before using the data set (Kearey et al., 2002).

The magnetic field is often characterized by the total field intensity F, the field declination D and the field inclination I. The declination refers to the angle between the horizontal direction of the field and the direction of true north. The inclination states the angle between the field and its horizontal component. These parameters are important as the direction of the Earth's magnetic field has strong influence on the shape of the resulting magnetic anomaly which makes them crucial for forward and inverse modelling. Like the gravity method, the magnetic method is a potential field method which makes it a highly non-unique problem. This means that, for example, a deeper structure with a strong magnetic susceptibility contrast with respect to the background has a very similar response than a shallow, low-contrast anomaly. This means that additional constraints in the inversion process are needed in order to infer a subsurface model based on some magnetic field observations (Kearey et al., 2002; Hinze et al., 2013; Lowrie and Fichtner, 2020).

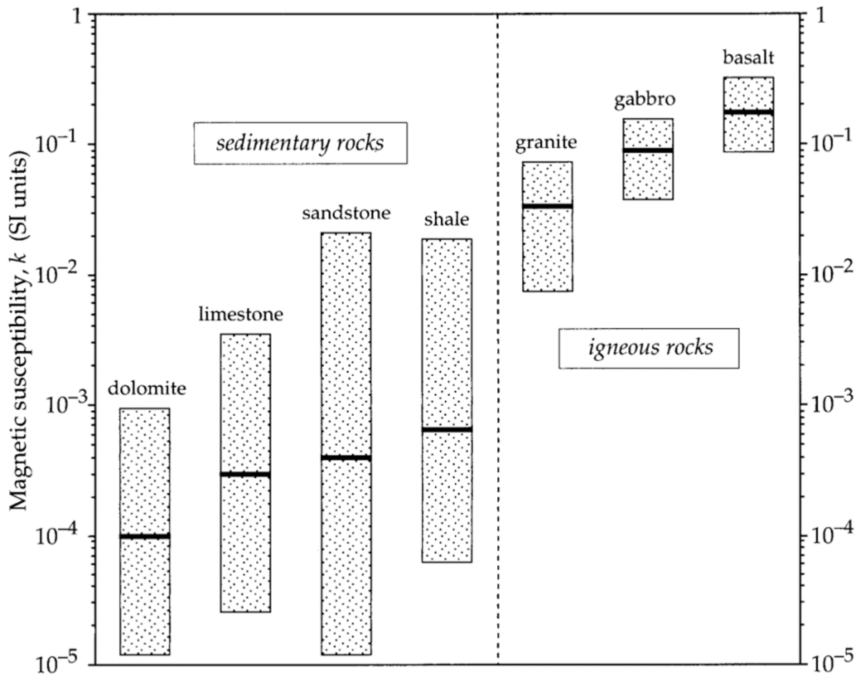

Figure 2.3: Mean values and ranges of magnetic susceptibility for the major sedimentary and igneous rocks (Lowrie and Fichtner, 2020).

2.2 Non-linear inversion

2.2.1 Inverse problem formulation

The basis for all geophysical inverse problems is the formulation of the forward problem. Consider a forward operator $\mathscr{F}$ and a finite amount of model parameters in a discrete space $\mathbf{m}$. The geophysical forward problem is then described as

$$\mathbf{d} = \mathscr{F}(\mathbf{m}). \tag{2.4}$$

Here, $\mathbf{d}$ represents the data vector containing the observations based on the model vector $\mathbf{m}$ and the forward operator $\mathscr{F}$. The goal of inversion is to find a set of model parameters $\mathbf{m}_{\text{est}}$ that explains the observed data $\mathbf{d}_{\text{obs}}$ which means that the norm of the residual vector **res** should be minimized. The residuals are described with the following relationships:

$$\Gamma = \mathbf{d}_{\text{pre}} - \mathbf{d}_{\text{obs}} = \mathscr{F}(\mathbf{m}_{\text{est}}) - \mathbf{d}_{\text{obs}}. \tag{2.5}$$

$\mathbf{d}_{\text{pre}}$ is the predicted data that results from the set of model parameters $\mathbf{m}_{\text{est}}$. Using eq. 2.5 the misfit functional ϕ_{d} can be defined as the square of the L2-norm of the residual vector:

$$\phi_{\text{d}} = ||\Gamma||^2 = \sum_i \Gamma_i^2 = (\mathscr{F}(\mathbf{m}_{\text{est}}) - \mathbf{d}_{\text{obs}})^T \; (\mathscr{F}(\mathbf{m}_{\text{est}}) - \mathbf{d}_{\text{obs}}) = \min. \tag{2.6}$$

ϕ_d is also often referred to as the data objective functional and is the central piece of every inversion algorithm. As the minimum of the objective function is defined through a derivative of zero, the solution of the inverse problem can be found by the following expression:

$$\frac{\partial}{\partial \mathbf{m}}(\phi_\mathrm{d}) = \frac{\partial}{\partial \mathbf{m}}\left[(\mathscr{F}(\mathbf{m}_\mathrm{est}) - \mathbf{d}_\mathrm{obs})^T \; (\mathscr{F}(\mathbf{m}_\mathrm{est}) - \mathbf{d}_\mathrm{obs})\right] \stackrel{!}{=} 0. \tag{2.7}$$

If the forward operator is linear, eq. 2.6 will simplify to matrix-vector multiplications and the least-squares (LSQR) solution can be found through simple variational calculus. However, most geophysical methods are non-linear problems and can, therefore, not be solved that simple. As the methods that are used in this work are subject to non-linear problems, the solution of linear inverse problems will not be discussed any further.

There are different approaches that can be used for the quadratic optimization problem described by eq. 2.7, namely local and global optimization methods. The latter usually requires significantly more computational resources and is therefore less common. Usually, local optimization methods based on gradients are used such as the steepest decent method or the conjugate gradient method. These methods aim at solving the inverse problem iteratively (Menke, 2018; Zhdanov, 2015). For all data inversions in this work, the inversion framework within the Python open-source library pyGIMLi is used. Since pyGIMLi uses the Gauss-Newton method for the optimization problem (Rücker et al., 2017), this non-linear inversion approach will be discussed in more detail in the following section.

2.2.2 Gauss-Newton method

The motivation behind the Gauss-Newton Method is to find the iterative solution in one step. Consider some starting model $\mathbf{m}_0$ and the model update $\Delta\mathbf{m}$ to obtain the solution $\mathbf{m}_1$ that explains the observed data $\mathbf{d}_\mathrm{obs}$ such that

$$\mathbf{m}_1 = \mathbf{m}_0 + \Delta\mathbf{m}. \tag{2.8}$$

Note that the subscript of $\mathbf{d}_\mathrm{obs}$ is dropped from now on to make the equations clearer. The misfit functional is then given as

$$\phi_\mathrm{d} = (\mathscr{F}(\mathbf{m}_0 + \Delta\mathbf{m}) - \mathbf{d})^T \; (\mathscr{F}(\mathbf{m}_0 + \Delta\mathbf{m}) - \mathbf{d}) = \min. \tag{2.9}$$

Similar to eq. 2.7, the model update $\Delta\mathbf{m}$ is then found by taking the first derivative of ϕ_d with respect to $\Delta\mathbf{m}$:

$$\begin{aligned}\frac{\partial}{\partial \Delta\mathbf{m}}(\phi_\mathrm{d}) &= \frac{\partial}{\partial \Delta\mathbf{m}}\left[(\mathscr{F}(\mathbf{m}_0 + \Delta\mathbf{m}) - \mathbf{d})^T \; (\mathscr{F}(\mathbf{m}_0 + \Delta\mathbf{m}) - \mathbf{d})\right] \\ &= 2\left(\frac{\partial}{\partial \Delta\mathbf{m}}(\mathscr{F}(\mathbf{m}_0 + \Delta\mathbf{m}))^T \; (\mathscr{F}(\mathbf{m}_0 + \Delta\mathbf{m}) - \mathbf{d})\right) \\ &\stackrel{!}{=} 0.\end{aligned} \tag{2.10}$$

To simplify the relation above, a first order Taylor expansion is used to approximate the non-linear operator $\mathscr{F}$. This is shown in eq. 2.11:

$$\mathscr{F}(\mathbf{m}_0 + \Delta\mathbf{m}) = \mathscr{F}(\mathbf{m}_0) + \mathbf{J}\Delta\mathbf{m} + \mathscr{O}\left(\Delta\mathbf{m}^2\right), \quad \text{with} \quad \mathbf{J} = \left\|\frac{\partial \mathscr{F}(\mathbf{m}_0)_i}{\partial m_j}\right\|. \tag{2.11}$$

Note that $\mathbf{J}$ is the Jacobian matrix which contains partial derivatives for all predicted data $\mathscr{F}(\mathbf{m}_0)$ with respect to all model parameters. $\mathscr{O}$ indicates a truncation of the Taylor expansion for terms of second-order or higher. Inserting eq. 2.11 into eq. 2.10 results in the following expression:

$$0 = \mathbf{J}^T(\mathscr{F}(\mathbf{m}_0) - \mathbf{d}) + \mathbf{J}^T\mathbf{J}\Delta\mathbf{m}. \tag{2.12}$$

The model update $\Delta\mathbf{m}$ is then obtained by

$$\Delta\mathbf{m} = \left(\mathbf{J}^T\mathbf{J}\right)^{-1}\mathbf{J}^T(\mathscr{F}(\mathbf{m}_0) - \mathbf{d})]. \tag{2.13}$$

Since eq. 2.11 is only a first order approximation of the non-linear forward operator $\mathscr{F}$, the solution is not obtained after one single iteration. Several iterations are needed to obtain a set of model parameters that explains the observed data (Loke and Dahlin, 2002; Rücker et al., 2017; Menke, 2018; Zhdanov, 2015). Therefore, the Gauss-Newton method can be summarized in the following iterative scheme:

$$\mathbf{m}_{n+1} = \mathbf{m}_n + \Delta\mathbf{m}_n = \mathbf{m}_n + \left(\mathbf{J}^T\mathbf{J}\right)^{-1}\mathbf{J}^T(\mathscr{F}(\mathbf{m}_n) - \mathbf{d}). \tag{2.14}$$

To improve the convergence of the Gauss-Newton method, it is also possible to multiply the model update $\Delta\mathbf{m}_n$ with an additional factor k_n. k_n is referred to as the step size and is defined as shown in eq. 2.15 (Zhdanov, 2015):

$$k_n = \frac{\Delta\mathbf{m}_n^T\mathbf{J}^T(\mathscr{F}(\mathbf{m}_n) - \mathbf{d})}{||\mathbf{J}_n\Delta\mathbf{m}_n||^2}. \tag{2.15}$$

2.2.2.1 Weighted Newton method

In practice, all observations are contaminated by some error. In that case, more accurate data should have a higher influence on the misfit functional than measurements with larger errors. Therefore, it is useful to introduce weighting factors w_i for each observation d_i. The data weighting matrix $\mathbf{W}_\mathrm{d}$ can then be defined as:

$$\mathbf{W}_\mathrm{d} = \mathrm{diag}(w_i) = \mathrm{diag}\left(\frac{1}{\delta_i}\right) \tag{2.16}$$

As seen in the equation above, the data weighting matrix is a diagonal matrix containing the individual weights. Intuitively, it makes sense to use the reciprocal of the standard deviations δ_i (i.e., the measurement errors) for the data weighting. Therefore, $\mathbf{W}_\mathrm{d}$ is also called the data covariance. It can be easily incorporated into the misfit functional in eq. 2.6, 2.9 and 2.12 as shown exemplary for eq. 2.6:

$$\phi_{\mathrm{dw}} = (\mathscr{F}(\mathbf{m}) - \mathbf{d})^T \mathbf{W}_{\mathrm{d}}^T \mathbf{W}_{\mathrm{d}} (\mathscr{F}(\mathbf{m}) - \mathbf{d}) = \min. \tag{2.17}$$

$$\chi^2 = \frac{\phi_{\mathrm{dw}}}{\mathscr{N}}. \tag{2.18}$$

ϕ_{d} is a more powerful data misfit functional as ϕ_{d} since data accuracy is also taken into account. It is commonly also quantified through χ^2 which is the error weighted misfit functional divided by the number of data points $\mathscr{N}$. Combining eq. 2.17 with eq. 2.10 and 2.11 results in the following expression of the weighted Gauss-Newton model update (Menke, 2018; Zhdanov, 2015):

$$\Delta \mathbf{m}_n = \left(\mathbf{J}^T \mathbf{W}_{\mathrm{d}}^T \mathbf{W}_{\mathrm{d}} \mathbf{J}\right)^{-1} \mathbf{J}^T \mathbf{W}_{\mathrm{d}}^T \mathbf{W}_{\mathrm{d}} (\mathscr{F}(\mathbf{m}_n) - \mathbf{d}). \tag{2.19}$$

2.2.2.2 Regularized Newton method

The Newton method as it is defined in eq. 2.14 might not be applicable as the inverse of the matrix $\mathbf{J}^T \mathbf{J}$ might not exist or it might be ill conditioned. In geophysical inverse problems, this is the case for mixed-determined or under-determined. The classification depends on the number of available data and its coverage as well as the spatial discretization that is chosen to construct the model. To invert the matrix $\mathbf{J}^T \mathbf{J}$, a regularization is introduced. Most commonly, the Tikhonov regularization method is applied which is defined through the following parametric functional ϕ:

$$\phi = \phi_{\mathrm{d}} + \lambda \phi_{\mathrm{m}} = \phi_{\mathrm{d}} + \lambda (\mathbf{m} - \mathbf{m}_{\mathrm{ref}})^T \mathbf{W}_{\mathrm{m}}{}^T \mathbf{W}_{\mathrm{m}} (\mathbf{m} - \mathbf{m}_{\mathrm{ref}}) = \min. \tag{2.20}$$

The parametric functional ϕ has a term describing the data misfit (ϕ_{d}) and a model misfit term (ϕ_{m}). As seen, ϕ_{m} can be described through the model parameters $\mathbf{m}$ and some reference model $\mathbf{m}_{\mathrm{ref}}$ if one is chosen for the inversion as well as the regularization matrix $\mathbf{W}_{\mathrm{m}}$, also known as the model weighting matrix. The choice of the regularization matrix is of importance as it determines the kind of regularization and therefore influences the solution drastically (Zhdanov, 2015).

If $\mathbf{W}_{\mathrm{m}}$ is the identity matrix, it will produce a damped LSQR-solution, also known as the minimum length solution. Looking at eq. 2.20 it can be seen that in this case, the minimum of the model misfit term would be reached when the model equals the reference model. Therefore, this approach can be understood as a damping towards the reference model in regions of the model space where little to no information is available. This approach is most successful if the reference model is sufficiently close to the true model. In many cases $\mathbf{W}_{\mathrm{m}}$ is chosen to be a first or second order finite-difference operator, which approximates the first or second derivative of the model parameter distribution. The corresponding model weighting matrices for a 1-D model are shown in eq. 2.21.

$$\mathbf{W}_1 = \frac{1}{\Delta x} \begin{bmatrix} -1 & 1 & 0 & & & \\ 0 & -1 & 1 & 0 & & \\ & & & \ddots & & \\ & & & 0 & -1 & 1 \end{bmatrix}, \quad \mathbf{W}_2 = \frac{1}{\Delta x^2} \begin{bmatrix} 1 & -2 & 1 & 0 & & \\ 0 & 1 & -2 & 1 & 0 & \\ & & & \ddots & & \\ & & 0 & 1 & -2 & 1 \end{bmatrix}. \tag{2.21}$$

The resulting solution has a rather smooth distribution of model parameters as strong variations between neighbouring model parameters are penalized. Therefore, it can be interpreted as a measure of the smoothness or flatness of the model and the resulting model appears to have less outliers and resembles a clearer image. Note, that the rows of the smoothness operator matrix are referring to the internal cell boundaries of the model domain while the columns reflect the number of model parameters (Menke, 2018).

If the regularization parameter λ was chosen too large during an inversion, ϕ_m would be contributing too strong to the parametric functional with respect to the data misfit functional. This might result in a solution that is very close to some reference model in case of damping or a very smooth solution in case of smoothing. However, the data misfit might not be sufficiently small such that the solution does not explain the data within the uncertainty. Therefore, different regularization parameters should be tested during inversions to obtain the optimal solution (Menke, 2018). It is important to mention that often the choice of regularization is very subjective and therefore dependent on preferences and experiences of the person performing the inversion. Keeping that in mind is important as the regularization introduces constraints that have a major influence on the solution. Also note that the data misfit term in eq. 2.20 can be described with (eq. 2.17) or without data weighting (eq. 2.6).

To find the non-linear LSQR-solution of the problem that is described by the parametric functional (eq. 2.20), the first derivative is set to zero. Combining eq. 2.20 with eq. 2.10 and 2.11 results in the following expression of the regularized Gauss-Newton model update:

$$\Delta \mathbf{m}_n = \left(\mathbf{J}^T\mathbf{J} + \lambda \mathbf{W}_\mathrm{m}^T \mathbf{W}_\mathrm{m}\right)^{-1} \left(\mathbf{J}^T\left(\mathscr{F}(\mathbf{m}_n) - \mathbf{d}\right)\right) - \lambda \mathbf{W}_\mathrm{m}^T \mathbf{W}_\mathrm{m}\left(\mathbf{m}_n - \mathbf{m}_\mathrm{ref}\right). \tag{2.22}$$

Finally, incorporating measurement errors results in the model update of the weighted regularized Gauss-Newton solution (Loke and Dahlin, 2002; Menke, 2018; Zhdanov, 2015):

$$\Delta \mathbf{m}_n = \left(\mathbf{J}^T\mathbf{W}_\mathrm{d}^T\mathbf{W}_\mathrm{d}\mathbf{J} + \lambda \mathbf{W}_\mathrm{m}^T \mathbf{W}_\mathrm{m}\right)^{-1} \left(\mathbf{J}^T\mathbf{W}_\mathrm{d}^T\mathbf{W}_\mathrm{d}\left(\mathscr{F}(\mathbf{m}_n) - \mathbf{d}\right) - \lambda \mathbf{W}_\mathrm{m}^T \mathbf{W}_\mathrm{m}\left(\mathbf{m}_n - \mathbf{m}_\mathrm{ref}\right)\right). \tag{2.23}$$

This expression for the weighted, regularized inversion is implemented in the inversion framework pyGIMLi (Rücker et al., 2017) and will be used for inversions within this work.

2.3 Joint inversion

2.3.1 Overview of joint inversion approaches

As mentioned in the previous section, geophysical problems are usually mixed-determined or under-determined, depending on the data and the spatial discretization. Therefore, there is not one unique solution but several models that explain the observations within the uncertainties. The resulting models are ambiguous, which could lead to difficulties for later interpretation. However, if data of several geophysical methods was acquired it will be possible to invert the independent measurements in a combined manner to reduce this ambiguity. This process is generally referred to as joint inversion (Moorkamp et al., 2011; Wagner and Uhlemann, 2021). Different approaches of joint inversion are presented in Figure 2.4 and will be discussed in the following paragraphs. Note that the independent inversion of different geophysical data (Figure 2.4A) and a joint interpretation of the resulting models is not considered a joint inversion as there is no coupling between the inversion instances.

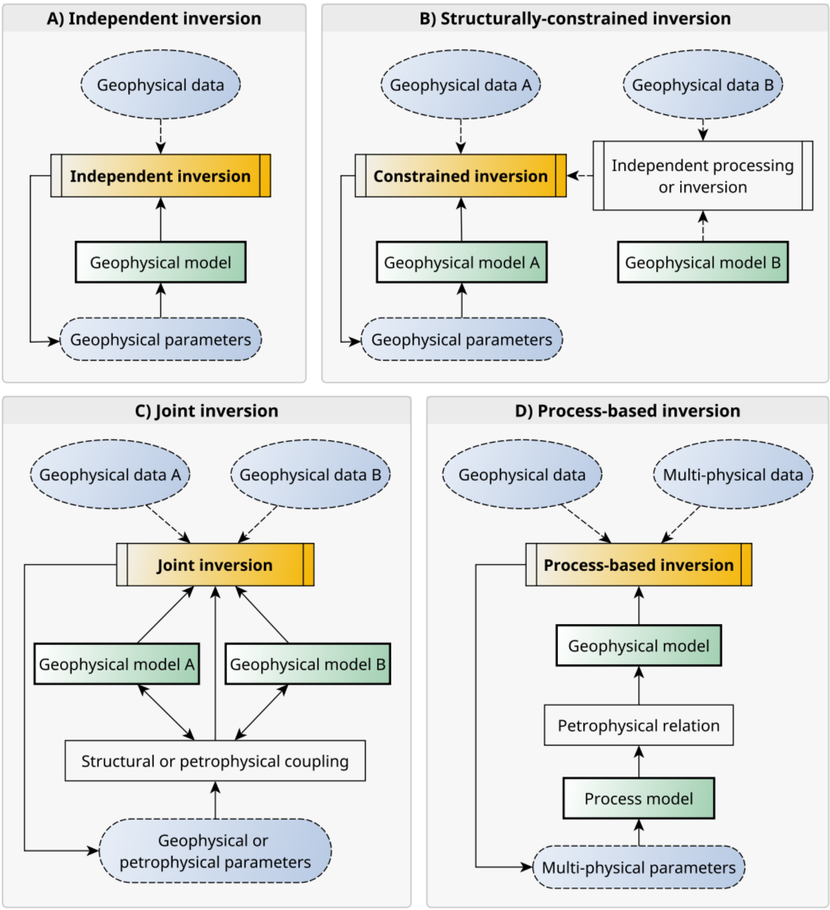

Figure 2.4: Schematic overview of A) independent geophysical inversion and various multi-method imaging approaches including B) structurally-constrained, C) joint, and D) process-based inversion (Wagner and Uhlemann, 2021).

2.3.1.1 Structurally-constrained inversion

In many applications, the goal is to image dominant boundaries in the subsurface geology, for example the boundaries confining an aquifer. Some geophysical methods like the seismic reflection method or ground penetrating radar (GPR) are suitable to locate these boundaries quite well as they exploit the reflection properties of subsurface features, while other methods like SRT or ERT generally return smooth images due to the smoothness operator in the regularized inversion process. It is possible to use the location of the boundaries obtained from one method, e.g. seismic reflection, as a-priori information for the inversion of another method, e.g. ERT (Bergmann et al., 2014). This is done by identifying cell boundaries in the inversion mesh that coincide with the subsurface feature and decouple the model parameters belonging to the respective cells around the boundary. By manipulating the smoothness matrix in the Tikhonov regularization (eq. 2.21) accordingly, the regularization constraint is weakened or even fully removed along the subsurface boundary allowing strong variations between model parameters that are located along it. That can be achieved by multiplying the corresponding rows of the model weighting matrix $\mathbf{W}_\mathrm{m}$ with some weighting factor that can take values between zero and one (Bergmann et al., 2014; Menke, 2018; Wagner and Uhlemann, 2021). This approach is referred to as structurally-constrained inversion and it is summarized in Figure 2.4B. It is important to mention that the structural decoupling has a strong influence on the structure and the amplitude of the resulting subsurface image and therefore the result is strongly influenced by the uncertainties of the decoupling constraint. Bergmann et al. (2014) and Wagner and Uhlemann (2021) propose to use this approach solely for evidence-based structural constraints like drill cores or logging information.

2.3.1.2 Structurally-coupled joint inversion

The motivation behind structurally-coupled joint inversion (Figure 2.4C) is similar to the structurally-constrained inversion (Figure 2.4B). Different methods should sense the same subsurface structures and the resulting images should therefore have structural similarity. However, in many cases it is not recommended to use a structurally-constrained approach, especially if there is no hard evidence of subsurface structures by drillings or excavations. A more flexible way of enforcing structural similarity is presented by structural coupling approaches. There are several structural coupling methods that are all based on the minimization of some similarity measure that is incorporated in the overall misfit functional of the inversion. Haber and Oldenburg (1997) present a first structural joint inversion approach that enforces spatial similarities without prescribing exact locations of these. The method is based on the minimization of the quadratic difference of the Laplacian operator of the models during the inversion. One of the most common structural coupling approaches is based on the cross-product of the individual model gradients (Gallardo and Meju, 2004; Gallardo et al., 2005). The parametric functional of the joint inversion instance holds the cross-gradient functional τ as an additional regularization term. The cross-gradient functional τ of two methods A and B is defined as follows:

$$\tau(x, y, z) = \nabla \mathbf{m}_\mathrm{A} \times \nabla \mathbf{m}_\mathrm{A}. \tag{2.24}$$

It can be seen in eq. 2.24 that τ is minimized if one of the gradients is zero or if the the gradients are parallel or anti-parallel. The latter indicate that the structure of the image must be similar. This approach was demonstrated for numerous applications and methods (Moorkamp et al., 2016) and is also applicable for joint inversions involving more than two methods (Gallardo, 2007). However, the translation of this gradient-based approach to unstructured meshes is not trivial as shown by Jordi et al. (2020).

There is a sub-category of structurally coupled joint inversion approaches that are not based on a shared joint objective functional but individual inversion instances that exchange structural information throughout the inversion process. This method is referred to as structurally-coupled cooperative joint inversion (SCCI). Günther and Rücker (2006) introduce an approach that uses the roughness, or smoothness, of the individual models at each internal boundary of the model domain. Using the roughness vectors of each method a weighting factor $\mathbf{w}$ for the boundaries is used to enable the exchange of structural information and the focusing on common boundaries. It is important to mention that this approach requires identical model discretization which might be challenging for methods with strongly differing resolutions (Günther and Rücker, 2006; Wagner and Uhlemann, 2021; Skibbe et al., 2021).

Even though the mentioned structural coupling approaches have a wide use in the field of geophysical imaging, they are limited to methods that sense the same structures in the subsurface. To illustrate this, consider a water salinity or water saturation gradient that is affecting the subsurface electrical resistivities but not necessarily the seismic velocities. In such a scenario it is not very useful to enforce structural similarity during the inversion process as the seismic data resembles the geologic structure while the resistivity data is strongly influenced by the fluids. Note that the before mentioned approaches are just a small selection of coupling methods. There are several other methods and variations that handle structural coupling in geophysical inversion (Moorkamp et al., 2016; Tu and Zhdanov, 2021; Zhdanov et al., 2022).

2.3.1.3 Additional joint inversion approaches

Instead of exploiting structural similarities during a joint inversion, it is also possible to use petrophysical relationships to transform geophysical properties like electrical resistivities into petrophysical properties like water saturation or porosity. Including petrophysical relationships during the inversion does not only allow jointly inverting different data sets but also ensures the plausibility of the resulting petrophysical parameters. It can also lead to an increased robustness for monitoring applications if the considered petrophysical parameter is constant throughout the time of investigation. This approach is referred to as petrophysical joint inversion and is widely used in the near surface community where petrophysical relationships for water saturation or permafrost parameters are sufficiently known. However, petrophysical models might not exist for some methods or require extensive calibrations based on samples in the laboratory which makes this approach not feasible. There are also process-based inversion approaches (Figure 2.4D) that are mainly used for studies of dynamic processes in the subsurface. They allow the inclusion of non-geophysical observations like soil moisture content which results in improved imaging of non-geophysical parameters. However, similar to the petrophysical inversion they require petrophysical and process models to create the link between geophysical and non-geophysical data (Wagner and Uhlemann, 2021).

2.3.2 Structurally coupled joint inversion with joint entropy stabilizers

As described in subsubsection 2.3.1.2, structurally coupled joint inversion approaches are useful to jointly invert geophysical data sets as they flexibly promote structural similarity in the resulting models. Zhdanov et al. (2022) introduce a novel approach that uses joint minimum entropy constraints to promote structural similarity between methods.

2.3.2.1 Entropy

In the field of information theory, the term entropy can be understood as the level of uncertainty of a system of random variables (Shannon, 1948). Consider a probability density function $p_{\mathrm{f}}(t)$ of a random variable $f(t)$. Here, t represents an element of a finite alphabet $\mathscr{T}$ such that the resulting entropy of the system is defined as (Caticha, 2007; Gray, 2013; Shannon, 1948):

$$H_{p(f)} = -\sum_{t \in \mathscr{T}} p_{\mathrm{f}}(t) \ln p_{\mathrm{f}}(t). \tag{2.25}$$

Since $p_f(t)$ represents a probability density function the following relations have to hold:

$$\begin{aligned} &0 \leq p_f(t) \leq 1 \ \text{ for } \ t \in \mathscr{T} \\ &\sum_{t \in \mathscr{T}} p_f(t) = 1 \end{aligned} \tag{2.26}$$

As this formulation of entropy is originating from the field of information science, this definition of entropy is still quite abstract and hard to relate to the geophysical domain. However, the connection can be made when considering a probabilistic formulation of the geophysical inverse problem (Zhdanov, 2002). Consider a geophysical model with model parameter vector $\mathbf{m}(\mathbf{r})$ which is described as a random variable at any point $\mathbf{r}$ in the spatial discretization of the model domain Ω. Analogue to eq. 2.26, a probability density function $p_m(\mathbf{r})$ can then be formulated as:

$$p_m(\mathbf{r}) = \frac{|\mathbf{m}(\mathbf{r})|}{Q} \ \text{ with } \ Q = \int_\Omega |\mathbf{m}(\mathbf{r})| \ d\mathbf{r}. \tag{2.27}$$

Note that the integral over the spatial model domain Ω can describe a 1D, 2D or 3D space. It can be seen that the pseudo probability density function $p_m(\mathbf{r})$ satisfies the conditions of eq. 2.26 as the division by normalization factor Q ensures the second condition while the absolute value ensures the first condition. Since these criteria are met, the entropy on the model space can be expressed as:

$$H(\mathbf{m}) = -\int_\Omega p_m(\mathbf{r}) \ \ln p_m(\mathbf{r}) \ d\mathbf{r}. \tag{2.28}$$

To further illustrate the entropy of the model space, consider the quadratic model domain with a homogeneous background and a strong anomaly in the center. Figure 2.5 shows the initial model on the left which is increasingly smoothed using a Gaussian filter. Using eq. 2.27 and eq. 2.28 the entropy is calculated and it can be seen that the entropy H of that model is inversely related to the sharpness of the model. Therefore, the entropy reaches smaller values for smaller and stronger anomalies it can also be understood as a measure of sparsity which is a more intuitive link to information sciences.

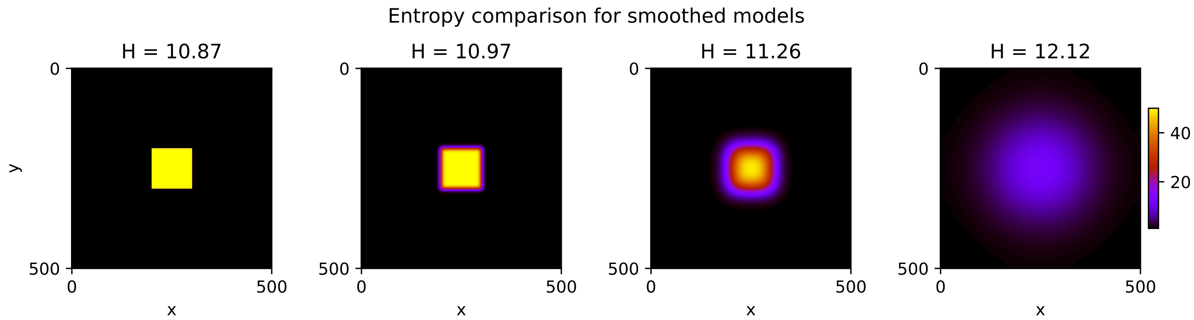

Figure 2.5: Comparison of entropy values H for increasingly smoothed models. The figure shows the initial model (left) and smoothed versions of the initial model right of it. The entropy H is calculated based on eq. 2.27 and eq. 2.28.

The relation in eq. 2.27 can be generalized as any transformation of the model $T[\mathbf{m}(\mathbf{r})]$ can be used as an equivalent of the probability density function.

$$p_{\mathrm{T}}(\mathbf{r}) = \frac{|T[\mathbf{m}(\mathbf{r})]|}{Q_{\mathrm{T}}} \quad \text{with } Q_{\mathrm{T}} = \int_{\Omega} |T[\mathbf{m}(\mathbf{r})]| \, d\mathbf{r}. \tag{2.29}$$

Possible transformations could be differential operators like the gradient (∇) or the Laplacian (Δ) as well as different powers of the model. Note that different transformations enforce different entropy conditions and therefore influence the final outcome accordingly. Based on the generalized entropy formulation in eq. 2.29, the expressions for minimum entropy and joint minimum entropy can be derived.

2.3.2.2 Minimum entropy stabilizers

To implement the concept of entropy in the geophysical inversion, the parametric functional ϕ has to be manipulated as follows (Zhdanov, 2002):

$$\phi(\mathbf{m}) = \phi_{\mathrm{d}} + \lambda S. \tag{2.30}$$

Here, a different regularization term, namely S, is introduced in the parametric functional. Using eqs. 2.29 and 2.28, Zhdanov (2002) and Zhdanov et al. (2022) derive the expressions for the minimum entropy (ME) stabilizer S_{ME} and minimum entropy gradient (MEG) stabilizer S_{MEG} as shown below:

$$S_{\mathrm{qME}} = -\int_{\Omega} \frac{|\mathbf{m}(\mathbf{r}) - \mathbf{m}_{\mathrm{ref}}(\mathbf{r})|^{q} + \beta}{Q_{\mathrm{qME}}} \ln \frac{|\mathbf{m}(\mathbf{r}) - \mathbf{m}_{\mathrm{ref}}(\mathbf{r})|^{q} + \beta}{Q_{\mathrm{qME}}} \, \mathrm{d}\mathbf{r}, \tag{2.31}$$

$$\text{where } Q_{\mathrm{qME}} = \int_{\Omega} |\mathbf{m}(\mathbf{r}) - \mathbf{m}_{\mathrm{ref}}(\mathbf{r})|^{q} + \beta \, \mathrm{d}\mathbf{r}. \tag{2.32}$$

$$S_{\mathrm{qMEG}} = -\int_{\Omega} \frac{||\nabla \mathbf{m}(\mathbf{r})||^{q} + \beta}{Q_{\mathrm{qMEG}}} \ln \frac{||\nabla \mathbf{m}(\mathbf{r})||^{q} + \beta}{Q_{\mathrm{qMEG}}} \, \mathrm{d}\mathbf{r}, \tag{2.33}$$

$$\text{where } Q_{\mathrm{qMEG}} = \int_{\Omega} ||\nabla \mathbf{m}(\mathbf{r})||^{q} + \beta \, \mathrm{d}\mathbf{r}. \tag{2.34}$$

Here, q represents the order of the entropy expression, β is some small value to ensure numerical stability by removing the singularity and $||\cdot||$ indicates the L2-norm. It is beneficial to include a reference model $\mathbf{m}_{\mathrm{ref}}$ in the minimum entropy stabilizer S_{qME} to avoid that the stabilizer promotes model parameters to become zero or very close to zero. This would lead to errors for many geophysical methods as some material properties like seismic velocity and electrical resistivity are not defined for 0 m/s and 0 Ωm respectively.

As the entropy stabilizer is minimized during the inversion, this justifies the name of the approach (minimum entropy constraints). Note that different expressions of entropy stabilizers are also possible following eq. 2.29. Considering an inversion instance using the minimum entropy stabilizer S_{qME}, the regularization will promote models with a lower entropy and therefore a simpler and sparser solution which is beneficial for many applications (Zhdanov et al., 2022). This is also in accordance with the principle of Occam's razor, which states that the simplest solution to explain an observation is always preferred (Constable et al., 1987).

2.3.2.3 Joint Minimum entropy stabilizers

The idea of the minimum entropy stabilizer within the geophysical inversion is just one of many possible regularization methods (Zhdanov, 2015; Moorkamp et al., 2016) and not as commonly used as, for example, the Tikhonov regularization. However, its value lies within the simple extension from a single-method stabilizer into a multi-method scheme. Consider a geophysical multi-method problem with model parameters $\mathbf{m}^{(i)}$ that refer to the used methods. The joint parametric functional ϕ_J can then be described as

$$\phi_{\mathrm{J}}\left(\mathbf{m}^{(1)}, \mathbf{m}^{(2)}, \ldots, \mathbf{m}^{(M)}\right) = \sum_{i=1}^{M} \phi_{\mathrm{d}}^{(i)} + \lambda S_{\mathrm{J}}\left(\mathbf{m}^{(1)}, \mathbf{m}^{(2)}, \ldots, \mathbf{m}^{(M)}\right). \tag{2.35}$$

Here M represents the number of methods, $\phi_{\mathrm{d}}^{(i)}$ is the data misfit term of the respective method and S_{J} represents some joint stabilizer that depends on all given models. Zhdanov et al. (2022) introduce the extension of eq. 2.31 to a joint minimum entropy (JME) stabilizer S_{qJME} of order q with following expressions:

$$S_{\mathrm{qJME}} = -\int_{\Omega} \frac{\left(\sum_{i=1}^{M} \left|\mathbf{m}^{(i)}(\mathbf{r}) - \mathbf{m}_{\mathrm{ref}}^{(i)}(\mathbf{r})\right|^{q} + \beta\right)}{Q_{\mathrm{qJME}}} \ln \frac{\left(\sum_{i=1}^{M} \left|\mathbf{m}^{(i)}(\mathbf{r}) - \mathbf{m}_{\mathrm{ref}}^{(i)}(\mathbf{r})\right|^{q} + \beta\right)}{Q_{\mathrm{qJME}}} \, d\mathbf{r}, \tag{2.36}$$

$$\text{where } \; Q_{\mathrm{qJME}} = \int_{\Omega} \left(\sum_{i=1}^{M} \left|\mathbf{m}^{(i)}(\mathbf{r}) - \mathbf{m}_{\mathrm{ref}}^{(i)}(\mathbf{r})\right|^{q} + \beta\right) d\mathbf{r}. \tag{2.37}$$

The resulting stabilizer S_{qJME} will promote consistent images of the same subsurface structure as the joint disorder of both methods will be reduced. This is further illustrated in Figure 2.6. It can be seen that the joint entropy is smallest for perfectly overlapping anomalies and increasingly higher for larger shifts between the model anomalies. Therefore, the joint entropy holds information about the structural similarity between models. Similarly, the expression for the minimum entropy gradient stabilizer S_{qMEG} can be extended to the concept of joint minimum entropy gradient (JMEG) stabilizer. Using this joint minimum entropy gradient stabilizer S_{qJMEG} will promote fewer and sharper gradients in similar regions of the different models and therefore produce similar structures (Zhdanov et al., 2022). The stabilizer is defined as:

$$S_{\mathrm{qJMEG}} = -\int_{\Omega} \frac{\left(\sum_{i=1}^{M} \left\|\nabla \mathbf{m}^{(i)}(\mathbf{r})\right\|^{q} + \beta\right)}{Q_{\mathrm{qJMEG}}} \ln \frac{\left(\sum_{i=1}^{M} \left\|\nabla \mathbf{m}^{(i)}(\mathbf{r})\right\|^{q} + \beta\right)}{Q_{\mathrm{qJMEG}}} \, d\mathbf{r}, \tag{2.38}$$

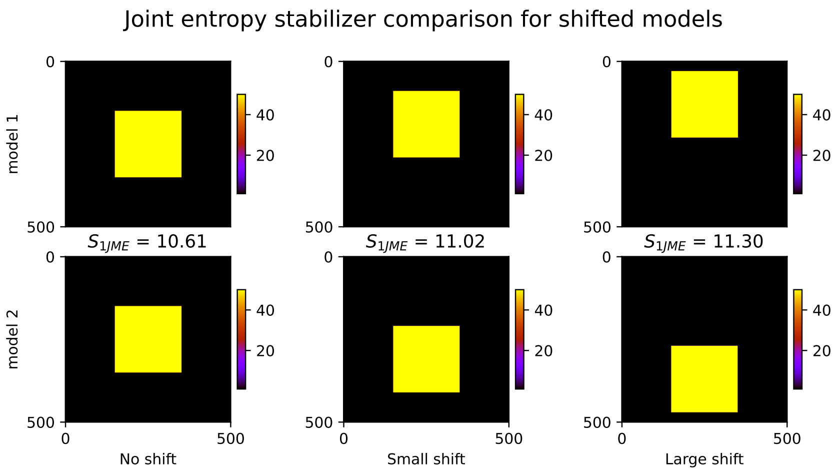

Figure 2.6: Comparison of Joint Entropy $S_{1\mathrm{JME}}$ for equal background models with shifted anomalies. S_{qJME} was calculated using eq. 2.36 where $\beta = 10^{-12}$, $q = 1$ and $\mathbf{m}_{\mathrm{ref}} = \mathbf{m}_{\mathrm{background}}$. Note that the joint entropy is smaller for smaller shifts. Small values therefore indicates similarities between different models.

$$\text{where } Q_{\mathrm{qJMEG}} = \int_{\Omega} \left(\sum_{i=1}^{M} \left\| \nabla \mathbf{m}^{(i)}(\mathbf{r}) \right\|^{q} + \beta \right) \mathrm{d}\mathbf{r}. \tag{2.39}$$

Note, that eqs. 2.36 and 2.38 equal their respective single method expressions in eqs. 2.31 and 2.33 for $M = 1$.

2.3.2.4 Representation of joint entropy stabilizers

To use the common non-linear inversion schemes like the Gauss-Newton scheme (2.2), a quadratic regularization term is necessary. Since the joint entropy stabilizers in eqs. 2.36 and 2.38 are non-quadratic, it is challenging to implement them into the corresponding parametric functional ϕ (eq. 2.30) or ϕ_J (eq. 2.35). To overcome this issue, Zhdanov (2002, 2015) propose, to transfer the expressions of the entropy stabilizers into a pseudo-quadratic form that can be written in the form of ϕ_{m} in eq. 2.20. Therefore, we express the entropy stabilizer S as:

$$S = \left(\mathbf{m}(\mathbf{r}) - \mathbf{m}_{\mathrm{ref}}(\mathbf{r})\right)^{T} \mathrm{W_e}^{T}\, \mathrm{W_e} \left(\mathbf{m}(\mathbf{r}) - \mathbf{m}_{\mathrm{ref}}(\mathbf{r})\right) = \int_{\Omega} \left| w_{\mathrm{e}}(\mathbf{r}) \left(\mathbf{m}(\mathbf{r}) - \mathbf{m}_{\mathrm{ref}}(\mathbf{r})\right)\right|^{2} \mathrm{d}\mathbf{r}. \tag{2.40}$$

Here, $\mathbf{W}_{\mathrm{e}}$ represents a diagonal model weighting matrix diag(ω_{e}) that contains specific model weights $\omega_{\mathrm{e}}(\mathbf{r})$ that depend on the current model and the reference model. Note that in case of a regular spatial discretization $w_{\mathrm{e}} = \omega_{\mathrm{e}}$ holds. For unstructured models the discretization has to be taken into account to ensure a mathematical correct approximation of the integral. The effects of this will be discussed in Chapter 3 (Method). The pseudo-quadratic form for the joint entropy stabilizers is constructed similar as seen in eq. 2.41.

$$S_J = \sum_{i=1}^{M} \left(\mathbf{m}^{(i)}(\mathbf{r}) - \mathbf{m}_{\mathrm{ref}}^{(i)}(\mathbf{r})\right)^{T} \mathbf{W}_{\mathrm{e}}^{(i)T}\, \mathbf{W}_{\mathrm{e}}^{(i)} \left(\mathbf{m}^{(i)}(\mathbf{r}) - \mathbf{m}_{\mathrm{ref}}^{(i)}(\mathbf{r})\right) \tag{2.41}$$

Considering a regular spatial discretization scheme, it can be shown that the following expressions for the specific model weights ω_e, that are included in the model weighting matrices $\mathbf{W}_e$, lead to equality between eqs. 2.31, 2.33, 2.36 and 2.38 and their respective pseudo-quadratic forms (Zhdanov et al., 2022):

$$\omega_{\mathrm{qME}}(\mathbf{r}) = \left[\frac{|\mathbf{m}(\mathbf{r}) - \mathbf{m}_{\mathrm{ref}}(\mathbf{r})|^q + \beta}{Q_{\mathrm{qME}}\left(|\mathbf{m}(\mathbf{r}) - \mathbf{m}_{\mathrm{ref}}(\mathbf{r})|^2 + \beta\right)} \ln \frac{Q_{\mathrm{qME}}}{|\mathbf{m}(\mathbf{r}) - \mathbf{m}_{\mathrm{ref}}(\mathbf{r})|^q + \beta} \right]^{\frac{1}{2}}, \tag{2.42}$$

$$\omega_{\mathrm{qMEG}}(\mathbf{r}) = \left[\frac{\|\nabla \mathbf{m}(\mathbf{r})\|^q + \beta}{Q_{\mathrm{qMEG}}\left(|\mathbf{m}(\mathbf{r}) - \mathbf{m}_{\mathrm{ref}}(\mathbf{r})|^2 + \beta\right)} \ln \frac{Q_{\mathrm{qMEG}}}{\|\nabla \mathbf{m}(\mathbf{r})\|^q + \beta} \right]^{\frac{1}{2}}, \tag{2.43}$$

$$\omega_{\mathrm{qJME}}{}^{(i)}(\mathbf{r}) = \left[\frac{\left|\mathbf{m}^{(i)}(\mathbf{r}) - \mathbf{m}^{(i)}_{\mathrm{ref}}(\mathbf{r})\right|^q + \beta}{Q_{\mathrm{qJME}}\left(\left|\mathbf{m}^{(i)}(\mathbf{r}) - \mathbf{m}^{(i)}_{\mathrm{ref}}(\mathbf{r})\right|^2 + \beta\right)} \ln \frac{Q_{\mathrm{qJME}}}{\sum_{j=1}^{M}\left|\mathbf{m}^{(j)}(\mathbf{r}) - \mathbf{m}^{(j)}_{\mathrm{ref}}(\mathbf{r})\right|^q + \beta} \right]^{\frac{1}{2}}, \tag{2.44}$$

$$\omega_{\mathrm{qJMEG}}{}^{(i)}(\mathbf{r}) = \left[\frac{\left\|\nabla \mathbf{m}^{(i)}(\mathbf{r})\right\|^q + \beta}{Q_{\mathrm{qJMEG}}\left(|\mathbf{m}(\mathbf{r}) - \mathbf{m}_{\mathrm{ref}}(\mathbf{r})|^2 + \beta\right)} \ln \frac{Q_{\mathrm{qJMEG}}}{\sum_{j=1}^{M}\left\|\nabla \mathbf{m}^{(j)}(\mathbf{r})\right\|^q + \beta} \right]^{\frac{1}{2}}. \tag{2.45}$$

Since the stabilizer is now in the same form as the common Tikhonov regularization (eq. 2.20), they can be used in the general framework of the regularized and weighted Gauss-Newton algorithm (section 2.2). However, it is important to mention that the entropy-constrained weights in the inversion are all depending on the models of the previous iteration. Therefore, the diagonal model weighting matrix needs to be recalculated each iteration. The inversion algorithm will then minimize the joint parametric functional with entropy stabilizers ϕ_{JE} as defined below:

$$\phi_{\mathrm{JE}}\left(\mathbf{m}^{(1)}, \mathbf{m}^{(2)}, \ldots, \mathbf{m}^{(M)}\right) = \sum_{i=1}^{M} \phi_{\mathrm{d}}^{(i)} + \sum_{i=1}^{M} \lambda^{(i)} \left(\mathbf{m}^{(i)}(\mathbf{r}) - \mathbf{m}^{(i)}_{\mathrm{ref}}(\mathbf{r})\right)^T \mathbf{W}_{\mathrm{e}}^{(i)T}\, \mathbf{W}_{\mathrm{e}}^{(i)} \left(\mathbf{m}^{(i)}(\mathbf{r}) - \mathbf{m}^{(i)}_{\mathrm{ref}}(\mathbf{r})\right). \tag{2.46}$$

Here, $\mathbf{W}_{\mathrm{e}}^{(i)}$ refers to either the joint minimum entropy or joint minimum entropy gradient weighting matrix which is a diagonal damping matrix. The regularization method can therefore be interpreted as model-specific damping. The different methods are purely coupled through the calculation of the weights at each iteration and therefore allows for separate inversion instances that are stopped after each iteration to recalculate the weights. This exchange of structural information throughout the inversion process justifies that Zhdanov et al. (2022) label this approach as a structurally-coupled cooperative inversion rather than a structurally-coupled joint inversion. The implementation of this method will be used and discussed in the following chapters.

3

Method

Contents

This chapter presents the implementation of the entropy constrained SCCI approach within the open-source library pyGIMLi (Section 3.1). The governing parameters as well as underlying choices that are made in this implementation are introduced and presented. Section 3.2 will illustrate the concept of the approach with simple 2D examples with the objective to create a better understanding and intuition of the method.

3.1 Implementation of joint minimum entropy constraints

The implementation of the joint inversion approach with joint minimum entropy constraints (eqs. 2.44 and 2.45) is done within the open-source library pyGIMLi (Rücker et al., 2017). In the frame of this work a joint inversion class is created that uses the theory of joint entropy constraints to jointly invert any given number of geophysical methods. The class-object and its workflow is further illustrated in Figure 3.1. The core of the approach is the structurally-coupled cooperative inversion scheme which involves a recalculation of the model weights after each iteration using the corresponding formulas presented in Chapter 2 (Theory). The flowchart already indicates the simplicity of the approach as existing inversion frameworks can be adjusted to successfully implement the method. In the following sections more detailed descriptions of certain aspects of the class as well as the important parameters are provided.

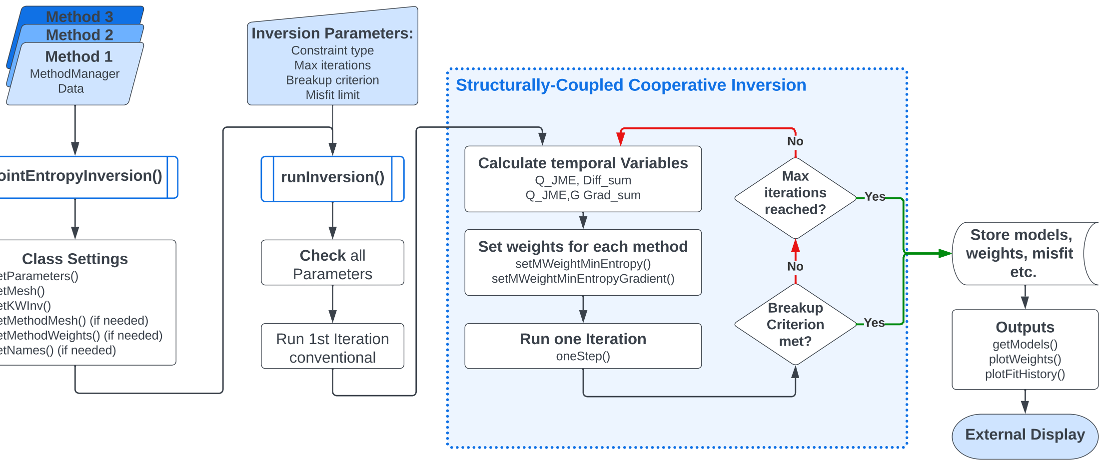

Figure 3.1: Flowchart illustrating the workflow of joint inversion using the JointEntropyInversion class.

3.1.1 Pre-Inversion phase

This implementation requires a *pygimli.frameworks.MethodManager* object as well as the corresponding data for each geophysical method that should be included in the joint inversion. Another input is an inversion mesh that is suitable for the data inversion of every given method. It is important to note that this mesh will be used as the parameter domain and therefore each cell of this mesh can be referred to as a model parameter during the inversion. To ensure the applicability of this method for the ERT method, an option was implemented that allows to use another mesh for the inversion which has an extended model region to prevent numerical artefacts introduced by the boundary conditions. However, the parameter domain of the inversion mesh of each method has to be identical to ensure that the joint entropy constraints can be applied.

Furthermore, the parameters q and β (eqs. 2.44 and 2.45) are set along with the smoothing variable a, method-specific weighting factors and keyword dictionaries that hold information about the method specific inversion parameters. The latter includes the regularization parameter λ that was introduced in Chapter 2 (Theory) as well as the start model of the inversion. The effects of these parameters are investigated in Chapter 4 (Synthetic study). It is important to mention that the starting model is also defined as the reference model for the inversion and therefore it should be chosen carefully as it influences the outcome drastically due to the damping during the inversion.

3.1.2 Normalization of different geophysical parameters

A common problem in every scientific field of research that combines different data sets is the normalization of the data to ensure comparability. To illustrate this issue in the context of geophysics and the joint minimum entropy constraints, consider a seismic velocity model and an electrical resistivity model. While natural seismic velocities vary between several hundreds to several thousands of m/s, resistivities might vary over more than five magnitudes of Ωm. Since eq. 2.44 considers differences of model parameters, changes in the resistivity are weighted stronger than velocity changes simply due to their dimensionality. To minimize these effects, the properties should be transferred to a similar range which makes them comparable. This can be achieved by normalization of the model parameters. Zhdanov et al. (2022) normalize the model parameters by the maximum model contrast and weigh them with the integrated sensitivities of the standalone inversion result. However, to not be dependent on previous single-method inversion runs the following normalization was chosen:

$$\mathbf{m}_n^{i\,\mathrm{norm}} = \frac{\ln \mathbf{m}_n^i - \min\left(\ln \mathbf{m}^i\right)}{\max\left(\ln \mathbf{m}^i\right) - \min\left(\ln \mathbf{m}^i\right) + \beta} \tag{3.1}$$

This normalization is performed before every entropy weight calculation to ensure a similar range of model parameters $\mathbf{m}^i$ of all methods. Eq. 3.1 uses the logarithmic transform of the models and normalizes them to values between 0 and 1. To ensure numerical stability for the case of a homogeneous model, the numerical stabilizer β is present in the denominator. It is important to mention that for the calculation of the stabilizers the reference model has to be transformed and normalized as well using the minimum and maximum values of the logarithmic model $\mathbf{m}^i$. The exact implementation can be seen in Listing 3.1

```python
def normalize(self, m, m0):
    mmin = min(np.log(m)) # Minimum of log(model)
    mmax = max(np.log(m)) # Maximum of log(model)

    # Normalizing current and starting model
    m_new = (np.log(m)-mmin)/(mmax-mmin+self.b)
    m0_new = (np.log(m0)-mmin)/(mmax-mmin+self.b)
    return m_new, m0_new
```

Listing 3.1: Function to normalize the model parameters and the reference model

3.1.3 Influence of cell sizes

As already mentioned in subsection 2.3.2, the derived expressions for the resulting model weights of the JME (eq. 2.44) and JMEG (eq. 2.45) stabilizers are only valid if a regular discretization of the model domain was chosen. However, for many applications it is more feasible to use unstructured meshes to discretize a certain region of interest in the model domain finer resulting in varying cell sizes. For example, in the field of ERT modelling and inversion, it is common practice to use meshes with finer discretization close to the current injection points, while model cells at larger distance from electrode locations can be larger (Günther et al., 2006). This ensures numerical stability and improves flexibility of the meshing as well as decreases run time due to a smaller number of model parameters. Also, it allows to model complex topographies which is beneficial for many applications. Now consider an irregular mesh and a ME stabilizer, with eqs. 2.32 and 2.42 defining Q_{qME} and ω_{qME} respectively. In order to ensure a correct approximation of the integrals in eqs. 2.32 and 2.40, an additional factor compensating for the cell size needs to be included when transferring the continuous integrals into a discrete domain. Therefore, the following discretized expressions for Q'_{qME} and ω'_{qME} emerge:

$$Q'_{\mathrm{qME}} = \sum_{j=1}^{\Omega} \mathbf{c}_j \left(\left| \mathbf{m}_j - \mathbf{m}_{ref\ j} \right|^q + \beta \right), \tag{3.2}$$

$$\omega'_{\mathrm{qME}} = \left[\frac{\mathbf{c}\left(|\mathbf{m}-\mathbf{m}_{\mathrm{ref}}|^q + \beta\right)}{Q_{\mathrm{qME}}\left(|\mathbf{m}-\mathbf{m}_{\mathrm{ref}}|^2 + \beta\right)} \ln \frac{Q_{\mathrm{qME}}}{|\mathbf{m}-\mathbf{m}_{\mathrm{ref}}|^q + \beta} \right]^{\frac{1}{2}}. \tag{3.3}$$

Here, Ω denotes the number of model parameters $\mathbf{m}_j$ within the model vector $\mathbf{m}$ and $\mathbf{c}_j$ indicates a single cell size within the cell size vector $\mathbf{c}$. Note, that $\mathbf{m}$ and $\mathbf{m}_{\mathrm{ref}}$ are normalized model parameters as described in the previous section. The meaning behind above equations is quite intuitive as larger cells also have a higher contribution to the overall entropy of the model. However, this has a strong influence on the resulting model weights as illustrated in Figure 3.2. The figure shows three different model discretizations of a homogeneous model, namely a regular rectangular grid (Figure 3.2 left), a finer, more regular triangular mesh (Figure 3.2 middle) and a highly irregular mesh with finer meshing close to the surface (Figure 3.2 right). The first two rows show the meshes with the corresponding cell sizes which clearly differentiates the grid from the meshes. In the third row the model weights without cell size factor (eqs. 2.32, 2.42) are presented. Below that, the weights corresponding to eqs. 3.2 and 3.3 are shown. As mentioned before, the regular grid does not show any difference as every cell has an identical cell size and since we consider a homogeneous model with a homogeneous reference model, we find that all model parameters (i.e. model cells) are weighted equally. This intuitively makes sense as the entropy of a homogeneous model is considered flat.

When neglecting the cell sizes, both meshes also result in a homogeneous model weight distribution. Note that the different magnitude of the homogeneous model weights are differing due to different amounts of cells and therefore model parameters. However, if cell sizes are included the model weights resemble the structure of the cell sizes, resulting in smaller weights for smaller cells and vice versa. This ultimately leads to promoted changes in regions with smaller weights while larger cells are constantly damped towards the reference model. For the finer mesh these effects might only be minor as the cell sizes are comparably close to each other but for the very irregular mesh (Figure 3.2 right) these effects drastically influence the outcome. As minimum and maximum cell size of the mesh are differing by a factor of 100 and the cell size distribution has a clear structure, this structure is transferred to the model weights which will cause the algorithm to promote this structure during the inversion.

This suggests that the joint entropy approach should be performed on regular model discretizations. However, as mentioned earlier unstructured meshes have many benefits and therefore it is proposed to neglect the cell size factor during the weight calculation. This will avoid the introduction of meshing related structure during the inversion and allows the use of triangular, unstructured meshes. It is important to mention that this motivates the use of finer, more regular model discretizations if the computational environment allows for it. From an interpretative point of view, ignoring the cell sizes indicates that we enforce equal weighting of model parameters for the entropy calculation, meaning that each model parameter is contributing to the model entropy the same amount.

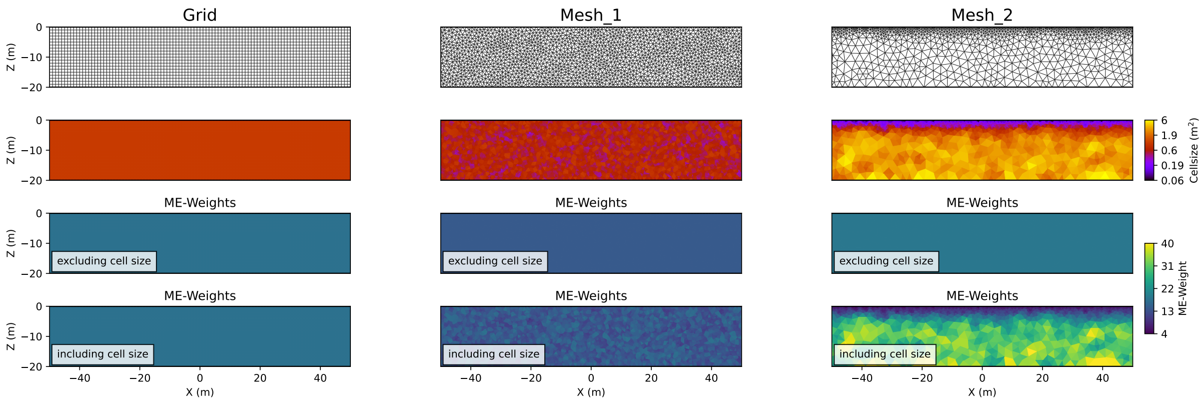

Figure 3.2: Illustration of cell size effects in the ME-weights. The columns are corresponding to a regular grid (left), a fine triangular mesh (middle) and a highly irregular mesh (right). The discretization with corresponding cell sizes are shown in the first two rows, while the weights of the homogeneous models are shown in the bottom rows. It can be seen that inclusion of cell sizes introduces meshing related structure into the weights which is not desirable.

3.1.4 Method weighting

The implementation of the joint minimum entropy approach was extended to allow for weighting between the methods which allows to lead the joint inversion more towards one of the used methods. To explain these weighting factors consider the extract of the code presented in Listing 3.2. Shown is the function that calculates and sets JME-weights. It can be seen that the method weighting factor (*method_weights*) is multiplied with the potentiated model contrast between current model and reference model. The factor is also multiplied with the contrast when computing the Q value and the denominator of the logarithm. As the logarithm is influenced by the sum of the model contrasts of each model at each cell, it is stronger influenced by the method with a higher weighting factor. This will increase the presence of the structure of the higher weighted model. However, it is important to mention that the method weighting factor also has a some influence on the magnitude of the resulting weights which can be compensated for through the regularization parameter λ. It is also not recommended to chose a very high method weighting for one method as this will restrict the flow of structural information during the joint inversion. The cooperative inversion scheme would then gradually turn into a constraint inversion which might enforce inversion artefacts of one method on the models of the others. The effect of method weighting is further illustrated in section 3.2.

```
1 def setMWeightMinEntropy(self, iteration, inv):
2     if iteration>0: # to ensure function applied after 0-th iteration
3         m0 = pg.Vector(inv.startModel)
4         m = inv.model
5         [m, m0] = self.normalize(m, m0)
6 
7         mesh = self.mesh
8         Q = self.Q_JME
9         # Index of manager in self.mgrs
10        mgr_i = np.argwhere([inv==mgr.inv for mgr in self.mgrs])[0][0]
11
12        # Calculate Weights
13        we = np.sqrt(1/Q * 1/(self.b+abs(m-m0)**2)*
14             (self.b+self.method_weights[mgr_i]*abs(m-m0)**self.q)*
15              np.log(Q/(self.b+self.Diff_sum)))
16
17        # re-set constrain weights corresponding to smoothness
18        Cweights = np.ones(len(inv.inv.cWeight()))*
19                   np.mean(we)*self.a[mgr_i]
20        # re-set constrain weights corresponding to damping
21        Cweights[-mesh.cellCount():] = we
22        # set weights in inversion instance
23        Cweights = pg.Vector(Cweights)
24        inv.inv.setCWeight(Cweights)
```

Listing 3.2: Function to calculate and set JME-weights.

3.1.5 Smoothing factor

For most of the conventional single method inversions a smoothing operator is chosen to be the regularization matrix as outliers are generally smoothed out and therefore the images of the subsurface appear to be less noisy in comparison with pure damping. This is taken into account in this implementation of the entropy constraints by enabling the inclusion of additional smoothness constraints in the regularization matrix. pyGIMLi already has a pre-implemented setting to set up a regularization matrix which holds smoothing and damping operator. Figure 3.3 shows how such a regularization matrix could look like. The diagonal matrix which is responsible for the damping is attached to a first-order smoothness operator such that the 20 columns and the last 20 rows of the resulting matrix refer to the model parameters, while the remaining rows refer to the internal boundaries of the mesh that are subject to the smoothing constraint. Furthermore, this implementation allows for multiplication of a model weighting vector from the right-hand side referred to as *MWeights* or a constraint weighting vector from the left-hand side (*CWeights*). While the *MWeights* solely weight every constraint on each model parameter, *CWeights* allow for the individual weighting of every single constraint, in this scenario a different weighting of smoothness constraint and damping. Therefore, the latter are more suitable to introduce the entropy constraints into the inversion instance.

In Listing 3.2 this can be seen after the calculation of the model weights (lines 17-24) as the entropy weights are used to set the bottom elements of the *CWeights*. The upper elements in the *CWeights* are all set to a constant value which consists of the product of the mean magnitude of the entropy weights and the smoothing factor α. In that way it can be assured that for α close to 1 smoothing and damping constraints have a similar strength, meaning that both constraints contribute to the parametric functional similarly strong. When α is set to zero the whole upper part of the constraint matrix simplifies to a zero matrix meaning that no smoothness constraint is applied. The influence of the smoothness constraint can be increased by choosing a higher smoothing factor. The effects and benefits of this additional smoothing is further discussed in the following Chapter 4 (Synthetic study).

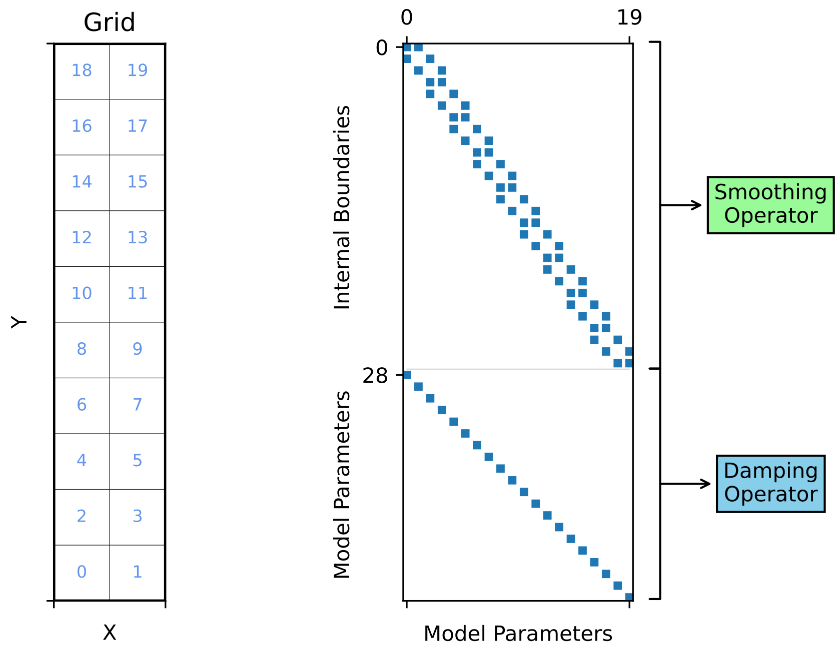

Figure 3.3: A simple 2D model domain (left) and the corresponding constraint matrix for smoothing and damping (right). The numbers indicate the index of each cell. The matrix shows non-zero matrix entries as blue markers and consists of a first-order smoothness operator and a damping operator (identity matrix). Within pyGIMLi this type of constraint is referred to as *cType=10*.

3.2 Example of model weights

To illustrate the concept of the joint minimum entropy approach, some first order ME and MEG weights of simple 2D models are calculated using the equations used in the *JointEntropyInversion()* class. Furthermore, JME and JMEG weights are presented to illustrate the method weighting factor.

3.2.1 Single-method weights

Consider the simple 2D models presented in Figure 3.4, namely a homogeneous model, a gradient model and a block model. As seen in the governing equations in Listing 3.2, the weight calculation requires a reference model. For this simple demonstration, the homogeneous model is set as the reference model for all three models. The second row of Figure 3.4 shows the resulting ME weights of the corresponding models. As expected, the homogeneous model has homogeneous ME weights as it is identical with reference model everywhere. The gradient model shows higher weights in regions where it is closer to the homogeneous reference model and lower weights where the gradient has strongly differing model parameters with respect to the reference model. The same observation can be made for the block model as the anomaly results in lower weights as the surrounding model space that is identical with the reference model. Since the entropy weighting is within the frame of damping, this means that regions of the model that are close to the reference model are stronger damped towards the reference model and vice versa. Therefore, the ME weighting leads to the development of few stronger anomalies rather than several smaller ones which coincides with a decreased model entropy.

At the bottom of Figure 3.4 the corresponding MEG weights are shown. The homogeneous model results once again in homogeneous weights since the model contrast and the model gradient is constant everywhere. The gradient model weights appear to be very similar in the structure since the gradient is constant but the model difference with respect to the reference model follows the same trend as in the ME weights. Therefore, we find that the part in front of the logarithm in eq. 2.43 defines the structure of the weights. The block model appears to be a little bit more complex. We find the smallest MEG weights inside the anomalous block due to the strong contrast in model parameters. The strong gradients at the boundaries of the anomaly cause greater model weights. Around the anomaly there is no model contrast and no gradient resulting in the same magnitude of MEG weights as the corresponding ME weights. In the context of damping this already indicates that the MEG approach is not as intuitive as the MEG weighting. Considering the block model with the MEG weights, the boundary of the anomaly would be damped relatively strong to the reference model while the inside as well as the outside show considerably less damping meaning that model parameter changes with respect to the reference model are promoted in these regions which can not be referred to the concept of entropy as easy as the ME weighting.

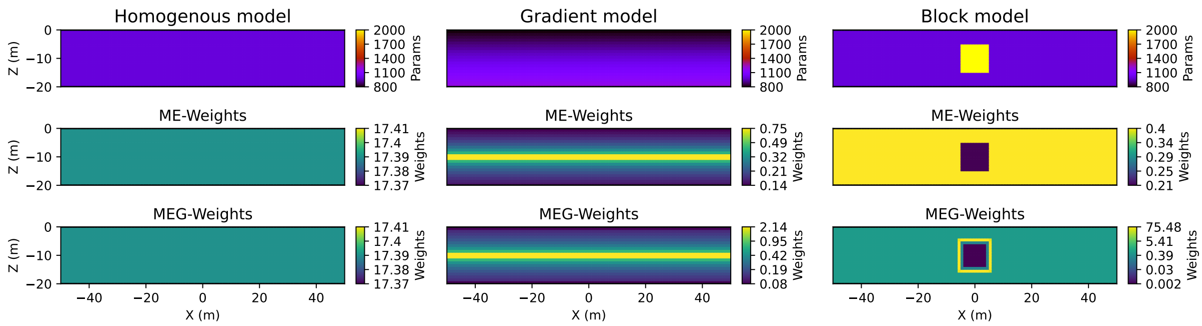

Figure 3.4: Illustration of ME weights (middle row) and MEG weights (bottom row) of three simple 2D models (top row). The reference model for all three models was set to the homogeneous model. ME weights are more intuitive as regions of high model contrast have smaller weights and are therefore less damped. Note that following parameters were fixed: $q = 1$, $\beta = 1e-5$.

Since Figure 3.4 displays the ME weights solely for order $q = 1$, Figure 3.5 presents a comparison of ME weights of the gradient model for different orders. Order $q = 1$ shares the behaviour of the first order expression as regions close to the reference model show bigger weights and are therefore damped strong to the reference model. However, for the third order expression the behaviour of the model weights are the exact opposite. The central part of the model that is close to the reference model appears to have small weights which will ultimately promote stronger parameter changes while regions with a relatively big model contrast are damped to the reference model. This would lead to an increasingly flat entropy spectrum as strong model contrasts are damped while small ones are promoted. The cause of this reversed behaviour is the term in front of the logarithm in eq. 2.42 which is approximately proportional to $|\mathbf{m}(\mathbf{r}) - \mathbf{m}_{\mathrm{ref}}(\mathbf{r})|^{q-2}$. In order to obtain the desired behaviour of the resulting weights, this would limit the choice of order to a maximum of $q = 2$. It is possible that this limitation is introduced by the pseudo-quadratic expression (eq. 2.40) that allows the use of existing inversion frameworks. Unfortunately, Zhdanov et al. (2022) do not discuss this when presenting the approach. However, they only present results up to order $q = 2$ which could indicate this limitation. This observation suggests to choose an order of $q \leq 2$ to avoid any complications related to this issue and therefore only first and second order expressions are considered within this work.

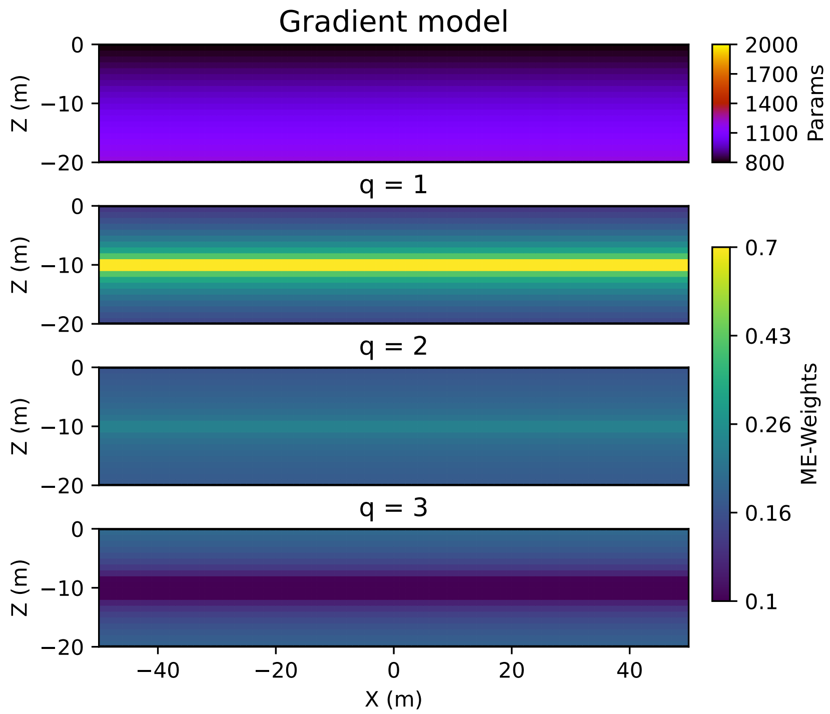

Figure 3.5: Illustration of ME weights of the gradient model using the homogeneous model as reference (3.4). The three rows of ME weights refer to orders q.

3.2.2 Multi-method weights

Now consider two different methods that are used to reconstruct different physical model parameters. Figure 3.6a and Figure 3.6b present two different models that show a rectangular anomaly of different strength. To better show the effects of the JME and JMEG weights along with the method weighting the anomalies are slightly shifted with respect to each other. Note that the reference model is a homogeneous model with a value of the background of both models.

First consider the JME weighting approach presented in Figure 3.6a. The second row presents the JME weights of model 1 and model 2 without method weighting. It can be seen that in addition to the region of the anomaly of the method itself also the anomaly of the other method appears with low weights. This means that during the joint inversion model changes with respect to the reference model are promoted where any of the methods already have a strong contrast. The lowest weights can be found in the region where the anomalies are overlapping meaning that parameter changes are encouraged in that region. Therefore, this will produce similar structure in both models during the inversion. The bottom two rows present the JME weights with a stronger method weighting on either model 1 or model 2. It can be observed that the anomaly of the higher weighted method is more dominant in the resulting model weights. This will cause the weaker weighted model to become more similar to the higher weighted. However, with increasing method weighting this rather flexible exchange of structural information will lead to a strong structural constraint on the weaker weighted method such that the exchange of structural information is only in one direction. A big risk of this is that possible inversion artefacts, like ray artefacts or other features created by noisy data, are enforced on another method making the inversion results rather worse than better. Therefore, it is suggested to use this method weighting with caution and only with small weighting factors to avoid running into these issues related to structural enforcement.

Figure 3.6b presents the corresponding JMEG weights. As already mentioned for the interpretation of the MEG weights (Figure 3.4), the entropy gradient weights are more complex and less intuitive. This becomes clearer when considering joint entropy gradients. Similar to the JME weights, structural information of the other method can be observed in the model weights of a method. However, solely the edge of the anomaly is contributing to the logarithm part of the JMEG weight expression (eq. 2.45) and therefore the anomaly boundaries of one method are more or less present in the model weights of the other depending on the specific method weighting. It is not clear what structures will be promoted by a model weight structure like this as some regions inside the boundaries of the other method are weighted equally as the outside. Note that the method weights have considerably higher values in order to show significant effects in the JMEG weights. This is probably caused by the very strong gradients at the edges of the anomalous rectangles. This simple demonstration already indicates that the use of JMEG weights is limited due to the complex behaviour and bad predictability of the weighting.

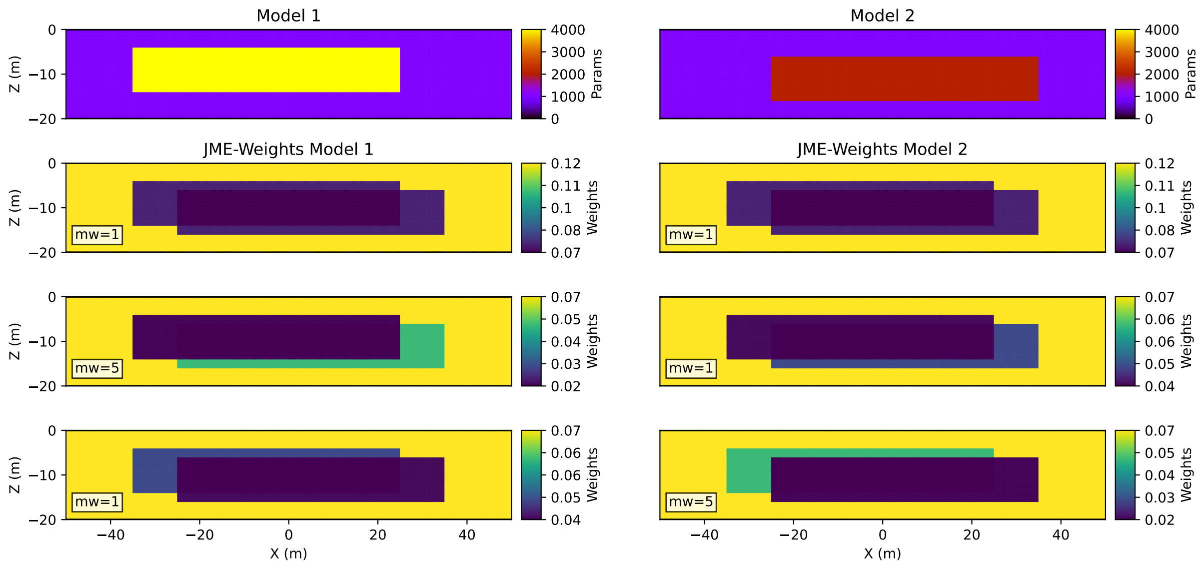

(a) JME

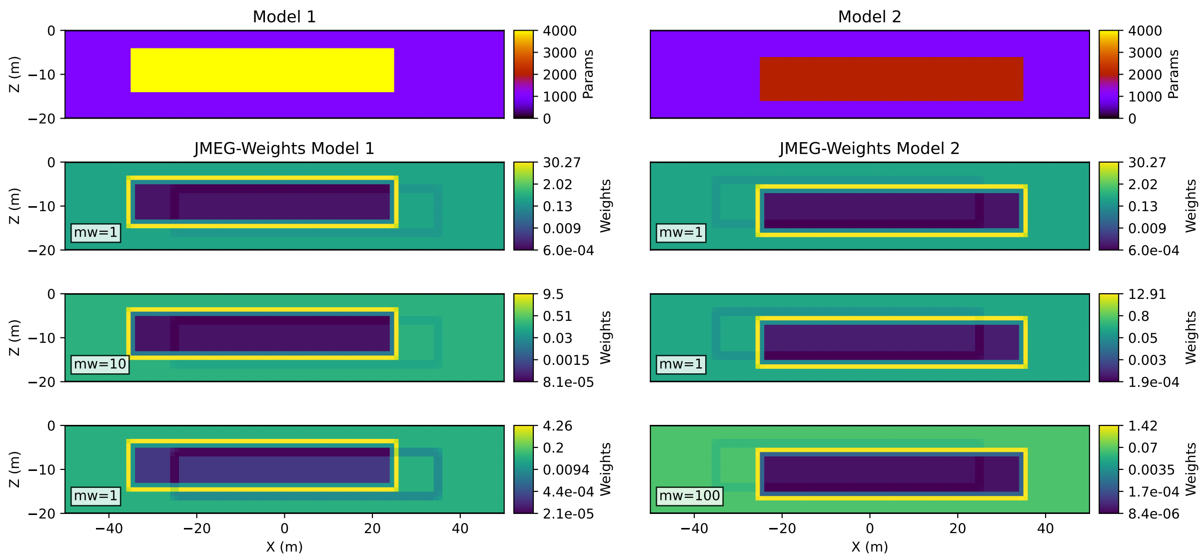

(b) JMEG

Figure 3.6: Example of joint minimum entropy (a) and joint minimum entropy gradient weights (b) for simple 2D models. The reference model is a homogeneous model. The rows correspond to related weights. the method weighting factor for both models are indicated by the text box in bottom left corner of each model weights plot. Note that following parameters were fixed: $q = 1$, $\beta = 1e-5$.

4

Synthetic study

Contents

In this chapter the joint minimum entropy and joint minimum entropy gradient constraints are applied to a two method, two dimensional geophysical imaging problem. The governing parameters introduced in Chapter 2 (Theory) and Chapter 3 (Method) are tested on synthetic ERT and SRT data. Section 4.1 presents the synthetic data generation and afterwards conventional smoothness-constraint inversion results as well as standalone entropy constraint results and joint inversion results will be presented. The inversion parameters for all presented results are summarized in Table A.1.

4.1 Synthetic data generation

For this synthetic 2D model study the ERT and SRT methods are considered. Therefore, a velocity model as well as an electrical resistivity model are constructed. Since the goal of this study is to investigate joint inversion, both models should be structurally similar. The models were chosen as seen in Figure 4.1. Both models show the same two anomalous bodies, namely a square on the left and a circle on the right. However, to make it a little more realistic the models are also differing in some aspects. The background resistivity is chosen to be constant at 700 Ωm while the velocity background shows a high velocity layer (4000 m/s) underneath a low velocity layer (500 m/s). This is also beneficial to improve the ray coverage in the region of the anomalies during the forward calculation of the seismic traveltimes as the bottom layer is a good refractor (Kearey et al., 2002). Furthermore, it allows to investigate if the seismic data will enforce this layered structure in the ERT result during the joint inversion.

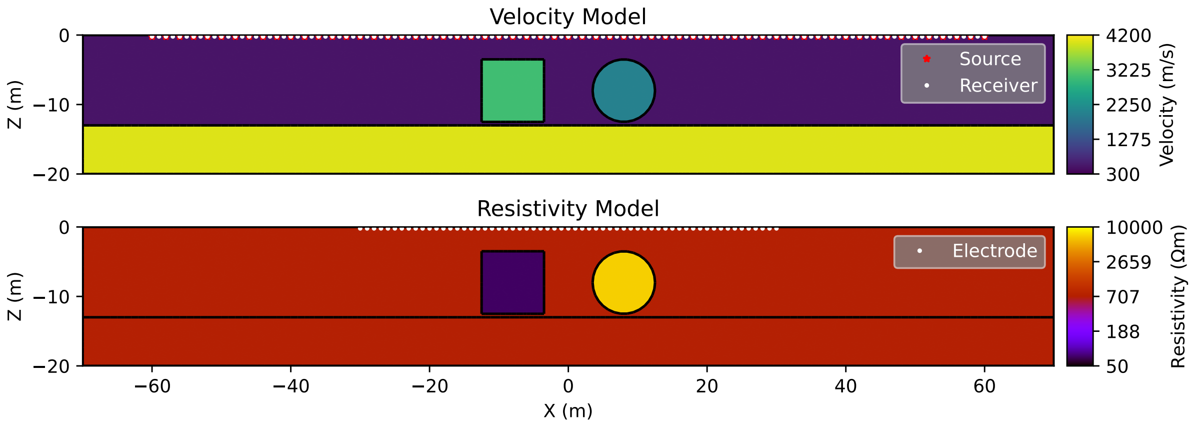

Figure 4.1: Seismic velocity model (top) and electrical resistivity model (bottom) that are used for the synthetic SRT and ERT data generation in pyGIMLi. Note that the structural similarity between the models is needed to justify a structurally-coupled joint inversion approach.

Figure 4.1 also shows the source and receiver locations used for the SRT data generation as well as all electrode locations for the ERT method. The acquisition spread of the SRT method is chosen to be twice as long as the electrode spread for the ERT method to improve the experimental design of the study. Note that in the following sections only the part between -30 m and 30 m are discussed as this is the region of the model domain that hosts the anomalies and that has good data coverage in both methods. All parameters required for the forward calculation can be found in Table 4.1. The resulting traveltime data and apparent resistivities are presented in Figures 4.2a and 4.2b, respectively.

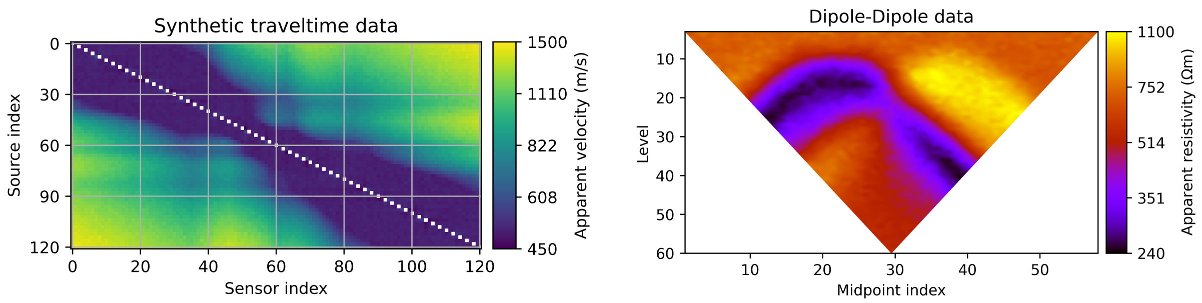

(a) Shown is the apparent velocity between each source-receiver measurement (i.e. source-receiver offset divided by the observed traveltime).

(b) Shown are the observed apparent resistivities (eq. 2.2). Note that the level refers to the distance between current and potential dipole.

Figure 4.2: Synthetic seismic data (a) and synthetic electrical resistivity data (b).

Table 4.1: Settings for forward computations.

Method	Parameter	Value
SRT	First sensor	- 60 m
	Last sensor	60 m
	Number of sensors	121
	Shot spacing	2 m
	Noise level	0.01 %
	Absolute noise	1 ms
ERT	Configuration	Dipole-Dipole
	First electrode	- 30 m
	Last electrode	30 m
	Number of electrodes	61
	Noise level	2.5 %
	Absolute noise	0.001 mV

4.2 Conventional inversion results

To establish a baseline result, conventional Tikhonov-regularized inversions are performed as derived in section 2.2. A first-order smoothing matrix was chosen similar to the one presented in eq. 2.21. The resulting resistivity and velocity distributions are shown in Figure 4.3. It also presents the starting model of each inversion instance in the top row of plots. Note that the starting model of the ERT inversion is a homogeneous model with a value of the mean of the apparent resistivities of the data. For the seismic refraction a gradient starting model was chosen with an increase of velocity from 500 m/s at the surface up to 4500 m/s at the bottom of the model domain. To ensure comparability of parameter tests and inversion approaches, these start models will be kept fixed throughout all inversions in this section.

Figure 4.3 shows that the ERT method is able to display the two anomalies quite well. The resistivity of the left anomaly is estimated accurately, however, the value of the right, circle anomaly is slightly underestimated. Furthermore, the image indicates a rather straight upper boundary of the left anomaly opposing to the rather round boundary of the right anomaly. However, the boundaries of the anomalies, especially the bottom boundaries, are smoothed out quite strongly due to smoothness-constraints in the regularized inversion scheme. The predicted velocity image on the other hand is recovering the synthetic model not as good as the bottom refractor is not presented as a continuous layer and the circle anomaly is not fully recovered. However, the left anomaly is represented quite accurate as value and location is very close to the true model. As already observed for the resistivity image, the velocity model is blurred out due to the smoothness constraint.

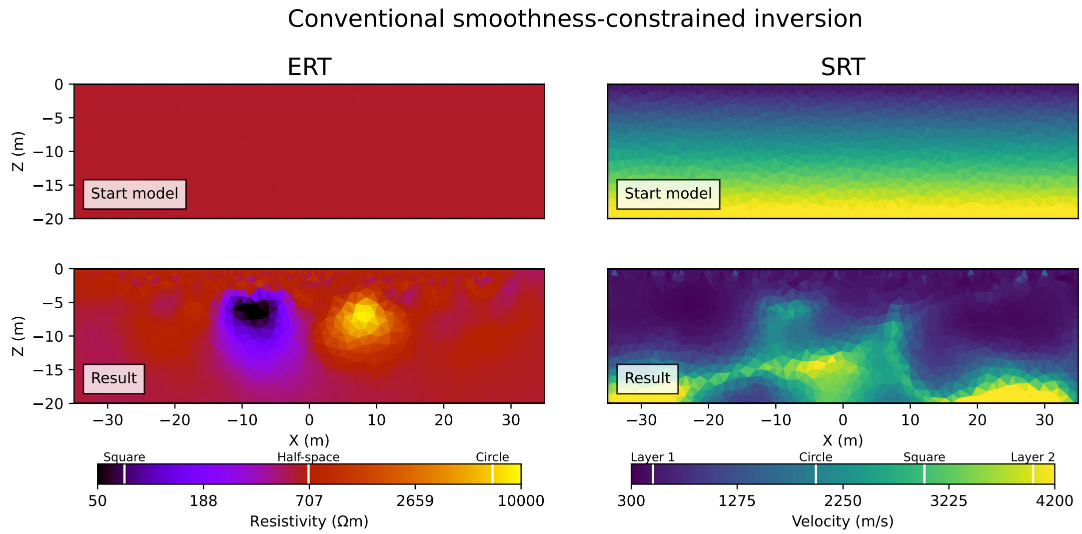

Figure 4.3: Conventional smoothness-constrained inversion results (bottom) of ERT and SRT method with their respective starting model (top).

4.3 Parameter tests

Before the joint inversion will be performed, tests of the most influential parameters are tested to determine suitable settings for the joint minimum entropy approach. Therefore, the following sections present tests of the regularization parameter λ, smoothing factor a and the order q. There are no parameter tests presented for the numerical stabilizer β as it has little to no effect on the final outcome if chosen much smaller than the model parameters. For all following inversions a value of $\beta = 1 \cdot 10^{-10}$ is kept fixed.

4.3.1 Regularization and smoothing parameters

4.3.1.1 Minimum entropy stabilizers

Standalone ME inversion results of the synthetic ERT and SRT data are presented in Figure 4.4 and Figure 4.5, respectively. Note that these results are obtained for an order of $q = 1$. Figure 4.4 presents the final inversion results for three different λ (columns) and three different a (rows). In the first row results with no smoothing are presented. Overall, the results appear to have several outliers resulting in a noisy image. The bottom two rows have smoothing which results in clearer, less noisy images as outliers are suppressed. It can be observed that an increasing a and an increasing λ for a fixed smoothing factor causes the magnitudes of the anomalies to be damped. Therefore, a high smoothing factor with a low λ (bottom left) might produce a similar result as a higher λ with a smaller a (center). Furthermore, strong smoothing leads to a similar result as the conventional smoothness constraint inversion as the influence of the entropy damping is vanishing. Another observation is that, without damping, an increasing λ increases the magnitude of the anomalies as well as of outliers. This is related to the increased influence of the regularization term in the objective function of the inversion, which in this case promotes changes in regions where there is a contrast with respect to the reference model. It is important to note that for a high λ of 0.1 models with a worse data fit are produced which indicates that this choice of regularization parameter is too high. Figure 4.4 suggests suitable ranges for λ and a to be between 10^{-5} to 10^{-2} and 0 to 25, respectively.

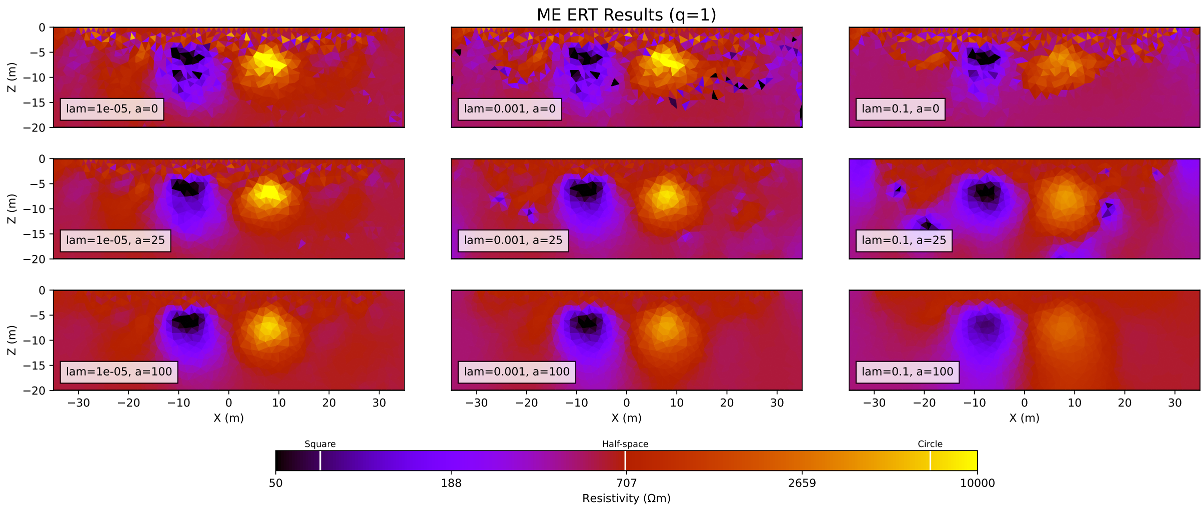

Figure 4.4: ERT ME Results for three different smoothing factors a and three different regularization parameters λ and order $q = 1$.

In Figure 4.5 different results for SRT ME inversions are presented. Similar to Figure 4.4, no smoothing results in very noisy results as the images do not indicate any clear structures. With increasing regularization parameter, less model cells show outliers resulting in only few high-velocity cells and many low-velocity cells for the highest tested λ. Similar to the ERT results, better results are obtained for additional smoothing, however, it can be seen that the SRT method generally requires stronger smoothing to obtain reasonable results. A possible reason for that might be, that the entropy constraints collapse high-velocity structures to smaller, even higher velocity structures that bundle many ray paths. Therefore, smoothing is needed to counteract this behaviour and obtain reasonable models. Furthermore, the results for $\lambda = 10^{-5}$ are generally not very clear and worse than the results for higher λ values. Therefore, a regularization parameter between 10^{-3} and 10^{-1} is suggested together with a smoothing factor between 50 and 200.

4.3.1.2 Minimum entropy gradient stabilizers

Figure 4.6 and Figure 4.7 present MEG results equivalent to the two previously discussed figures. Note that the λ values are chosen two magnitudes smaller to obtain comparable results. The ERT Results (Figure 4.6) show once again that a smoothing factor of $a = 0$ is not preferable as several strong outliers can be observed in the results. It appears that an increasing λ is enhancing this

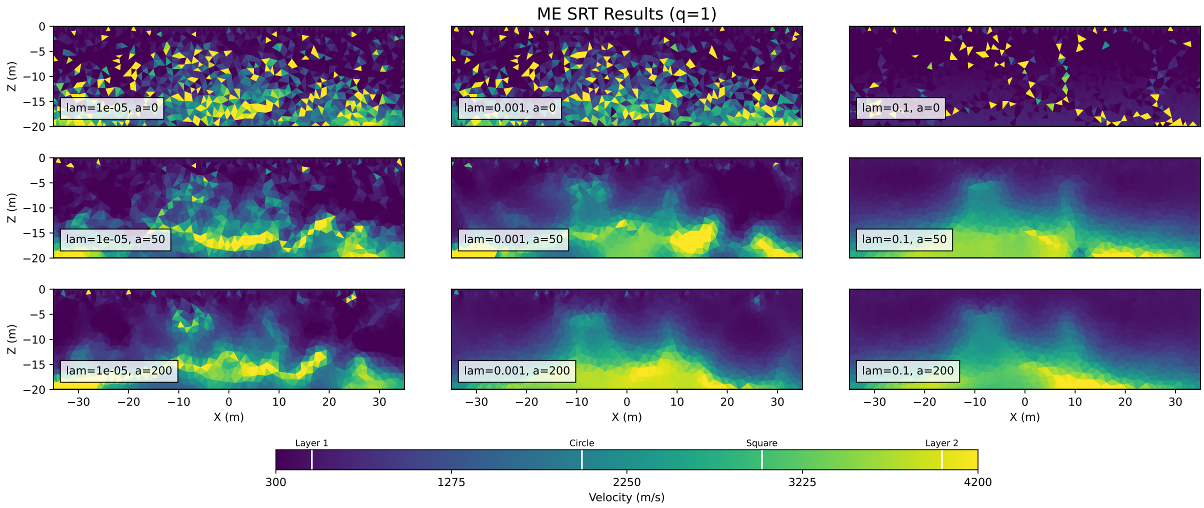

Figure 4.5: SRT ME Results for three different smoothing factors a and three different regularization parameters λ and order $q = 1$.

effect and causing increasingly more outliers. However, increasing smoothing counteracts this and produces similar good results with few additional outliers with respect to the ME inversion results. These results suggest a λ between 10^{-7} and 10^{-5} along with a smoothing factor between 25 and 100.

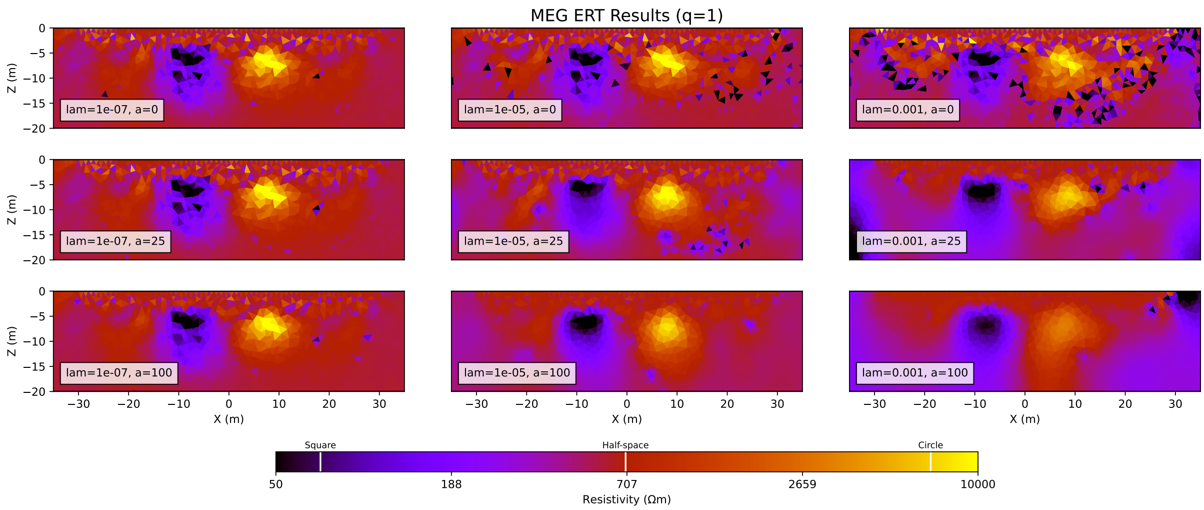

Figure 4.6: ERT MEG Results for three different smoothing factors a and three different regularization parameters λ and order $q = 1$.

Figure 4.7 confirms the observations of the previous discussed figures. For the SRT method stronger smoothing is required to avoid pure noise in the final images. Howeveer, it appears that the MEG approach is not as suitable for the SRT inversion as the ME approach as the results are not as clear. Also, a change in a or λ leads to strongly differing results. In combination with the worse data fit for most of the MEG Inversions, this indicates that the MEG approach is not preferable for SRT inversions. However, as seen in Figure 4.7, some settings produce reasonable results that are comparable to the ME results (bottom left, center right).

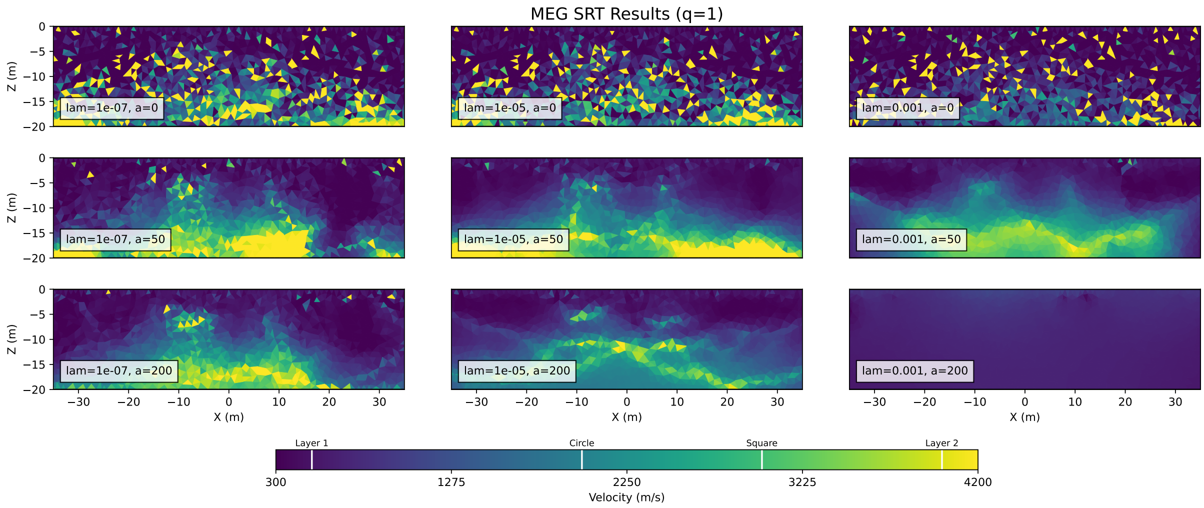

Figure 4.7: SRT MEG Results for three different smoothing factors a and three different regularization parameters λ and order $q = 1$.

4.3.2 Order

4.3.2.1 Minimum entropy stabilizers

To investigate the effects of the order of the entropy expression, the previously discussed figures are replicated for order $q = 2$. Figure 4.8 presents the second order equivalent to Figure 4.4. It can be seen that the second order results show slight improvements to the first order results as the background appears more homogeneous. A possible reason for that could be that the second order entropy expression is promoting changes only in regions where comparably strong model contrast are occurring. Therefore, small contrasts related to noisy data or sensitivity artefacts are more damped towards the background such that only the strong anomalies are promoted for parameter changes. Also, The anomaly magnitudes are higher than in the first order results which also leads to better reconstruction of the actual anomaly values, especially when stronger smoothing is applied.

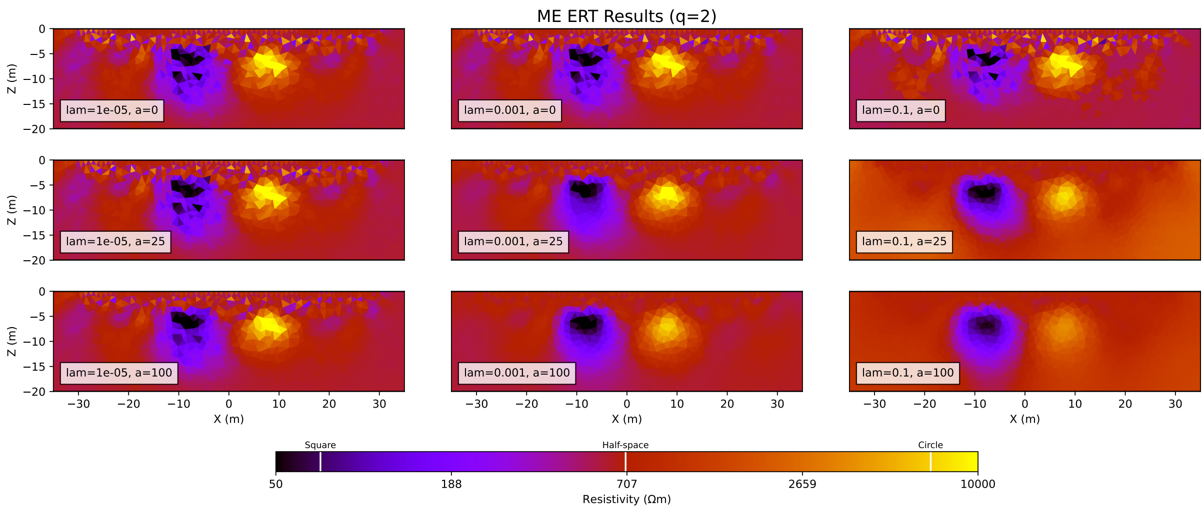

Figure 4.8: ERT ME Results for three different smoothing factors a and three different regularization parameters λ and order $q = 2$.

The SRT ME results for the second order are presented in Figure 4.9. The top right result illustrates the previously mentioned effects of the regularization parameter λ as high-velocity cells seem to be collapsed to the main ray paths. In comparison to the first order results (Figure 4.5, a regularization parameter of 10^{-5} and 10^{-3} requires stronger smoothing in order to obtain comparably good results. Especially the bottom high-velocity layer is not as good imaged as in the first order results. However, there are subtle improvements for $\lambda = 10^{-1}$ as the bottom layer as well as the right anomaly are imaged slightly better. This suggests for the second order ME inversion of the SRT data a slightly higher λ and similar a with respect to the first order settings.

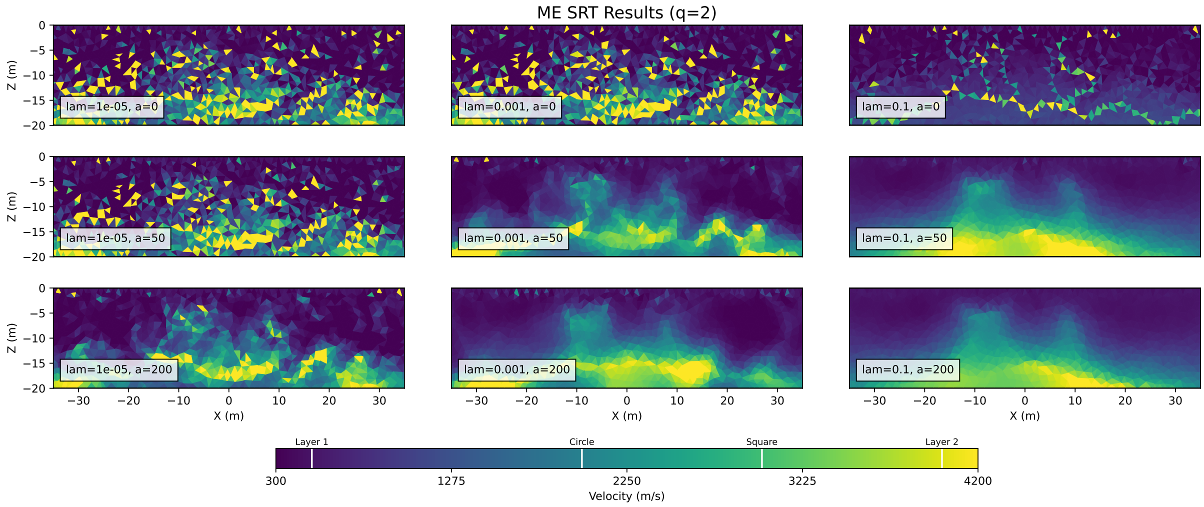

Figure 4.9: SRT ME Results for three different smoothing factors a and three different regularization parameters λ and order $q = 2$.

4.3.2.2 Minimum entropy gradient stabilizers

Figure 4.10 and Figure 4.11 present the second order results of the MEG approach. The ERT results in Figure 4.10 still show considerably many outliers for higher λ values and only few improvement to the respective first order results. It can be observed that for low λ values there is little to no changes while for higher regularization parameters the background appears slightly more homogeneous.

The second order MEG results of the SRT data inversion are presented in Figure 4.11. As already observed for the first order equivalent (Figure 4.7), the results are considerably worse than the ME results and no significant improvement can be observed with respect to the first order equivalent. Results are changing drastically with changed parameters and reasonable results are solely obtained for strong smoothing.

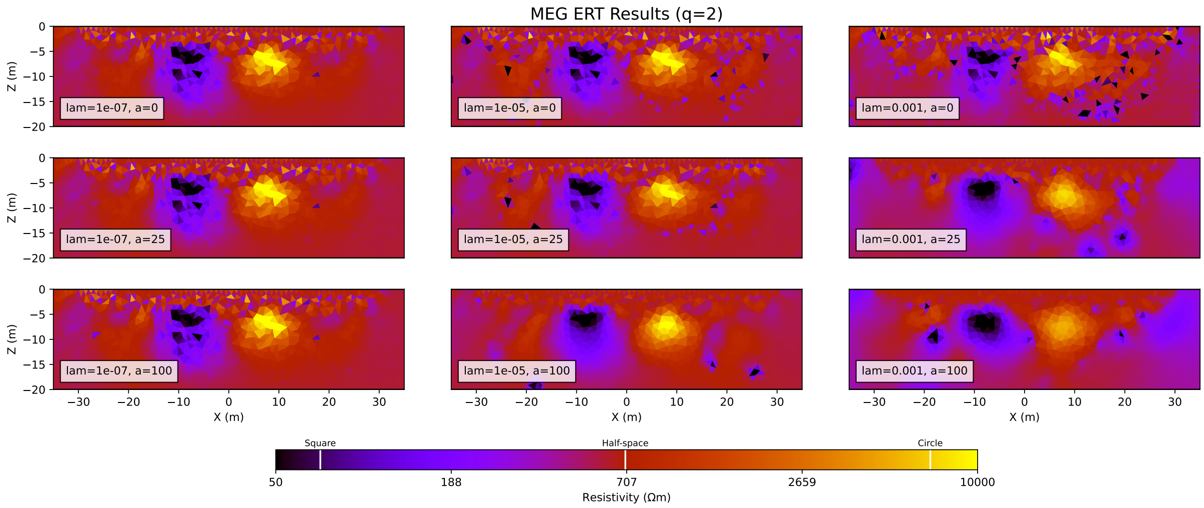

Figure 4.10: ERT MEG Results for three different smoothing factors a and three different regularization parameters λ and order $q = 2$.

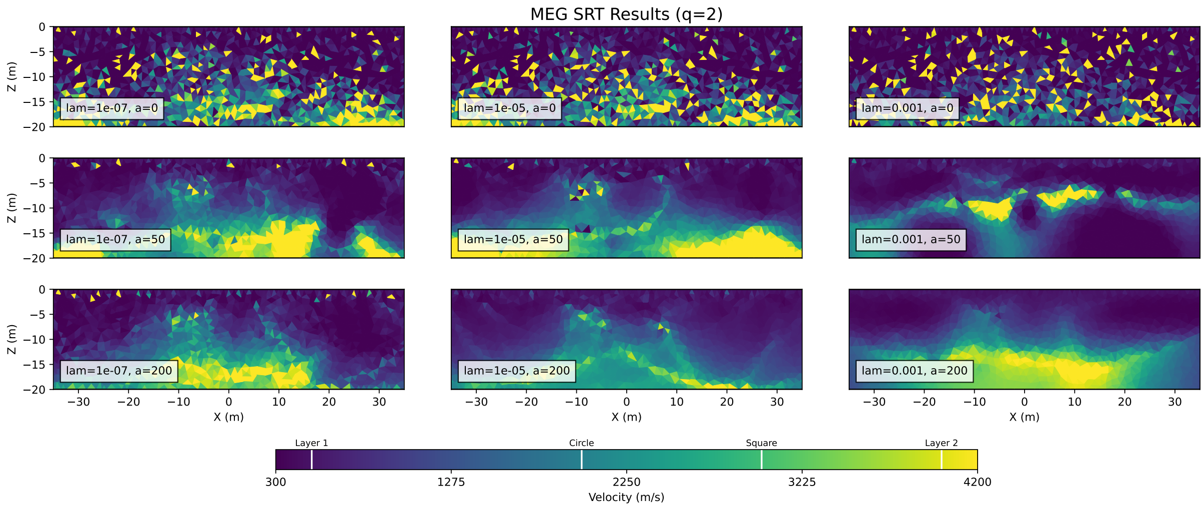

Figure 4.11: SRT MEG Results for three different smoothing factors a and three different regularization parameters λ and order $q = 2$.

4.4 Comparison between standalone and joint inversion results

Based on the standalone ME and MEG inversions in the previous section, suitable parameters are chosen to perform joint inversions.

4.4.1 Joint minimum entropy (JME)

Figure 4.12 presents a comparison of the estimated resistivity and velocity models (Figure 4.12a) based of conventional, first-order standalone ME and first-order JME inversion as well as the corresponding data misfit (Figure 4.12b). For the ERT inversions regularization parameters $\lambda_{\text{ERT}} = 0.003$ and $\lambda_{\text{SRT}} = 0.01$ and smoothing factors $a_{\text{ERT}} = 15$ and $a_{\text{SRT}} = 90$ are chosen.

As already mentioned, the conventional inversion is able to retrieve the resistivity distribution pretty well, however, it does not fully recover the true velocity model as the bottom layer and the right anomaly are not imaged properly. In contrast to that, the standalone ME SRT inversion result shows a more continuous bottom layer with a more dominant left anomaly. The right anomaly shows little to no improvements. The ERT result shows slight improvements in the imaging of the resistive circle as well as the bottom of the square anomaly. However, it seems to come with the drawback of a less homogeneous background.

For the joint inversion a unweighted scenario with method weighting factors of 1 for both methods and a weighted JME approach with double weighting on the ERT inversion are considered. The unweighted JME results show an improvement in the imaging of right anomaly for both methods. Especially in the ERT result the magnitude of the resistivity is more in accordance with the true model and the anomaly seems to be less smoothed. In the SRT results the left anomaly shows little to no improvements as it appears. However, the left conductive anomaly in the resistivity image appears to have two separated zones, namely a highly conductive zone at the top and a less conductive one underneath.

For a higher weighting on the ERT method there is no significant changes in the resistivity image, however, some changes can be recognized in the SRT result. The left anomaly now has a slightly higher velocity feature at the top that coincides with the location of the highly conductive region in the resistivity image. This illustrates that the weighted JME inversion promotes changes in the velocity image where strong resistivity contrasts occur. This could also explain why the right anomaly appears to be less present in the image in comparison with the unweighted scenario. In the SRT inversion the reference model is a gradient model that has approximately the seismic velocity of the right anomaly in the upper half of the circular anomaly. Therefore, the SRT inversion needs stronger damping in that region in order to recover the velocity of 2000 m/s properly. However, the ERT inversion produces lower weights in that region as there occurs a stronger model contrast. The stronger weighting of the ERT method then increases the influence of the resistive anomaly on the joint entropy calculation which ultimately leads to lower SRT weights within the right anomaly. This might cause the right anomaly to be imaged not as good as in the unweighted case. This illustrates that a higher weighting on one method might cause deterioration rather than improvements of the imaging.

For a proper comparison of the different results the data misfit should be taken into consideration (Figure 4.12b). The ERT results show very good data fit for all inversions with only slightly higher misfit levels for the standalone ME inversion. In contrast to that, there are clear differences between the SRT data fit. It can be seen that the fit of the conventional inversion appears to be the worst as misfit levels are slightly higher. Note that the small offset measurements close to the edges of the model domain have the highest data misfit. The misfit pattern already shows improvements for the standalone ME inversion and is best for the JME inversions. This is in accordance with the observations of the resulting velocity models. Therefore this indicates that the joint inversion had positive effects on the imaging of the seismic velocity structure.

In Figure 4.13 the second-order equivalent inversion results are presented. As already observed in the previous section, the second-order ME inversion performs better for the ERT inversion. This is confirmed by the improved misfit levels in Figure 4.15b. The ME SRT result shows slight improvements in the imaging of the left anomaly, however, the bottom layer is lacking continuity in comparison with the first-order results. Similar to the ERT JME results of Figure 4.12a there is little to no difference between the unweighted and unweighted JME inversion. However, in comparison to the first-order results we find improved imaging of the lower part of the left anomaly as well as a more homogeneous background. The biggest difference between the first- and second-order JME inversions is present in the SRT results. The left anomaly does show two high-velocity features at the top and bottom with a low velocity structure in between. The bottom layer appears more like an up-welling structure rather than a horizontal layer. This is also reflected in the corresponding data fit plots as they show an increased level of percentile misfit. This suggests that the first-order expressions are more suitable for the joint inversion of SRT data. A possible reason for that could be the previously mentioned behaviour of collapsed high-velocity zones that are promoted during the second-order ME weighting.

4.4.2 Joint minimum entropy gradient (JMEG)

As already observed in the previous section, the MEG approach does not show improvements in either the ERT nor the SRT inversion with respect to the ME approach. For completeness of the comparison of the approaches, Figure 4.14 and Figure 4.15 show MEG and JMEG results for first- and second-order. Generally, the ERT data fit is comparably good the ME and JME results in Figure 4.12b and Figure 4.15b, however, the resulting resistivity models show a less homogeneous background. The SRT results appear better for the second-order approach (Figure 4.15) in comparison with the first-order approach (Figure 4.14), however, the misfit levels are considerably worse in comparison to the ME and JME results. Furthermore. the resulting velocity models are not very consistent with the true model similar to the observations made in Figure 4.7 and Figure 4.11. Therefore, this illustrates again that the joint minimum entropy approach is not a suitable approach to jointly invert the data. Since the MEG and JMEG approach also requires more computational time due to gradient calculations, there appears to be no significant benefit of this method for the inversion of near surface geophysical data in comparison to the ME and JME approach. Therefore, Figure 4.14 and Figure 4.15 will not be discussed any further.

4.5 Conclusion

As all first and second order MEG and JMEG inversions generally result in a worse data fit as well as worse subsurface images with respect to their equivalent ME inversion results, this section suggests that the ME approach is a more suitable method to jointly invert the near surface multi-physics data sets. Therefore, the MEG approach will not be investigate further in this study and will not be considered for the following field data study. In contrast to the entropy gradient approach, the ME and JME could be used to successfully invert synthetic data. Therefore, this approach is chosen for the following field data study.

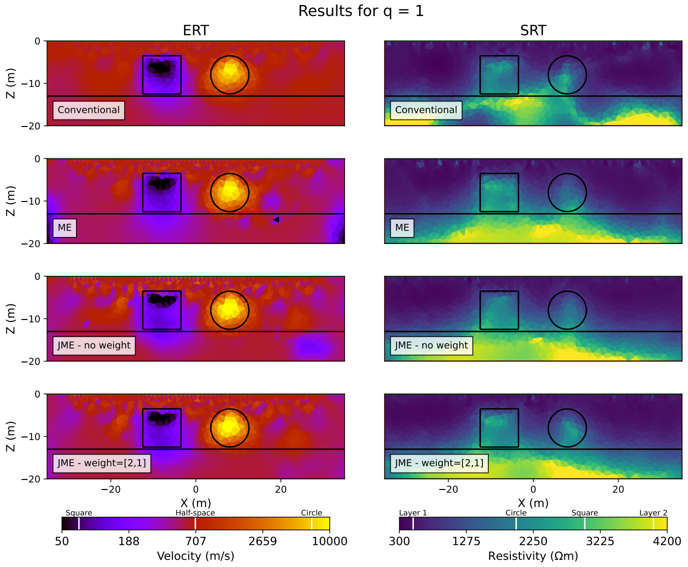

(a) Estimated electrical resistivity models (left) and seismic velocity models (right). The black lines indicate the true model structures.

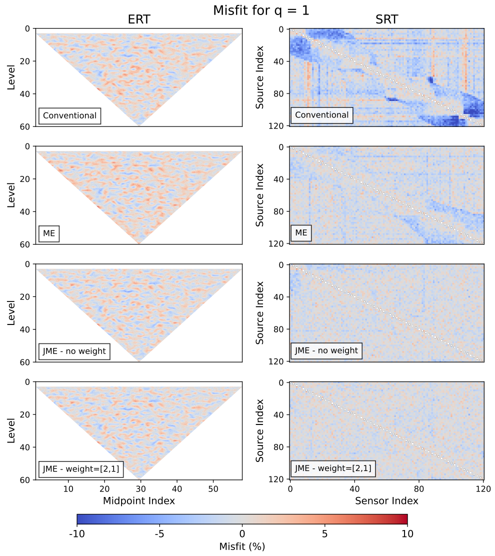

(b) Resulting data misfit in of ERT (left) and SRT (right) inversion results.

Figure 4.12: Comparison of conventional inversion, standalone ME inversion as well as unweighted and weighted JME inversion results of ERT and SRT data. Shown are the estimated model parameters of the last iteration (a) and the corresponding data misfit (b). The entropy have the following fixed parameters: $q = 1$, $\beta = 10^{-10}$, $\lambda_{\mathrm{ERT}} = 0.003$, $\lambda_{\mathrm{SRT}} = 0.01$, $a_{\mathrm{ERT}} = 15$ and $a_{\mathrm{SRT}} = 90$.

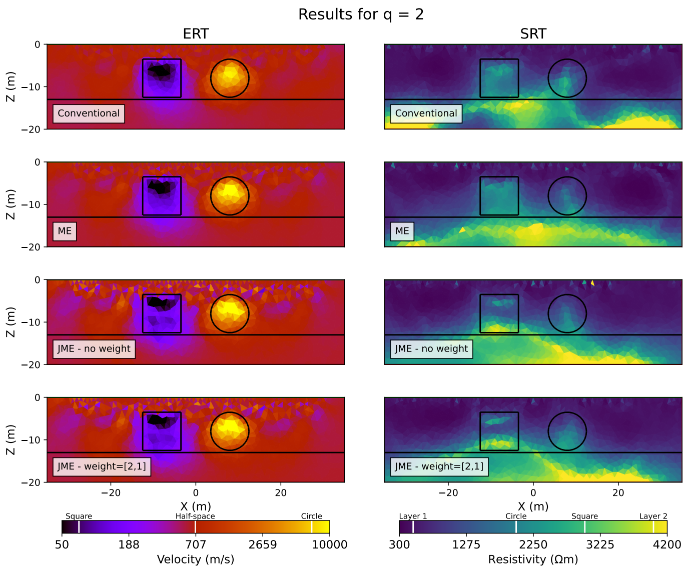

(a) Estimated electrical resistivity models (left) and seismic velocity models (right). The black lines indicate the true model structures.

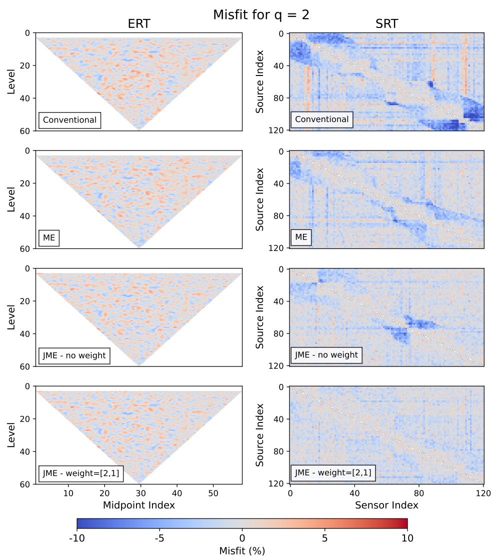

(b) Resulting data misfit in of ERT (left) and SRT (right) inversion results.

Figure 4.13: Comparison of conventional inversion, standalone ME inversion as well as unweighted and weighted JME inversion results of ERT and SRT data. Shown are the estimated model parameters of the last iteration (a) and the corresponding data misfit (b). The entropy have the following fixed parameters: $q = 2$, $\beta = 10^{-10}$, $\lambda_{\mathrm{ERT}} = 0.003$, $\lambda_{\mathrm{SRT}} = 0.01$, $a_{\mathrm{ERT}} = 15$ and $a_{\mathrm{SRT}} = 90$.

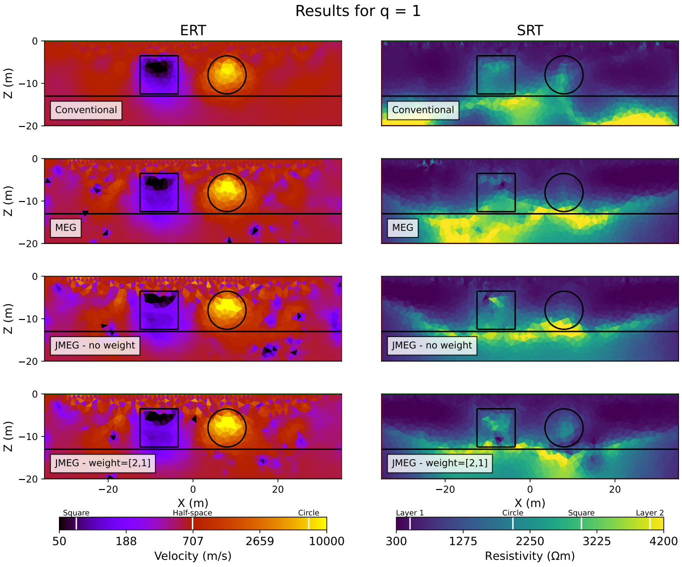

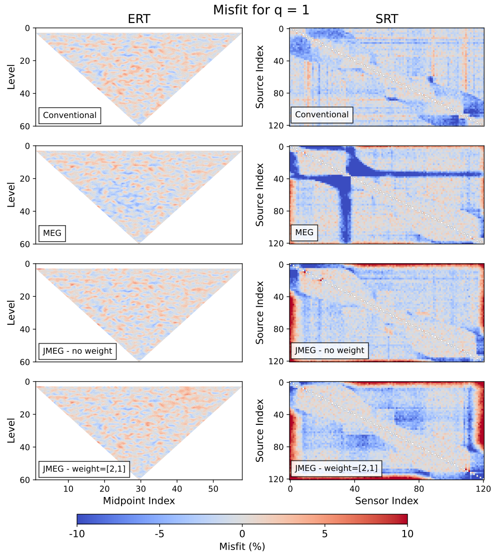

(a) Estimated electrical resistivity models (left) and seismic velocity models (right). The black lines indicate the true model structures.

(b) Resulting data misfit in of ERT (left) and SRT (right) inversion results.

Figure 4.14: Comparison of conventional inversion, standalone MEG inversion as well as unweighted and weighted JMEG inversion results of ERT and SRT data. Shown are the estimated model parameters of the last iteration (a) and the corresponding data misfit (b). The entropy have the following fixed parameters: $q = 1$, $\beta = 10^{-10}$, $\lambda_{\mathrm{ERT}} = 5 \cdot 10^{-6}$, $\lambda_{\mathrm{SRT}} = 5 \cdot 10^{-4}$, $a_{\mathrm{ERT}} = 20$ and $a_{\mathrm{SRT}} = 100$.

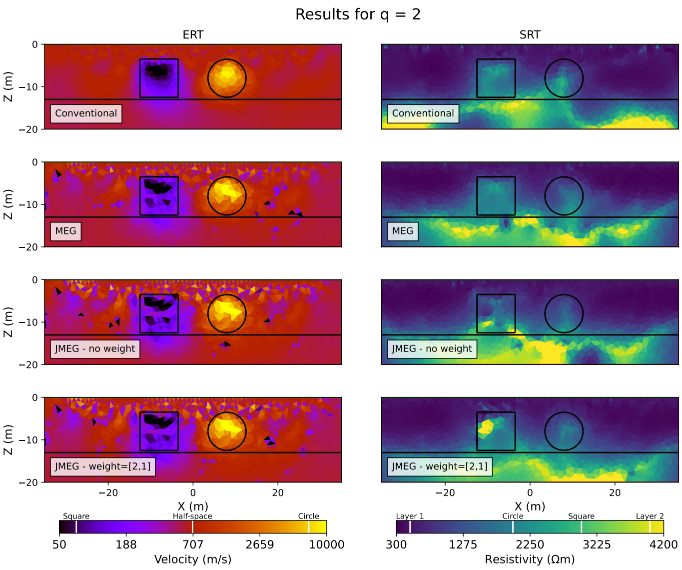

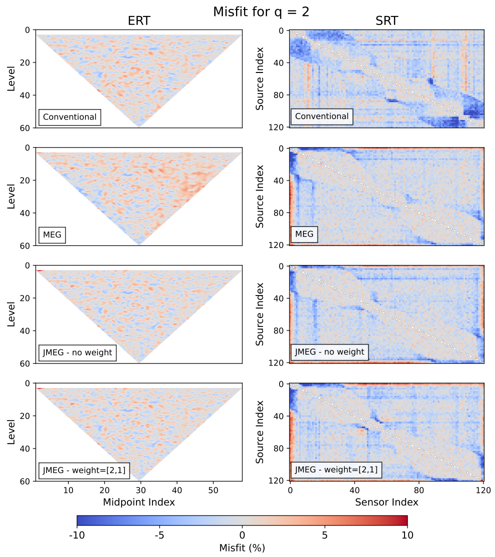

(a) Estimated electrical resistivity models (left) and seismic velocity models (right). The black lines indicate the true model structures.

(b) Resulting data misfit in of ERT (left) and SRT (right) inversion results.

Figure 4.15: Comparison of conventional inversion, standalone MEG inversion as well as unweighted and weighted JMEG inversion results of ERT and SRT data. Shown are the estimated model parameters of the last iteration (a) and the corresponding data misfit (b). The entropy have the following fixed parameters: $q = 2$, $\beta = 10^{-10}$, $\lambda_{\mathrm{ERT}} = 5\dot{1}0^{-6}$, $\lambda_{\mathrm{SRT}} = 5\dot{1}0^{-4}$, $a_{\mathrm{ERT}} = 20$ and $a_{\mathrm{SRT}} = 100$.

5

Field study: Rockeskyller Kopf

Contents

In this chapter the interest in the study area around the Rockeskyller Kopf, Germany is presented followed by the acquisition of ERT and magnetic data that will be used to create subsurface models of the suspected volcanic diatreme structure. First conventional and standalone ME inversions are performed which will be used as benchmarks for the joint inversion results with minimum entropy constraints. Results will be shortly discussed, interpreted and compared to previous studies of that area. Note that all parameters of inversions in this chapter are summarized in Table A.2. Additional 3D screenshots of the results using PyVista (Sullivan and Kaszynski, 2019) are provided in Appendix A.

5.1 Study Site

Strong volcanism shaped the western part of the Eiffel region in the last one million years. In some places remnants of these volcanoes can be observed on the surface, however, sometimes volcanic structures are covered by younger sediments, making them difficult to discover (Schmincke, 2009). The latter also holds true for the region that is investigated in this study. It is located northwest of the village Rockeskyll (Figure 5.1a) and is located close to the Rockeskyller Kopf volcanic complex, which consists of three monogenetic volcanoes (Shaw et al., 2010). This region is of special interest as huge sanidine crystals were found that indicate a phonolitic eruption close to a highly differentiated magma which is atypical for the region (Hopmann, 1914). Since the discovery of the crystals, several studies concerning the mineralogy and the related volcanism were conducted (Eilhard, 2009, 2018). The source is expected to be a volcanic diatreme structure that is located near by. It cannot be seen by morphological observations as surface erosion and fresh sediments buried the structure. This motivates the use of geophysical methods as these are able to sense a potential diatreme due to the change of physical parameters like electrical resistivity or magnetic susceptibility.

The first geophysical efforts are presented by Mertes (1983). He performed a magnetic mapping of the area to locate the volcanic source that produced the crystals along with phonolitic pyroclasts that were found. Within the region of interest a strong magnetic anomaly could be observed that was interpreted as the location of the volcanic diatreme structure that ejected the rocks. Several follow-up surveys using different geophysical methods were conducted by the University of Bochum with the aim to confirm the location of the volcanic diatreme structure through imaging of the subsurface. Boxberg (2011) and Mues (2013) performed a denser, more local magnetic mapping that is used for modelling of the magnetic anomaly. By data fitting of the observations they are able to identify a cylindrical structure that explains the observed anomaly. Plumpe (2015) and Gilberti (2020) performed ERT profiles cutting through the central part of the measured magnetic anomaly. They discovered a high resistivity feature at a depth of 5 to 10 m, however, the results were inconclusive and not consistent with the magnetic observations. Furthermore, a 3D SRT survey has been conducted to image the diatreme through the change of seismic velocity with respect to the surrounding sandstone. The study reveals a velocity anomaly that is approximately in the same area than the magnetic anomaly, however, due to uncertainties the data cannot fully confirm the structure that was modelled by Boxberg (2011). An additional 2D reflection seismic survey was performed but, like the ERT studies, no conclusive interpretation could be performed (Schneider, 2017). Therefore, the initial magnetic subsurface model is not properly confirmed by subsurface imaging yet and further studies are necessary.

As the previous studies solely focused on separate data inversion with the goal of a joint interpretation, the results are not consistent with each other, making a reliable subsurface interpretation more difficult. To overcome this issue, the newly developed joint inversion approach with joint minimum entropy constraints is applied to the field data with the aim to create more consistent multi-physics subsurface models that either confirm the model proposed by Boxberg (2011) or suggest a new one. It will also give insight to the suitability of the new joint inversion method for 3D field data applications. In this work previously acquired magnetic data (Boxberg, 2011) as well as newly acquired ERT data will be jointly inverted.

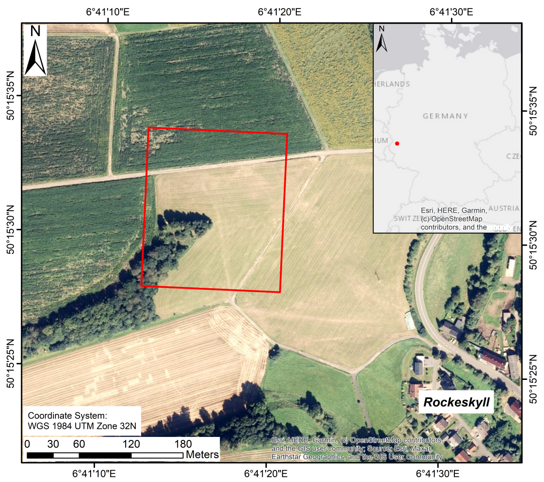

(a) Satellite imagery of the study site. Created with ESRI ArcGIS (Redlands, 2011).

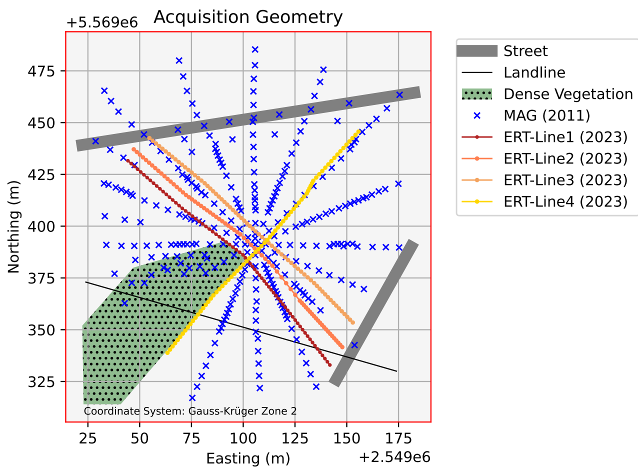

(b) Plot of the acquisition geometry and the main features of the study area.

Figure 5.1: Maps of the study area (a) and the acquisition geometry (b). The red dot on the top right map of (a) shows the location of the main map within Germany. The red rectangle indicates the position of (b). Note that the area of (b) appears slightly tilted in (a) due to a differing coordinate system.

5.2 Acquisition

5.2.1 Magnetics

Boxberg (2011) performed total magnetic field measurements using the proton magnetometer *ENVI-MAG*™ by the company *Scintrex*. The data was acquired radially around a central point that is coinciding with the central part of the strong magnetic anomaly mapped by Mertes (1983). The regions between measurement points with strongly varying field intensities were sampled more densely to better capture the changes of the magnetic field (Figures 5.1b, 5.2). As seen, the southwestern part of the area is not sampled as frequent due to the dense vegetation that makes the operation of the device more challenging. Furthermore, all point are georeferenced using a tachymeter which requires a clear path of sight between magnetic sensor and some reference point. Therefore, this also limited the ability to perform measurements in the densely vegetated area (Boxberg, 2011).

Figure 5.2 shows the interpolated topography based on the tachymeter measurements, as well as the observed total field anomaly and the estimated noise. It can be seen that the study area has a slope in N-S direction with approximately 30 m of elevation difference. It is important to include the topography in the inversions as it will influence the forward modelling response of the methods and therefore has a strong effect on the inversion. The natural background magnetic field measured at an observatory is needed to extract the total field anomaly. Boxberg (2011) uses a daily mean of the natural magnetic field of 48487.4 nT based on data measured by the Black Forest Observatory on the respective acquisition days. The processed data shows a strong magnetic anomaly of nearly 1500 nT. Due to the strength of the anomaly as well as the local extent, no further processing has to be performed. The magnetometer performs several measurements per location and returns the field intensity as the mean of the repeated observations. This also allows to get an estimate of the noise on the data by considering the standard deviation of the repeated measurements. The noise is used to calculate relative data errors which are additionally increased by 2% to weight the data during the inversion. The interpolated relative error is presented in Figure 5.2 on the right and shows reasonable values between 2% and 7%.

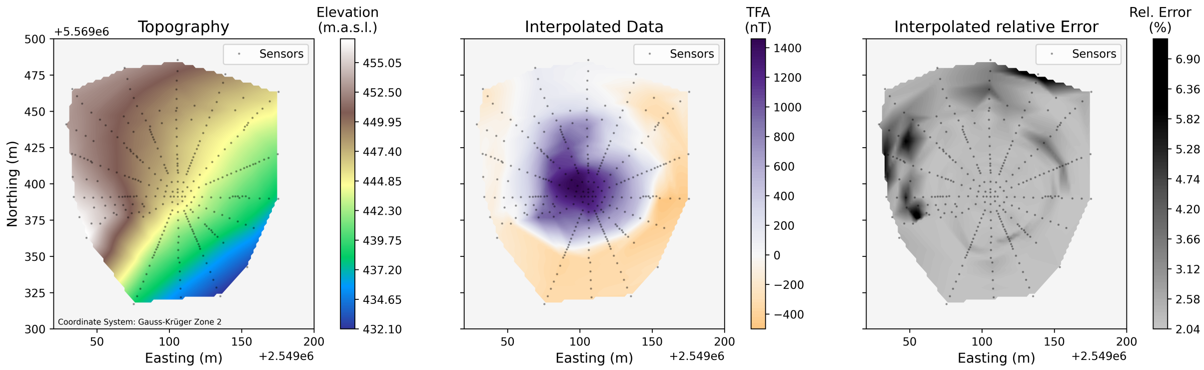

Figure 5.2: Overview of magnetic data acquired by Boxberg (2011). Shown are the interpolated topography based on sensor positions (left), the interpolated total field anomaly (middle) and the interpolated relative error. Note that the total field anomaly was determined with a background magnetic field of 48487.4 nT.

5.2.2 Electrical resistivity tomography

As only two ERT profiles were acquired prior to this study with inconclusive results, four new ERT profiles using a dipole-dipole configuration were acquired within this project. The dipole-dipole configuration was chosen for the reasons that were explained in Chapter 2 (Theory), namely a good horizontal resolution and its ability to be parallelized. The latter could be exploited since the device *Syscal Terra* by the French company *IRIS Instruments* was used, which uses up to 10 channels for parallelized data acquisition.

As seen in Figure 5.1b three lines are parallel to each other in NW-SE direction with a spacing of about 5-10 m and a fourth line intersecting them approximately perpendicular to gather better 3D information of the resistivity distribution of the subsurface. The lines were planned to cover the central part of the magnetic anomaly which allows the methods to investigate a similar subsurface volume. Several electrode positions were georeferenced using the GPS of a smartphone, resulting in a higher uncertainty than more elaborate GPS trackers or tachymeters. Unfortunately, no GPS device with a higher accuracy was available at the time to perform a better positioning. Therefore, the uncertainties of the positioning will mitigate into the geophysical inversion result along with the measurement errors.

Lines 1, 2 and 4 consist of 72 electrodes with a spacing of 2 m. For line 3 the last three electrodes had to be excluded due to the road in the southeast. Additional to the geometry assignment, some filtering has to be performed on the ERT data as Lines 1 and 4 showed anomalous values that are not related to the subsurface but to system malfunctions (Figure 5.3). During the measuring of these lines the batteries had to be changed from car batteries to internal batteries and back to another car battery. Due to these changes null measurements were taken that have to be excluded. Furthermore, line 4 shows a cloud of anomalous values toward the western end of the lines that are related to an anomalous electrode and probably to some influence of the landline crossing the electrode spread.

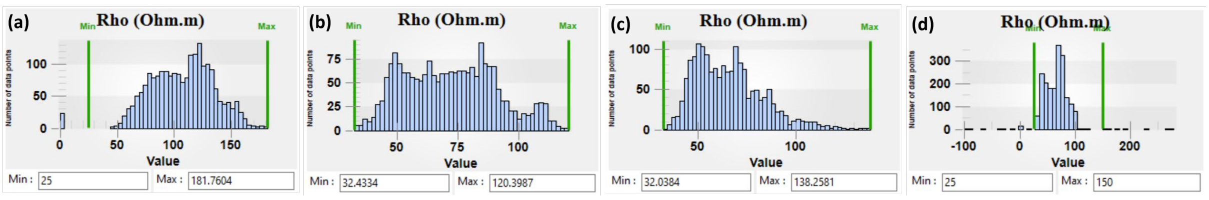

Figure 5.3: Histogram filtering of raw ERT data. (a), (b), (c) and (d) refer to lines 1, 2, 3 and 4, respectively. Only Lines 1 and 4 were subject to filtering. The vertical green markers indicate minimum and maximum apparent resistivity applied for the filtering.

The resulting filtered and processed data is shown in Figure 5.4. Line 1 and 3 appear very similar with slightly lower resistivities at lower levels and higher resistivities for deeper levels. Line 2 shows very resistive measurements towards the SE end of the line that occur at all levels. Since it is not present in the neighbouring lines it is possible that there was a near-surface, high resistive feature with a small lateral extent. Line 4 appears similar to lines 1 and 3 with the exception of higher apparent resistivities for deeper levels and on the east side of the pseudosection. Prior to the field measurements strong rain occurred in the study area such that the near surface was very wet which relates to the lower resistivities of the low level observations in the pseuosections. Furthermore, it can be assumed that electrodes generally have a good ground coupling which ensures improved data quality.

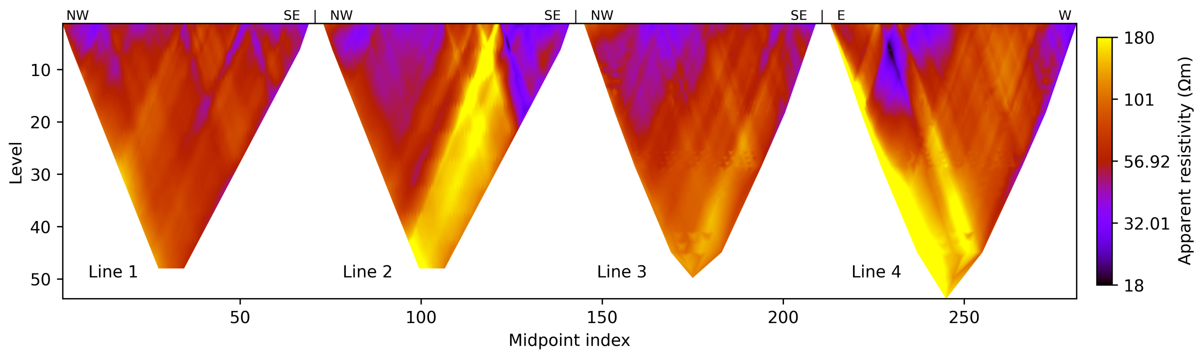

Figure 5.4: Pseudosections of ERT data acquired in 2023 after filtering and processing. The orientation of the lines are indicated with the capitals above the pseudosections.

5.3 Results

5.3.1 2D inversion

Before starting the 3D inversions, a 2D inversion of each ERT profile will be performed to get a first impression of possible subsurface structures. The 2D inversions are performed with a starting model that is a homogeneous model with an electrical resistivity of the mean observed apparent resistivities. As seen in Figure 5.3, all four profiles show similar apparent resistivities such that the resulting starting models are of resistivity 65.5 Ωm, 67.8 Ωm, 62.8 Ωm and 76 Ωm, respectively. All four inversions are performed using a first-order smoothing operator with a regularization parameter

$\lambda = 10$, resulting in an error weighted misfit of $\chi^2 < 1$. The imaged 2D electrical resistivity profiles are presented in Figure 5.5. Lines 1 to 3 show relatively consistent images with approximately 30 to 100 Ωm in the upper 15 m and a high-resistive structure underneath which appears shallower in the south. They also show a low-resistive feature at the bottom of the slope which could be related to moisture accumulation due to the rainfall prior to the measurements. The intersecting line 4 is in accordance with these observations, suggesting that the data is suitable for a 3D inversion.

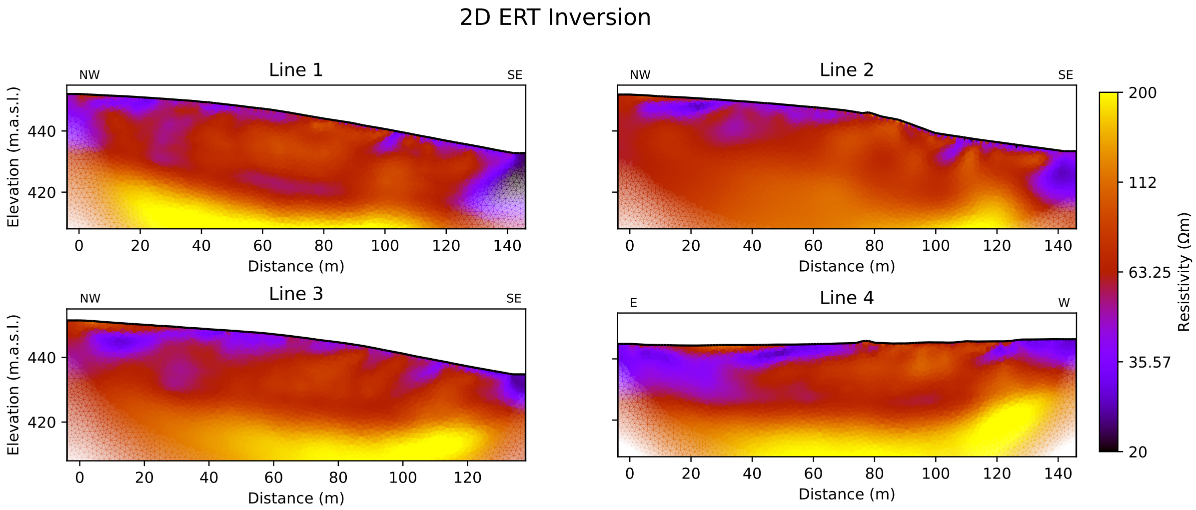

Figure 5.5: 2D inversion results of the four ERT profiles shown in Figure 5.1b. It can be assumed that near-surface resistivities are low due to rainfall prior to the ERT surveys.

5.3.2 Conventional inversions

For the 3D inversions an unstructured mesh is generated that replicates the surface topography based on the positions of the magnetic sensors (Boxberg, 2011). The mesh needed to be adjusted slightly to ensure that electrodes are at node locations while magnetic sensors are not on the nodes. The latter is a necessary requirement as the magnetic field gradients are calculated through a line method, which requires the observation points not to be on the edges or nodes of cells (Holstein et al., 2007).

The 3D ERT inversion result using the conventional first-order smoothing constraint is presented in Figure 5.6. Shown are the 2D sections that are extracted from the 3D resistivity model. All lines show a high-resistive feature at the bottom of the model reaching over 300 Ωm. In comparison to the separate 2D inversions (Figure 5.5), this feature is more present in the images, especially for line 2. In the 2D sections, the southern end of the slope shows a conductive feature, however, in the 3D result this feature only appears in the result of line 2 while the surrounding lines 1 and 3 show more conductive features. It is important to mention that the error weighted misfit χ^2 is around 6, which is a much higher value with respect to the 2D inversions. However, this is to be expected as the 3D inversion has less degrees of freedom, since the measurements of several lines are used to invert for the subsurface resistivities. This comes especially into play for the region below line 2 as the pseudosection, as well as the 2D inversion result, shows clear differences to the neighbouring lines.

The corresponding 3D magnetic inversion results are shown in Figure 5.7 and have a very good data fit of χ^2 close to 1. The results show a smooth magnetic susceptibility anomaly. The magnitude of the anomaly reaches 0.15 in its core while the surrounding host rock appears to have a susceptibility close to 0. It is important to mention that the model parameter range had to be limited during the magnetic inversion and therefore has a large influence on the appearance of the magnetic anomaly. Based on literature and previous investigations in the area, the susceptibility is limited to values between 0 and 0.15 (Lowrie and Fichtner, 2020; Boxberg, 2011). This explains the maximum susceptibility contrast that is observed in the anomaly.

An important observation is that both the ERT and the magnetic method show strong anomalies in their respective geophysical subsurface model. However, while the high-resistive anomaly appears to be more present in the central and southern part of the slope, the magnetic anomaly is more dominant towards the northern part of the lines 1 to 3. This observation illustrates the motivation of this joint inversion study quite well as the goal is to bring the two anomalies closer together. Since the magnetic inversion result is highly non-unique, a joint inversion has the potential to change the form and location of the anomaly significantly. It is important to mention that this can only be achieved when the underlying assumption holds that both methods sense a similar structure.

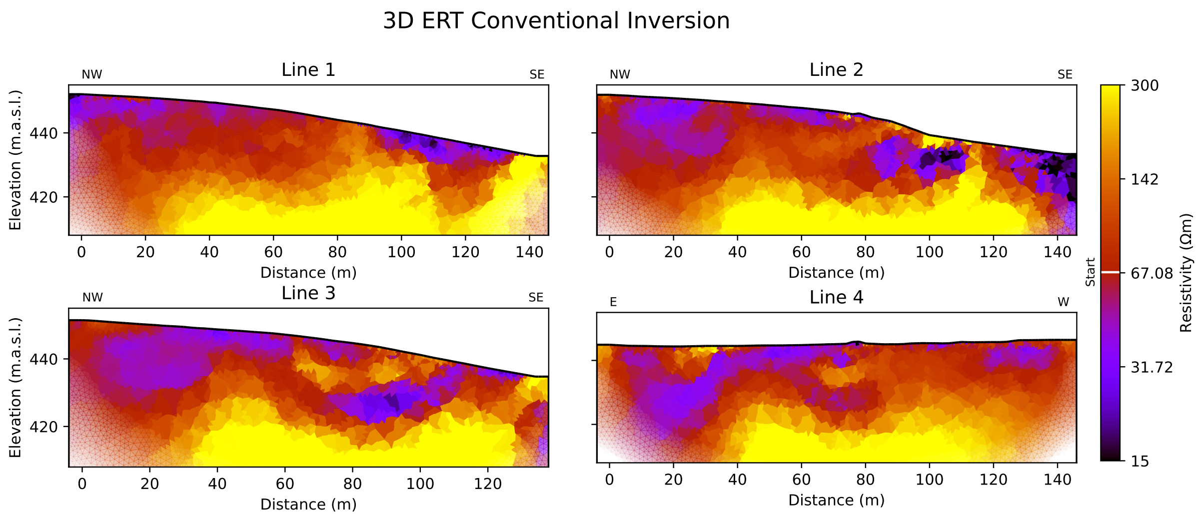

Figure 5.6: 3D ERT inversion result with a conventional first-order smoothness constraint. Shown are the cross-sections along the 4 ERT profiles. The misfit χ^2 is around 6. The value of the homogeneous starting model is indicated by the white line on the colorbar.

5.3.3 Minimum entropy inversions

Before a joint inversion is performed, standalone ME inversions of the 3D ERT and magnetic data set are performed. This enables the investigation of the influence of the order q, the regularization λ and the smoothing factor a better, since computational requirements are reduced in comparison to the joint inversion. The ERT inversion parameters are guided by the synthetic data study which already used the ERT method (Chapter 4 (Synthetic study)), however, it is important to note that λ is mesh dependent and therefore the settings only provide a good starting point as they might differ to the 2D case. The magnetic method was not used yet such that several inversion runs had to be performed to get a suitable set of parameters. An important observation is that the ME magnetic

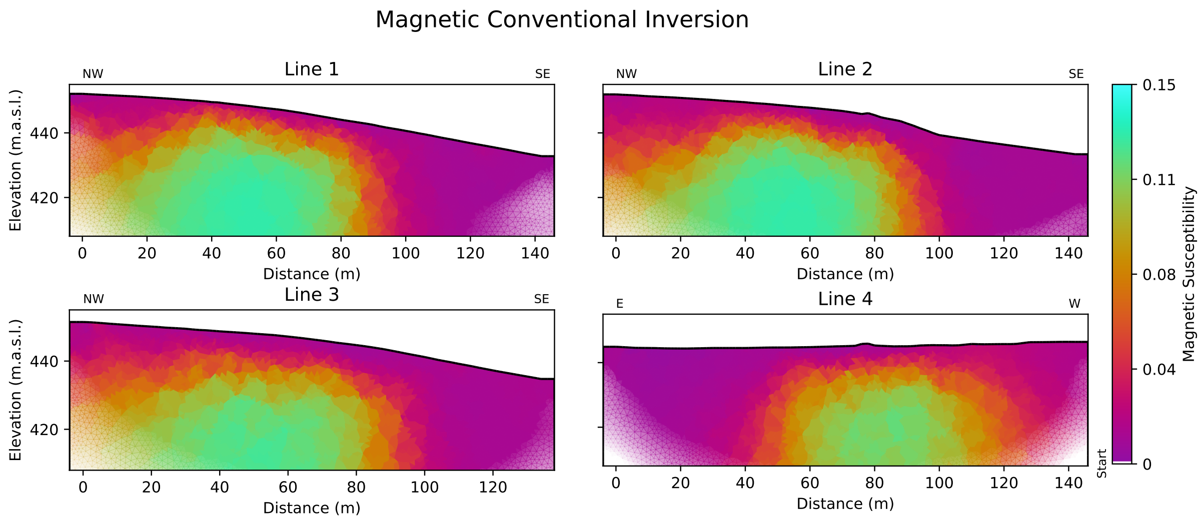

Figure 5.7: 3D magnetic inversion result with a conventional first-order smoothness constraint. Shown are the cross-sections along the 4 ERT profiles. The misfit χ^2 is around 1. The value of the homogeneous starting model is indicated by the white line on the colorbar.

inversion eventually ends up at a good misfit of $\chi^2 < 3$, however, it generally requires more iterations due to a slow convergence. Therefore, ME parameters should not only result in a good fit but also in a relatively fast convergence. The final ME magnetics settings produce reasonable susceptibility images with $\chi^2 < 2$ in less than 20 iterations.

The best ME results of the ERT and magnetic method are presented in Figure 5.8 and Figure 5.9, respectively. The first order results of the ERT inversion are very similar to the conventional inversion results (Figure 5.6) with slightly stronger resistivity contrasts at shallow depth due to the entropy constraint. Larger differences occur for the second-order results as the high-resistive feature at greater depth appears smaller and more present at the southern end of the slope. Furthermore, shallow resistivity changes are stronger in comparison with the first-order results. This is best illustrated in the profiles 2 and 3 between 80 and 120 m.

In contrast to the ERT method, the magnetic ME inversion results show considerable differences to the conventional first-order smoothing. The first-order ME results show a strong magnetic anomaly in the same region as the conventional results (Figure 5.7). However, while the conventional results are strongly smoothed out, the ME results present a very concise outline of the body with very little smoothing. The anomaly appears to be homogeneous with a susceptibility value of 0.15 in a non-magnetic host rock with a susceptibility close to 0 due to the sparsity constraints introduced by the entropy stabilizers. Furthermore, these susceptibility images are similar to the magnetic and gravimetric images provided by Zhdanov et al. (2022) and are therefore indicating a correct implementation of the method. It appears that the sparsity constraint is even stronger for the second-order ME inversions as the anomaly is more compact with even less smoothed out transitions between the anomaly and the background. The anomaly is solely present in the southwestern part of the conventional and first-order ME inversion anomaly.

These standalone ME inversion results suggest that the first-order ME is more suitable for data inversion as it does not lead to a collapsed magnetic anomaly. Furthermore, the first-order ME ERT results show not as drastic resistivity changes at shallow depth as well as a more continuous high-resistive feature. The latter is more in accordance with the geologic knowledge of the area as consolidated sandstones and a volcanic diatreme are expected (Eilhard, 2018).

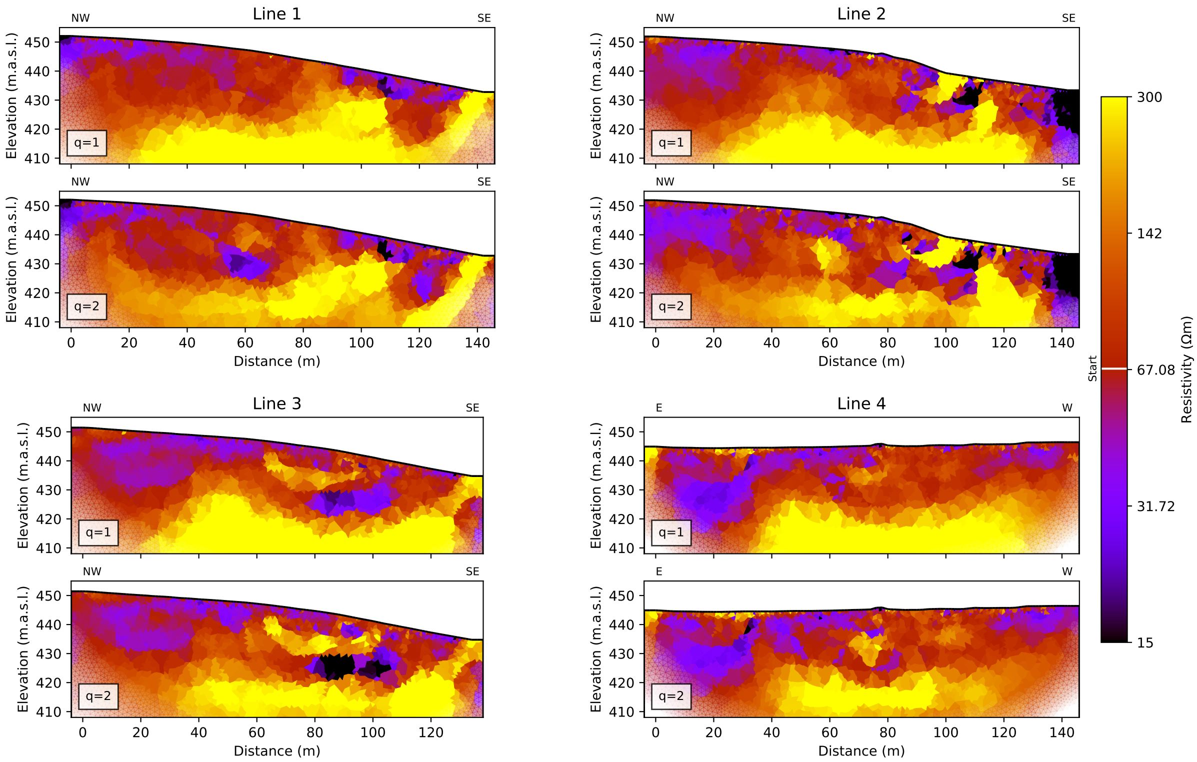

Figure 5.8: ERT ME inversion results. Shown are the first and second-order results for all 4 ERT profiles. The value of the homogeneous starting model is indicated by the white line on the colorbar. Following parameters are chosen: $\beta = 10^{-10}$, $\lambda_{\mathrm{ME1}} = 0.005$, $\lambda_{\mathrm{ME2}} = 0.01$, $a_{\mathrm{ME1}} = 35$, $a_{\mathrm{ME2}} = 20$.

5.3.4 Joint minimum entropy results

5.3.4.1 Method weighting tests

The standalone ME inversions provide suitable values of λ, q and a, however, they do not hold any information about the method weighting factors mw. Therefore, three different weighting scenarios of the JME inversion are considered in this section, namely an equally weighted scenario between ERT and magnetics as well as two one-sided weighting cases where one method has a hundred times stronger weighting. Figure 5.10 presents the resulting inverse models (5.10a, 5.10b) along with the corresponding misfit plots (5.10c). For each joint inversion the iteration with the lowest joint misfit ($\chi_{\mathrm{ERT}} + \chi_{\mathrm{MAG}}$) are selected for display. The equally weighted case is presented in the upper row while stronger weighting on the ERT method is presented in the middle row and stronger magnetic method weighting at the bottom. The Figures 5.10a and 5.10b indicate that a stronger weighting of the ERT method is changing the appearance of the susceptibility anomaly and improves the resistivity images as it appears smoother. If the magnetic method is weighted stronger, there is little to no change in

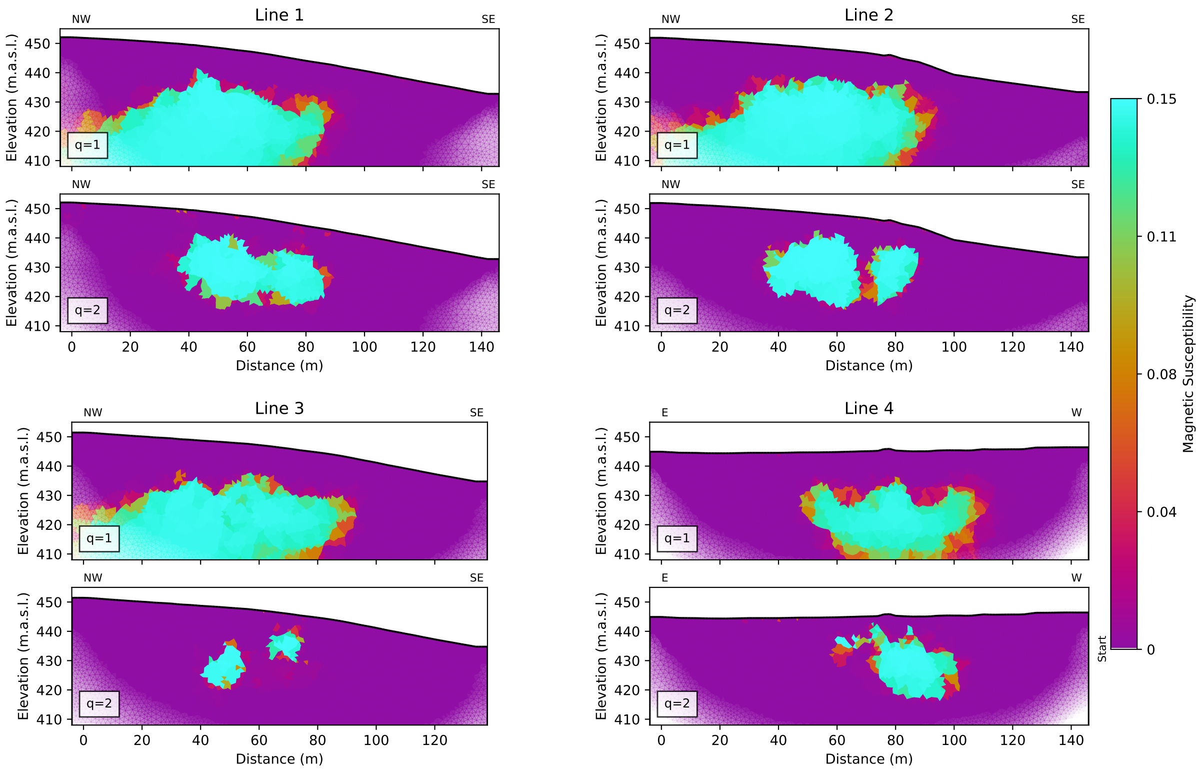

Figure 5.9: Magnetic ME inversion results. Shown are the first and second-order results for all 4 ERT profiles. The value of the homogeneous starting model is indicated by the white line on the colorbar. Following parameters are chosen: $\beta = 10^{-10}$, $\lambda_{\mathrm{ME1}} = 0.05$, $\lambda_{\mathrm{ME2}} = 0.01$, $a_{\mathrm{ME1}} = 50$, $a_{\mathrm{ME2}} = 60$.

the magnetic result in comparison to the equally weighted case, however, the resulting resistivity sections show clear deterioration as they appear quite noisy with many strong resistivity variations. For all three scenarios the ERT methods seems to converge much faster than the magnetic method, however, the latter eventually reaches lower χ^2 values. As seen, the improvement of the data fit of the magnetic method is strongly influenced by the method weighting factor, as a large *mw* on the magnetic method provides more freedom and flexibility to fit the data since the ERT structure has only little influence. Vice versa, for strong ERT weighting the inversion cannot produce as good data fits due to the strong structural constraint of the ERT method. Therefore, the method weighting factor does not only influence the exchange of structural information but ultimately can be used to improve convergence of a method.

Figure 5.10c also shows the value of the joint minimum entropy stabilizer S_{JME1} throughout the inversion in red. For the cases of $mw = [1, 1]$ and $mw = [1, 100]$, the stabilizer stays nearly constant at values close to 10 after few iterations. However, for stronger ERT weighting the stabilizer shows strong changes throughout the inversion. Towards the end of the inversion the algorithm seems to find a magnetic model that decreases the stabilizer which causes a spike in the magnetic data misfit. This could be an indication that there are structures in the ERT that simply cannot be explained by the magnetic observations. However, since the ERT method is less ambiguous and has more data observations than the magnetic method, a stronger weighting on the ERT method is considered. This will also ensure a better interpretability of the subsurface resistivity image. Figure 5.10 suggests to

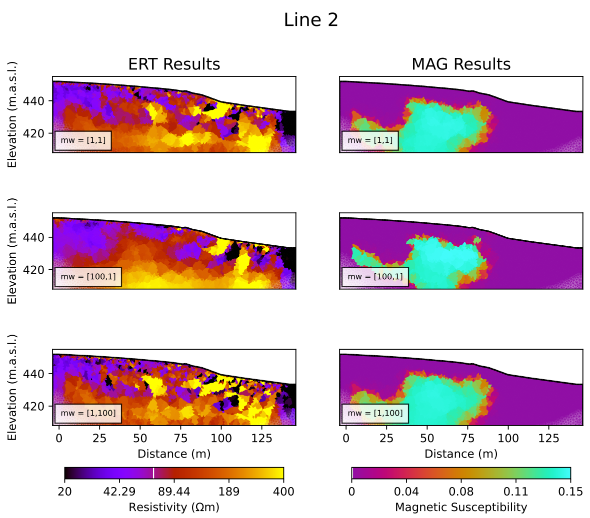

(a) 3D Model resistivity and susceptibility cross-section below line 2.

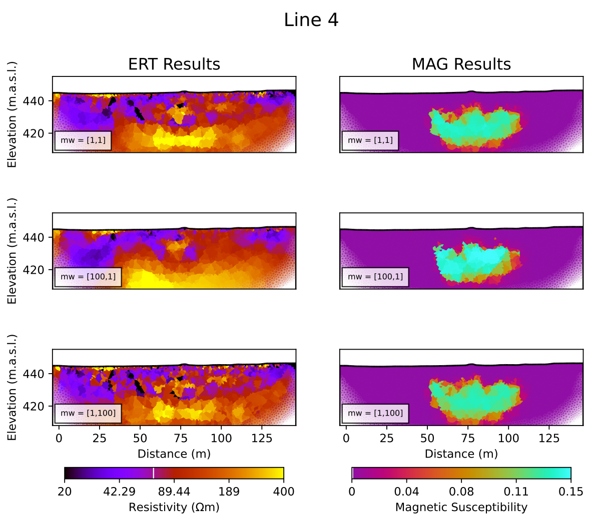

(b) 3D Model resistivity and susceptibility cross-section below line 4.

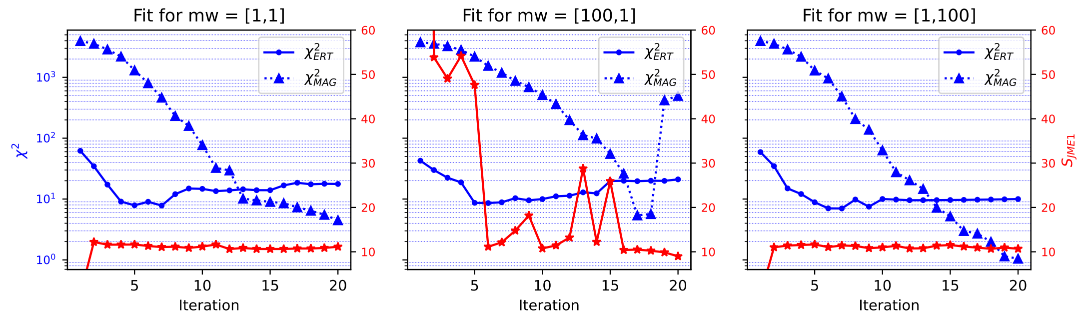

(c) Convergence plots of the data fit during the inversion. The red line is scaled by the right, red axis and demonstrates the value of the stabilizer S_{JME1} at each iteration.

Figure 5.10: First-order JME inversion results for different method weighting factors mw. The factors are presented in the format of $mw = [mw_{\mathrm{ERT}}, mw_{\mathrm{MAG}}]$. Considered are an equally weighted case as well as strong one-sided weighting. Shown are cross sections below the ERT lines 2 (a) and 4 (b) as well as the data fit during the inversion for all three scenarios.

choose a much weaker ERT weighting factor than 100 to ensure good data fit of the magnetic data as well as a good behavior of the entropy stabilizer.

5.3.4.2 Result comparison

Based on the observations made in the previous subsections, a joint minimum entropy inversion is performed with the first-order JME expression, $\lambda_{\mathrm{ERT}} = 0.005$, $\lambda_{\mathrm{MAG}} = 0.05$, $a_{\mathrm{ERT}} = 35$, $a_{\mathrm{MAG}} = 50$, $mw_{\mathrm{ERT}} = 10$, $mw_{\mathrm{MAG}} = 1$ and $\beta = 10^{-10}$. Comparisons of the joint inversion results with the conventional results (Figures 5.6 and 5.7) and first-order ME results (Figures 5.8 and 5.9) are presented in Figures 5.11 to 5.14. It can be observed that the JME results show clear differences to the conventional smoothness-constrained inversion and the standalone ME results. The magnetic anomaly shows a clear change in shape and susceptibility contrast with respect to the ME results. In lines 1 to 3 the match between the two different methods is much better in the northwestern part than towards the southern end of the slope. The high resistive feature appears diminished inside the magnetic anomaly and cut off from another high resistive feature on the southern end of the lines. In line 4 the relatively wide spread high-resistive feature at greater depth seems focused within the anomaly, making the images more similar. It is important to mention that the magnetic anomaly appears less homogeneous which probably is connected to the changed shape while providing good data fit. Furthermore, the ERT results show comparably strong resistivity variations inside the magnetic anomaly as resistivity increases towards greater depth. Overall, the results indicate a clear improvement towards structural similarity.

To illustrate the impact of the JME approach further, consider the model weights $\omega_{\mathrm{JME1_i}}$ of the last iteration of both methods as well as the contribution of every cell to the JME stabilizer $S_{\mathrm{JME1}}(\mathbf{r})$ (Figure 5.15). The black lines are corresponding to the magnetic anomaly as shown in Figures 5.11 to 5.14. The magnetic weights show the lowest weights exactly where the anomaly is located and the strongest weights around it. There appears a decrease in model weights with increasing distance from the anomaly meaning that in these regions there appears a model contrast that is supported by the JME constraint. This simply arises from magnetic susceptibilities two to three magnitudes lower than 10^{-4} (susceptibility of the reference model), which therefore represent a considerable contrast to the reference model due to the logarithmic transformation in the model normalization as shown in eq. 3.1. This means that the JME constraint pushes these model parameters closer to zero and therefore away from the reference model. In contrast to the magnetic model weights, the ERT weights appear more complex. Strong variations can be observed at shallow depth and outside the magnetic anomaly that originate from the resistivity variations in Figures 5.11 to 5.14. The upper and southern parts of the anomaly also show weight variation due to resistivity changes. However, the bottom part of the anomaly which appears with high resistivities in the inversion results, shows low weights as it is to be expected based on the intuition of the approach. According to eq. 2.40, both method specific model weights together with the respective inverse models can be used to calculate the contributions of each cell towards the JME stabilizer (Figure 5.15 right). It becomes clear that the region of the anomaly has the strongest contribution to the joint entropy and therefore confirms that the JME stabilizer actually promotes a shared subsurface structure during the inversion.

Figure 5.16 presents the different data misfits for the different inversion results. First, consider the ERT misfit pseudosections. There is a clear deterioration in the data fit going from separate 2D inversions to the 3D inversions as there are less degrees of freedom. In all 3D ERT inversions, most of the higher misfits are located at low levels in line 2 which is probably related to the strong apparent resistivity contrast to the neighbouring lines 1 and 3 (see Figure 5.4). Furthermore, slight improvements can be observed going from conventional 3D inversion to standalone ME ERT inversion. The JME ERT misfit appears to be improved, however, the corresponding χ^2 indicates a worse data fit. Reason for that is that the outliers at low levels might have higher misfit percentages and therefore have a strong negative influence on χ^2 while the remaining misfit shows slight improvements. Another factor that influences the fit is the joint structural constraint which might counteract with the data fitting as the ERT method might sense hydrological changes that are not sensed by the magnetic method and therefore are not included in the JME structural coupling. In comparison to that, the magnetic data misfit shows great improvement from conventional to ME inversion. This might be related to the sharp anomaly edges that are produced in the ME inversion (see Figure 5.9) as it

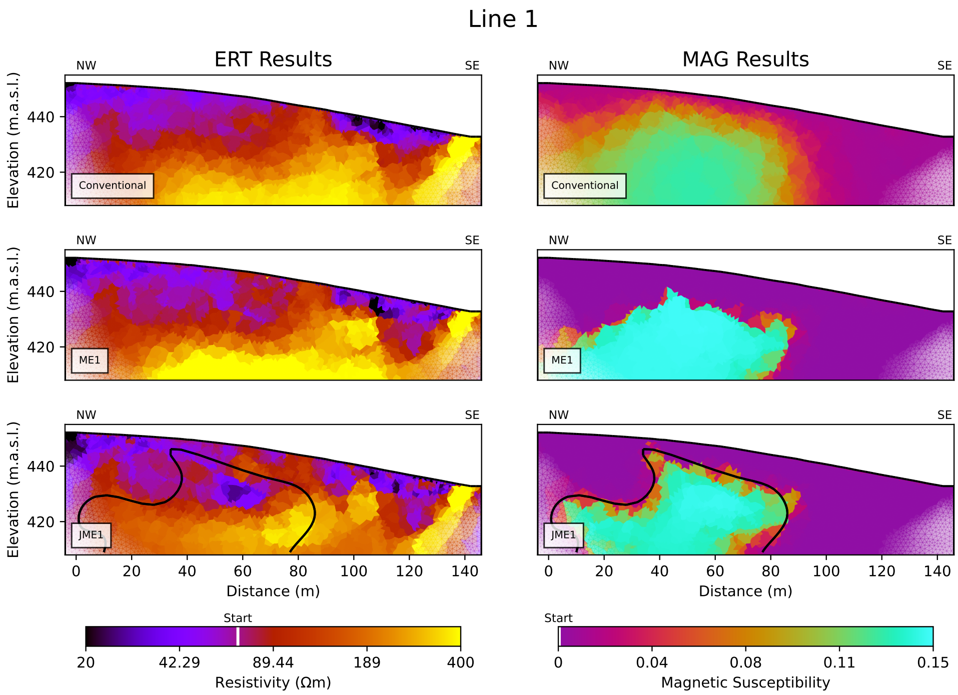

Figure 5.11: Comparison of conventional, ME standalone and JME inversion results underneath ERT line 1 (see Figure 5.1b). The black lines outline the magnetic anomaly to better illustrate shared structures.

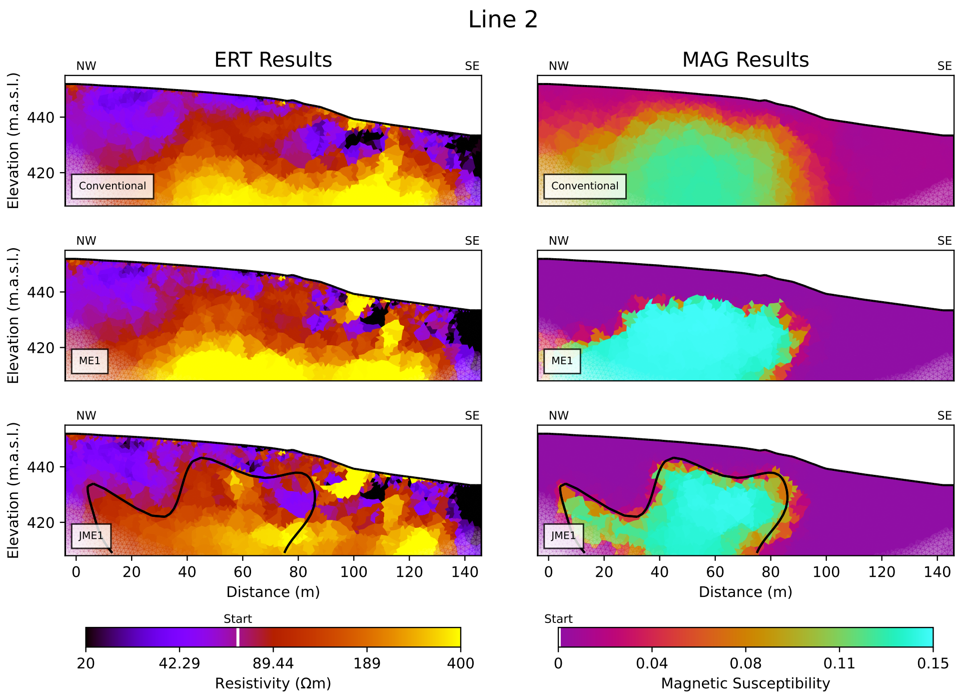

Figure 5.12: Comparison of conventional, ME standalone and JME inversion results underneath ERT line 2 (see Figure 5.1b). The black lines outline the magnetic anomaly to better illustrate shared structures.

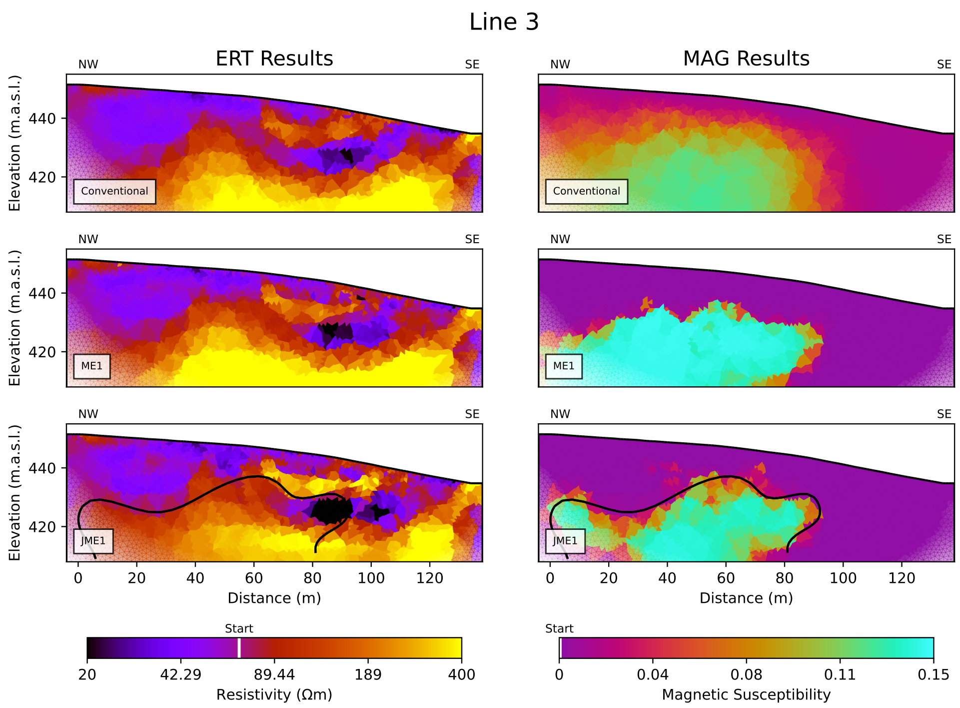

Figure 5.13: Comparison of conventional, ME standalone and JME inversion results underneath ERT line 3 (see Figure 5.1b). The black lines outline the magnetic anomaly to better illustrate shared structures.

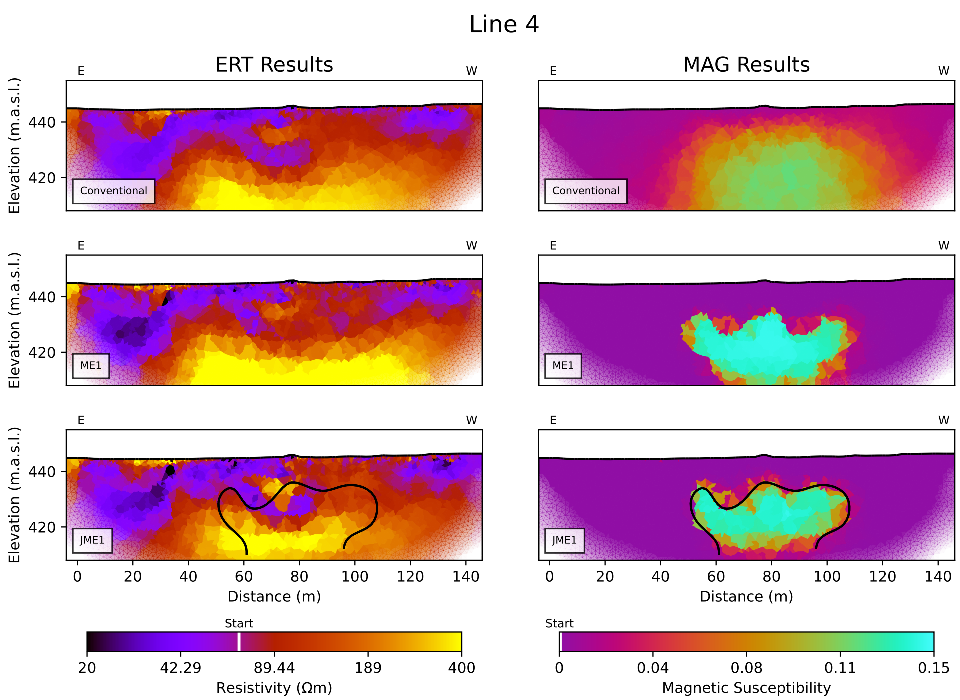

Figure 5.14: Comparison of conventional, ME standalone and JME inversion results underneath ERT line 4 (see Figure 5.1b). The black lines outline the magnetic anomaly to better illustrate shared structures.

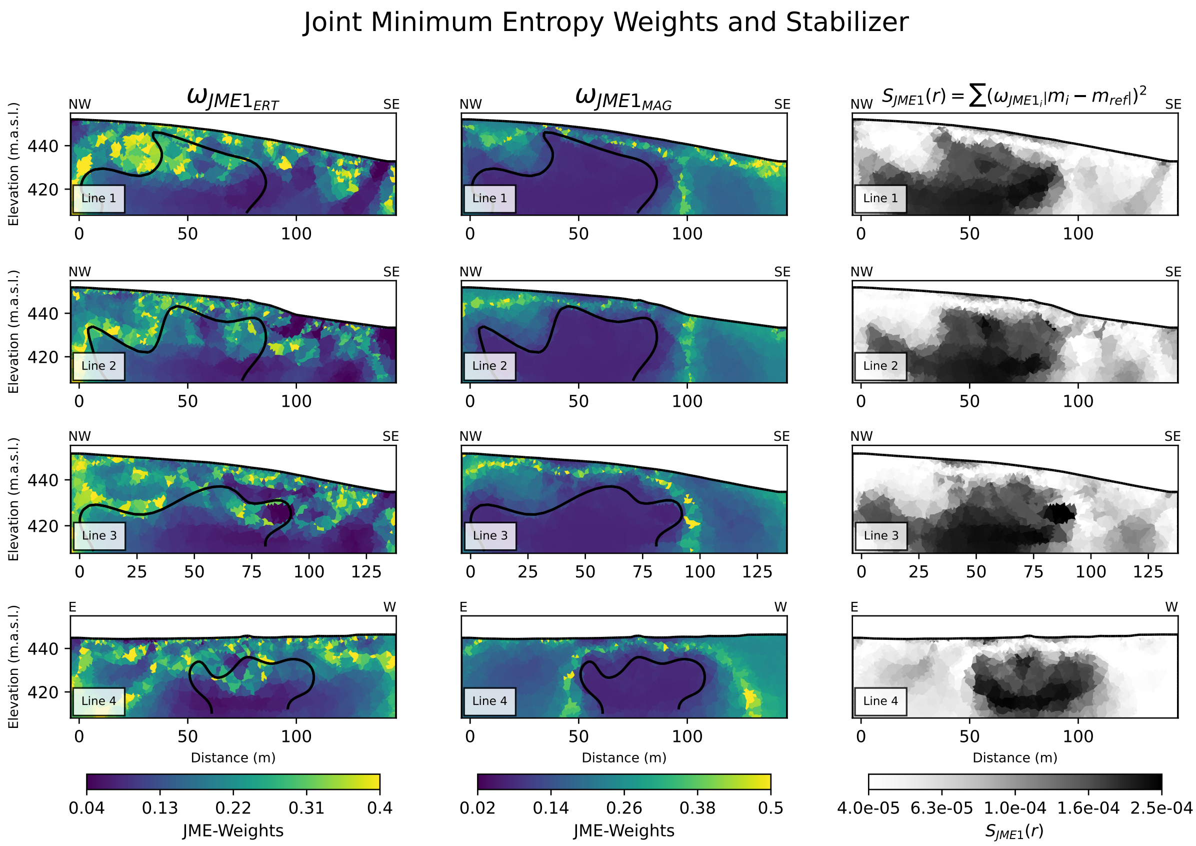

Figure 5.15: JME weights of ERT (left) and magnetic method (middle) based on JME inversion results of Figures 5.11 to 5.14. The right column shows the contribution of each model cell to the JME stabilizer (eq. 2.40). The black lines outline the magnetic anomaly to better illustrate shared structures in the model weights and the JME stabilizer.

is more realistic than very smooth susceptibility distributions in the subsurface and therefore could explain the data more accurate. However, the conventional inversion eventually ends up at similar misfits after more iterations as it is converging very slow. This suggests that the difference might also be introduced by the choice of the convergence criterion in the conventional inversion. Similar to the ERT misfit, the magnetic JME misfit shows a slightly elevated χ^2 which originates from the additional structural constraint. Overall, the magnetic data is fitted better than the ERT data since the magnetic data has less observations and is more ambiguous.

5.3.5 Geologic interpretation

For the geologic interpretation of the inversion results consider the cross-sections presented in Figures 5.11 to 5.11 as well as the 3D visualization in Figures 5.17, A.2 and A.3. They show a strong magnetic anomaly of magnetic susceptibilities of above 0.1 which exceed the common range of sedimentary rocks and therefore indicate the suspected volcanic diatreme structure. The surrounding host rock has susceptibilities below 10^{-4} which is in accordance with the common range of sandstones (see Figure 2.3). The diatreme appears to be located more towards the northwestern part of the study area at a depth between 10 and 20 m below the surface. The upper part is very irregular and wider than the root of the diatreme at greater depth, making the anomaly look like an irregular,

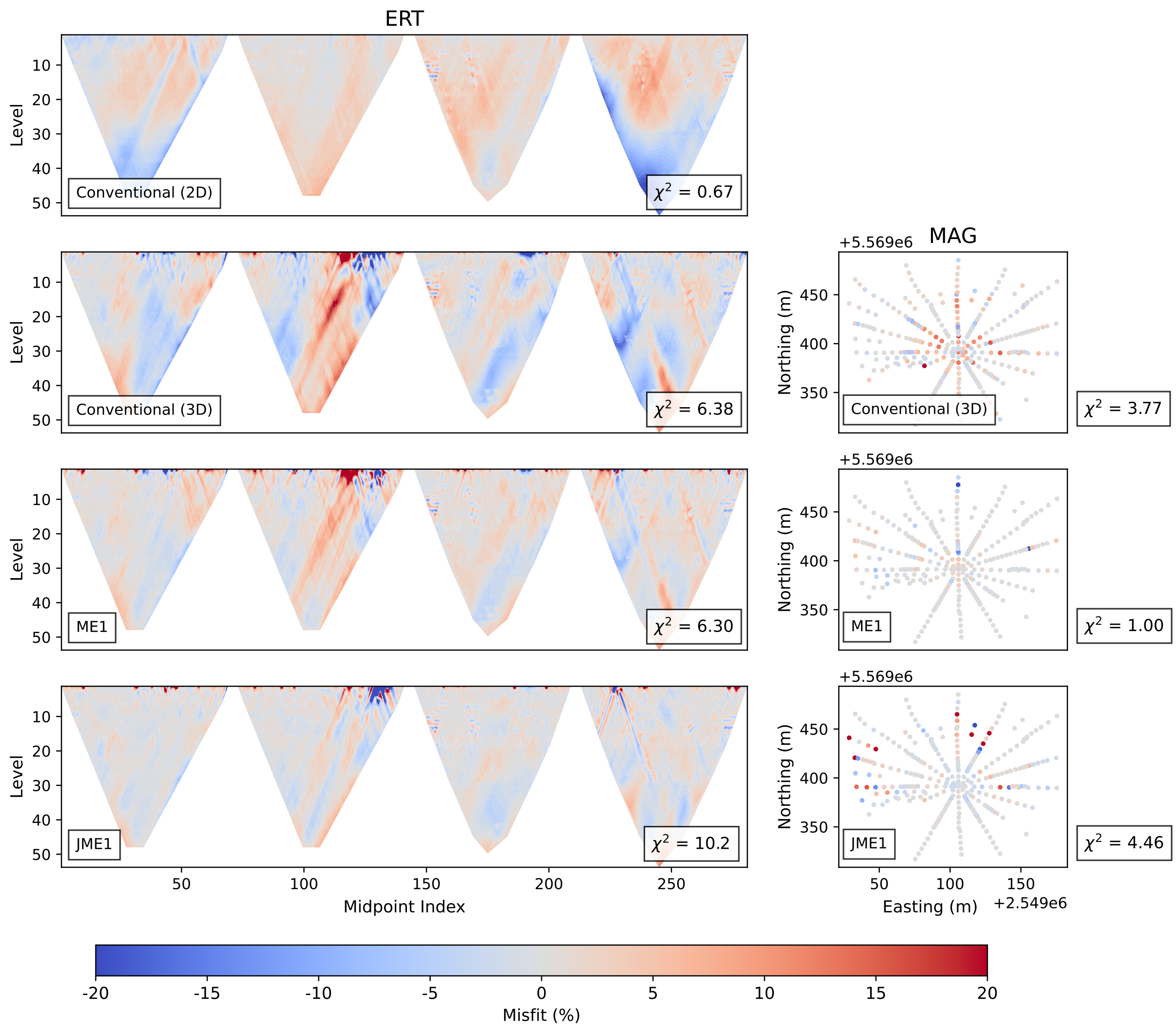

Figure 5.16: Comparison of the data misfit of 2D ERT Inversions and 3D conventional, standalone ME and JME inversion with Magnetic data fit.

up-side-down cone. This is in accordance of the expected shape of the volcanic structure as during the eruption a small crater was built that partly filled with the erupted material (Schmincke, 2009; White and Ross, 2011). It is important to mention that the appearance of the magnetic anomaly still holds considerable uncertainties due to the underlying choices of the parameter range as well as the depth extent of the model domain. However, the JME inversion results of the ERT data can confirm parts of the magnetic anomaly suggesting that the results are reasonable and interpretable. In the northwestern part of the diatreme there is a good match between the multi-physical images. The resistivity image suggests that the diatreme structure has electrical resistivities of below 100 Ωm in the shallow regions that are increasing towards 400 Ωm at the bottom of the model. This suggests that the upper part of the diatreme has a higher porosity or permeability which increases the electrical conduction through the water-filled pore space (Kearey et al., 2002). In context of the diatreme this could also be explained by erupted material falling back into the crater structure and by less compaction due to less overburden. Above the diatreme, resistivities below 50 Ωm indicate soil as well as loose and wet sediments, which is also in accordance with the interpretation of the host rock of the magnetic anomaly and the observations in the field.

The shallow, southern part of the magnetic anomaly is not matching the ERT results as good as the northwestern part. While the magnetic data inversion indicates a clear boundary of the diatreme, the ERT result shows strong variations. Towards greater depth the two images appear more similar again as the high resistive feature matches the magnetic anomaly. The most obvious explanation for this discrepancy are hydrologic conditions as the ERT method is sensitive to changes of the water-filled pore space in the subsurface. It is possible that the rain prior to the field campaign created water accumulations in certain regions which produce conductive regions in the subsurface. In contrast to that the magnetic method is solely sensitive to the rock content as the rock matrix is the only part in the subsurface that holds a significant magnetization. It can therefore be assumed, that the shallow sandstone holds significant heterogeneities that strongly influence the hydrologic conditions. Further resistivity variations might be introduced by the soil layer as the sun on the south-facing slope partially dried the upper soil. In conclusion, both results indicate a potential volcanic diatreme structure, that is most likely be the missing eruptive source of the found sanidine crystals and volcanic tuffs. To fully confirm the findings, drillings or excavations need to be considered.

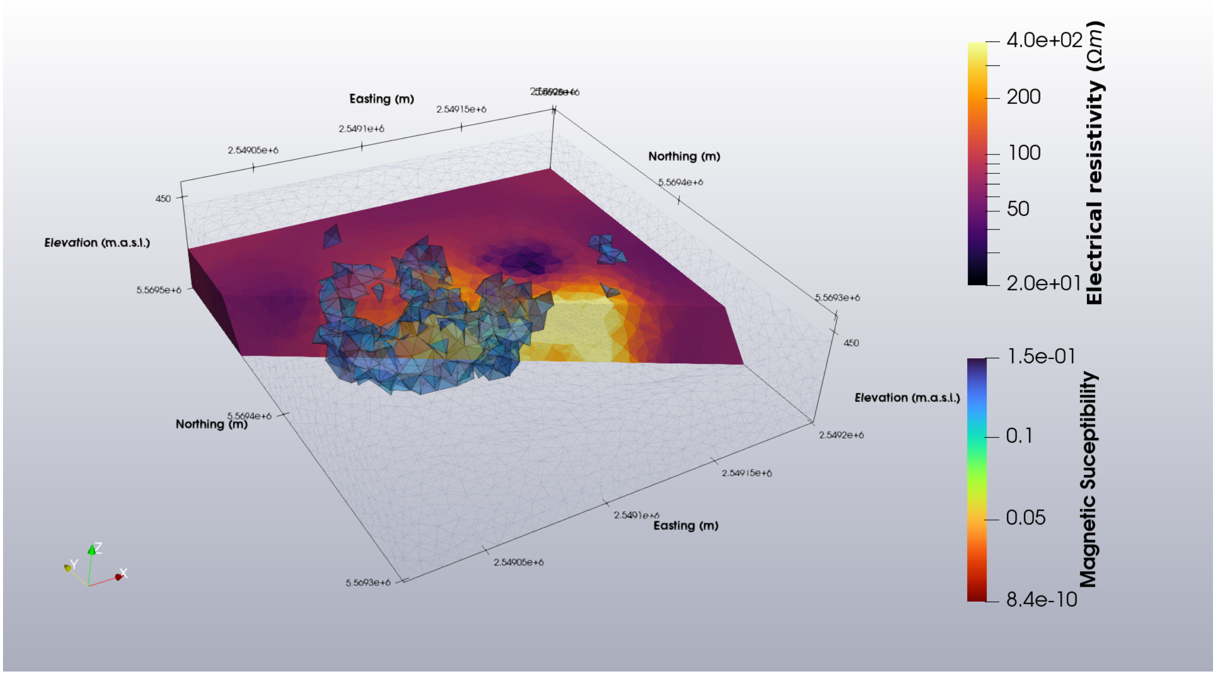

Figure 5.17: 3D Visualization of 3D JME ERT inversion and 3D JME magnetics inversion. The magnetic anomaly is shown as the blue partially transparent volume. The 3D electrical resistivity volume is sliced diagonally and at an elevation of 425 m.a.s.l. using ParaView (Ahrens et al., 2005).

5.3.6 Comparison to previous studies

This study does not only aim on the application of the JME inversion approach but also on the confirmation of the magnetic model created by Boxberg (2011), which assumes a cylindrical anomaly with a susceptibility of 0.1. As seen in Figures 5.11 to 5.14 as well as in Figures 5.17, A.2 and A.3, the existence of the diatreme could be confirmed, however, they indicate that the structure is more complex than a simple cylinder or a cone. To provide a full comparison to the volcanic diatreme models, consider the screenshots of 3D visualizations in Figure 5.18. The magnetic model of Boxberg

(2011) is presented in green alongside the region of the magnetic anomaly that has a susceptibility of $\kappa \geq 0.1$ (grey). Both models are present in the same region, however, the results of this work indicate a shift of 5 to 10 m towards southwest with respect to the the previous model. The lateral extents of both models are in accordance with each other. Furthermore, the previous model extends to an elevation of 380 m.a.s.l. which is approximately 25 m deeper than the model domain chosen for the 3D inversions in this chapter. As mentioned previously, that could have an influence on the appearance of the anomaly. The depth of the model domain could not be increased as it was chosen to fit the ERT data. A joint inversion beyond the sensitivity of one method does not hold reliable information, which made it not feasible to extend the depth of the 3D mesh. The old magnetic model shows a strong indent at the upper, northeastern part of the cylinder which seems to be partly present in the 3D JME magnetic results as well (Figure 5.18c). However, the old magnetic model assumes a flat top boundary of the diatreme, which seems to be a too strong simplification.

The updated location of the diatreme also coincides with a low-velocity structure that is observed in the 3D SRT inversion result at a depth of approximately 20 m. The relatively low velocity with respect to the surrounding rock was interpreted as an indication for brittle or fractured material that fell back into the crater after the eruption. This is also in accordance with the interpretation of the ERT inversion results and therefore further confirms the findings of this chapter.

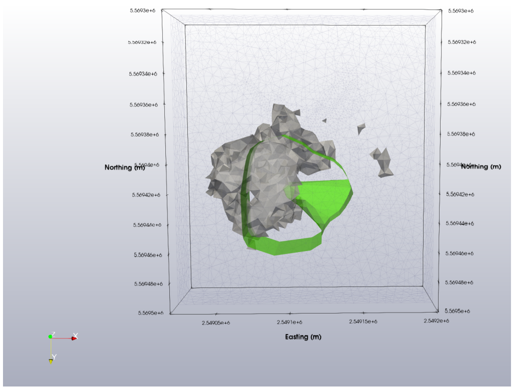

(a) View up.

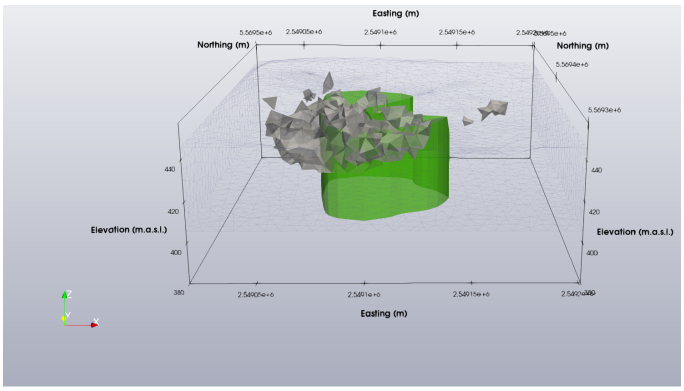

(b) View towards North.

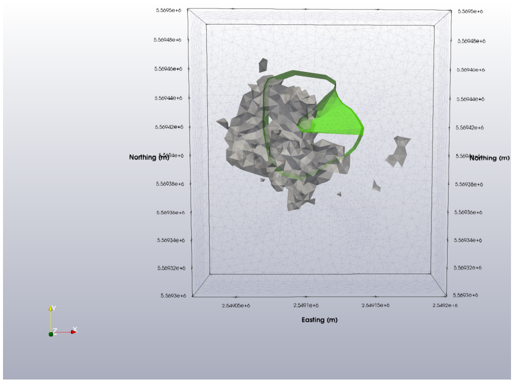

(c) View down.

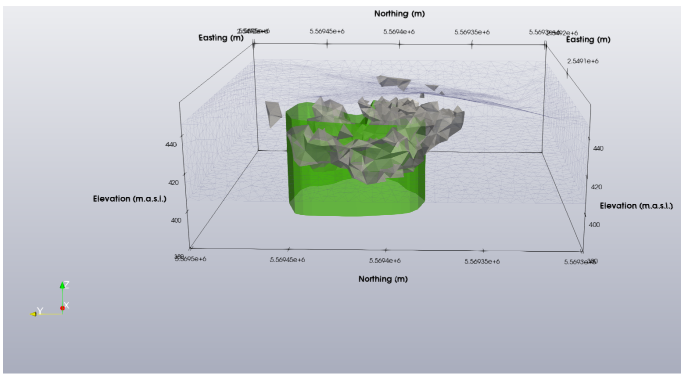

(d) View East.

Figure 5.18: 3D visualizations of the old magnetic model of Boxberg (2011) alongside the magnetic JME inversion result.

6

Discussion

Contents

This chapter presents the discussion of the implementation of the JME-constrained SCCI approach that was applied to synthetic and field data in the previous chapters. The main elements of the discussion are concerning structural coupling, model sparsity, hyperparameters, reference models, and the (joint) minimum entropy gradient expression.

6.1 Structural coupling

In Chapter 4 (Synthetic study) and Chapter 5 (Field study: Rockeskyller Kopf) the joint minimum entropy constrained SCCI approach is successfully applied. In the synthetic data study, small improvements in the imaging of the seismic anomalies could be observed due to the JME inversion (Figure 4.12). The structural similarity is enhanced when considering the case of stronger method weighting on the ERT method as the left anomaly appears stronger at the top part than at the bottom in both models. Improvements towards more consistent structures are also observed in Figures 5.11 to 5.14 as the magnetic susceptibility anomaly clearly develops shared boundaries with the electrical resistivity distribution. An important observation is that there is no indication for the enforcement of features that are only present in one method. This can be seen best in Figure 4.12 as the high velocity bottom layer that is present in the SRT result does not seem to introduce any structure in the resistivity distribution. Similarly, the resistivity variations observed in the southern part of the study area at Rockeskyller Kopf do not introduce susceptibility variations in the magnetic inversion result. Furthermore, the resistivity gradient that is present within the region of the magnetic anomaly does not produce a gradient in the magnetic result and therefore illustrates that the structural coupling between the methods is flexible. This is a behavior that is highly desired as it prevents the introduction of strong inversion artefacts of one method into another. It was also observed by Zhdanov et al. (2022) when the method was presented for the first time and once again confirms a correct implementation.

In this work, no fair comparison to other common structurally-coupled joint inversion approaches is performed, however, the results presented in the previous chapters and studies of other structural coupling approaches allow a qualitative comparison. In section 2.3, the cross-gradient approach was shortly introduced (see eq. 2.24). The results of Gallardo and Meju (2004), Gallardo et al. (2005) and Gallardo (2007) suggest that the cross-gradient method presents a stronger structural coupling between methods as resulting models appear to be more structurally similar to each other. Possible reasons for this could be that the method uses model gradients in comparison to the JME approach, which utilizes model contrasts. Furthermore, it is a proper joint inversion meaning that during the inversion a joint objective is minimized that consists of all data misfit functionals $\phi_{\mathrm{d}}^{(i)}$ as well as all model misfit functionals $\phi_{\mathrm{m}}^{(i)}$ alongside the cross-gradient functional. The JME inversion approach is implemented in a cooperative scheme, which provides weaker coupling between the methods. However, it is easier to implement as different inversion frameworks are running in parallel and only certain parameters need to be recalculated after each iteration based on a shared objective (Skibbe et al., 2021; Zhdanov et al., 2022).

The SCCI approach used by Skibbe et al. (2021) uses the model roughness calculated through a first-order finite-difference operator (eq. 2.21) to change the weighting of the smoothness constraint on the internal boundaries. In contrast, the JME approach is acting on the weighting of the individual model cells, which changes the applied damping. Both methods are able to produce similar structures in multi-physical images, however, due to the damping nature of the JME approach, results might be prone to outliers resulting in noisier images. This can be counteracted by increasing the smoothing factor, but this will ultimately lead to smoothed out edges. As the SCCI approach by Skibbe et al. (2021) is solely based on smoothing and decoupling of model cells, it can produce clean images without strong outliers while producing sharp edges. It is important to mention that these are just qualitative observations based on final inversion results. For a proper comparison, the different approaches should be applied on the same data, which will shed light on the benefits and drawbacks of each approach under the consideration of computational demands.

6.2 Model sparsity

Figure 2.5 illustrates how the entropy is used to introduce sparsity in the model. The minimum entropy constraints within the JME inversion theoretically promotes sharper edges and stronger magnitudes of anomalies. The latter was confirmed in the synthetic data study as resistivity anomalies had increased resistivity contrasts with respect to the background resulting in more accurate value estimations (Figure 4.12). This increased contrast of anomalies appears to be even stronger for the second order entropy expressions (see Figure 4.13). Similar observations are made in the field data study (see Figures 5.8, 5.9). However, the field data study as well as SRT ME inversion results reveal that these sparsity constraints might be too strong as anomalies appear collapsed and with unreasonable values. The latter is illustrated for example in Figure 5.13 as a low resistivity region develops increasingly lower values from conventional over ME towards JME inversion. An electrical resistivity below 10 Ωm is quite unlikely to be found in the study area based on the geologic understanding of the region and therefore a limitation of the parameter range could be considered to avoid the occurrence of such anomalous values. In pyGIMLi, this was a mandatory input for the magnetic data inversion and can be considered for other inversion frameworks as well, but it should be noted that these limitations are subjective choices and should therefore be chosen carefully with transparent reasoning.

The development of sharper edges is the second aspect of the sparsity constraint. It is nicely illustrated in the field data study as the standalone ME magnetics inversion shows massive improvements with respect to the conventional inversion, similar to the results shown by Zhdanov et al. (2022). However, it can be observed that the ERT and SRT JME inversion results do not have as sharp edges around anomalies. This might be related to the required smoothing of these methods that is necessary to produce clearer images with less outliers. Another explanation could be that this implementation of the approach is more suitable and more powerful for potential field methods. It is possible that the performance of the sparsity constraint can be improved by including sensitivities in the normalization of the model parameters similar to the implementation of Zhdanov et al. (2022) who use the integrated sensitivity to create dimensionless model parameters. Some first tests showed no significant gain when including sensitivities, but there is a multitude of choices for more sophisticated normalization approaches which could not be tested and implemented within the frame of this project.

It is important to mention that the entropy constraints can also be applied to standalone (i.e. single method) inversions, which might enhance subsurface imaging with respect to conventional smoothness constraints as indicated in chapters 4 and 5 (see Figures 4.12, 5.9). This indicates that the approach is not only beneficial for multi-method inversions, but also provides a useful tool for single method geophysical imaging.

6.3 Hyperparameters

The parameter tests in Chapter 4 (Synthetic study) illustrate how significant the influence of the governing parameters are on the resulting images. As mentioned during the field data study, they also have a considerable influence on the convergence of the inversion (see Figure 5.10) and therefore parameter tests are essential for the success of the JME approach. To speed up and simplify this process, it is suggested to start the search for suitable settings during ME standalone inversions as it is demonstrated in the previous chapters. Unfortunately, parameters have to be found by trial and error since no criterion or rule could be observed during this study. Therefore, it is recommended to perform grid searches for certain parameters, namely the regularization parameter λ, smoothing factor a, order q, and method weighting factor mw, similarly as it was done in this thesis. Note that mw can only be tested in the joint inversion and should therefore be investigated last.

Based on the results of this work, some dare rule of thumbs can be established that could help finding suitable parameters. However, it is important to mention that parameters of one method might need to be adjusted slightly for different applications, as it was shown for the ERT method in the previous two chapters. The numerical stabilizer β has no significant influence on the results as long as it is chosen much smaller than the normalized model parameters. The default of 10^{-10} can be transferred to future studies as normalized physical parameters are generally higher. The regularization parameters appears to be strictly below 1 to ensure sufficient data fitting while a smoothing factor of at least 10 is beneficial to prevent that weaker outliers are supported by the ME or JME constraints. As seen in Figures 4.4 to 4.11, both parameters are related to each other as a higher λ increases the smoothing along with the entropy constraint. Based on this study, the SRT method appears to prefer a higher λ and stronger smoothing with respect to the ERT method. This can be explained by the collapse of high velocity regions to ray paths-like structures that need to be smoothed out. This becomes more obvious when considering the second-order expression as it represents a stronger constraint on the entropy (see Figures 4.9, 4.15a). The magnetic method converges comparably slow in the field data study in comparison to the ERT method and therefore parameters are chosen to ensure relatively fast convergence. However, this could only be achieved by manual testing and is likely to be different for different data sets. The order is mainly influencing the sparsity of the model and was already discussed in the previous section. The results of this thesis suggest that a first-order expression should be generally considered for the JME inversion. Only if the ME standalone inversions of all methods indicate clear improvements with respect to the first-order results, the second-order expression should be considered for the joint inversion. Keep in mind that the sparsity constraint might be additionally enhanced during the joint inversion as shown in the ERT JME results. This thesis suggests that a method weighting factor $mw \ll 100$ should be chosen to ensure good convergence of all methods. It is best practice to make a fair comparison between the three weighting cases similar to Figure 5.10 as it ensures transparency in choice of this inherently subjective parameter.

6.4 Reference models

While clear improvements towards structural similarity are observed in the field data study, there are only minor improvements in the joint ERT and SRT inversion. This discrepancy is most likely influenced by the methods itself as discussed prior in this chapter. However, the reference models also have a considerable influence on the success of the JME approach. In this work the reference models are equal to the starting models, which is an intuitive and reasonable choice. As a consequence, a gradient reference model for the SRT method and a homogeneous reference model for the ERT method are obtained. As seen in the mathematical formulations of subsection 2.3.2, the JME inversion defines model contrasts in the same region as structural similarity. Therefore, the reference models of each method need to be chosen such that all methods develop anomalies in the same region. In case of the synthetic data study in this work the ERT method develops clear contrasts to the homogeneous background in the location of the anomalies as shown in Figure 6.1. However, the SRT method appears to have weak contrasts in certain regions of each anomaly and strong contrasts outside both anomalies. This occurs as the velocity of the first layer is much smaller than the gradient model in that region, while the gradient model has similar values to the anomalies at their respective positions (see Figures 4.1, 4.3, 6.1a). Thus, the JME stabilizer interprets the region outside the actual velocity anomalies as well as the bottom part of the circle anomaly and the upper part of the square anomaly as an anomaly with respect to the gradient reference model. As a consequence, ERT and SRT contrasts are not in similar regions, which could explain the minor improvements of the imaging of the anomalies (see Figure 4.12). This theory is confirmed by the splitting of the left anomaly in two zones in the ERT results as the upper part is an anomaly in both methods while the bottom is only interpreted as a model contrast in the ERT method.

This indicates that the method is working best if the starting and hence the reference model is representing the background of anomalous structures in the subsurface sufficiently good. It is possible that improvements of the joint ERT and SRT inversion can be achieved by adjusting the seismic reference model, for example with the correct two-layer background, which might be derived from standalone ME inversions. As seen in Figure 6.1b, this would produce ERT and SRT model contrasts in the same region, which is more beneficial for the JME inversion. This theory is confirmed when considering the JME inversion results with a new SRT starting model that approximately represents the correct two-layer background (see Figure 6.2). Due to the new starting model, the bottom layer has a slightly more concise left anomaly in comparison to the JME results of Figure 4.12 that is more similar to the ERT anomaly at the top, however, there is little to no improvement in the imaging of the right anomaly. This might be related to the applied method or to poor experimental design as the circle anomaly is also not imaged properly with a conventional inversion technique.

In theory it is possible to set a reference model that is not the starting model of the inversion instance, for example a gradient starting model with a homogeneous reference model (see Figure 3.4). However, this might introduce an initial bias as there are initial model contrasts present at the start of the inversion. A detailed reference model study is required to investigate the impact of the introduced bias in order to confirm this statement.

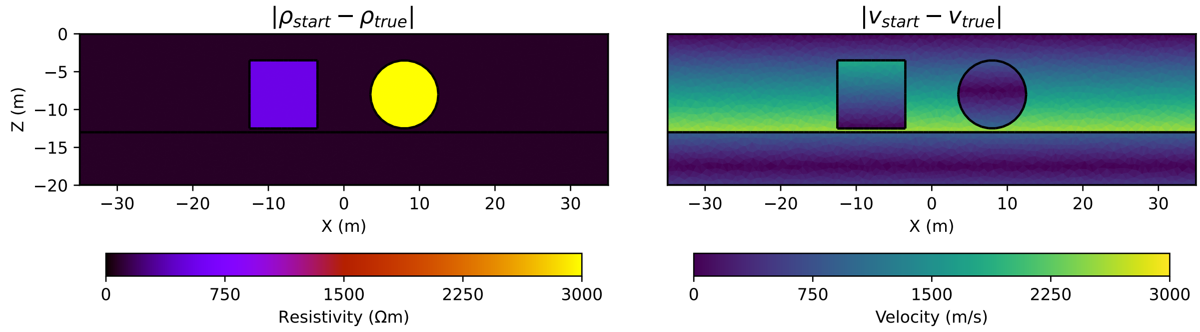

(a) Contrasts of true models (Figure 4.1) and the used starting models (Figure 4.3).

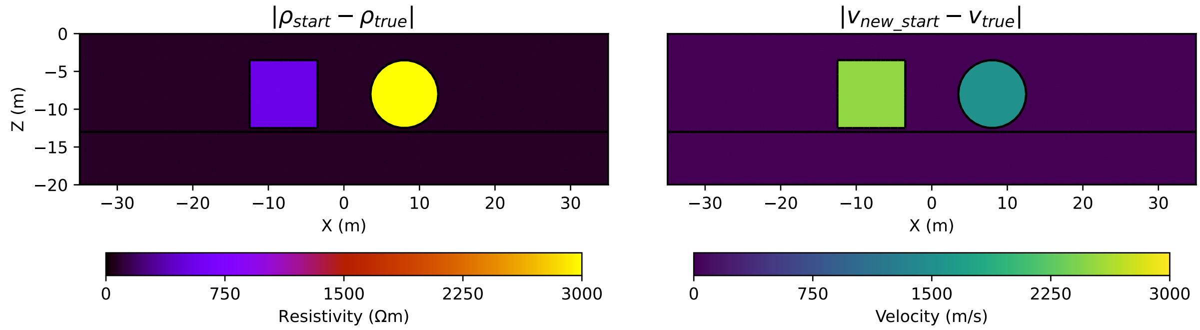

(b) Contrasts of true models (Figure 4.1) with the used ERT starting models (Figure 4.3) and an adjusted SRT starting model equal to the two-layer background of the true model.

Figure 6.1: Comparison of the model contrasts between true and starting models of the ERT and SRT method. The models are related to the synthetic data study as presented in Chapter 4 (Synthetic study). Note that the meshes of this figure are the mesh used for the synthetic data generation for illustrative purposes.

6.5 MEG and JMEG stabilizers

It was shown in Chapter 4 (Synthetic study) that the MEG and JMEG stabilizers do not perform as good as the ME and JME approaches. The exact reason for that is not clear, however, it can already be inferred from Figures 3.4 and 3.6b that there is no simple intuition behind the entropy gradient constraints in comparison to the ME and JME method. It is important to mention that the MEG formulation (eq. 2.33) and its extension (eq. 2.38) are introduced by Zhdanov et al. (2022) but not illustrated or applied to an inversion. Therefore, it is not clear if this approach is even applicable in its form or if it requires additional modifications. Due to the limited time of this research project, the latter could not be faced within this work.

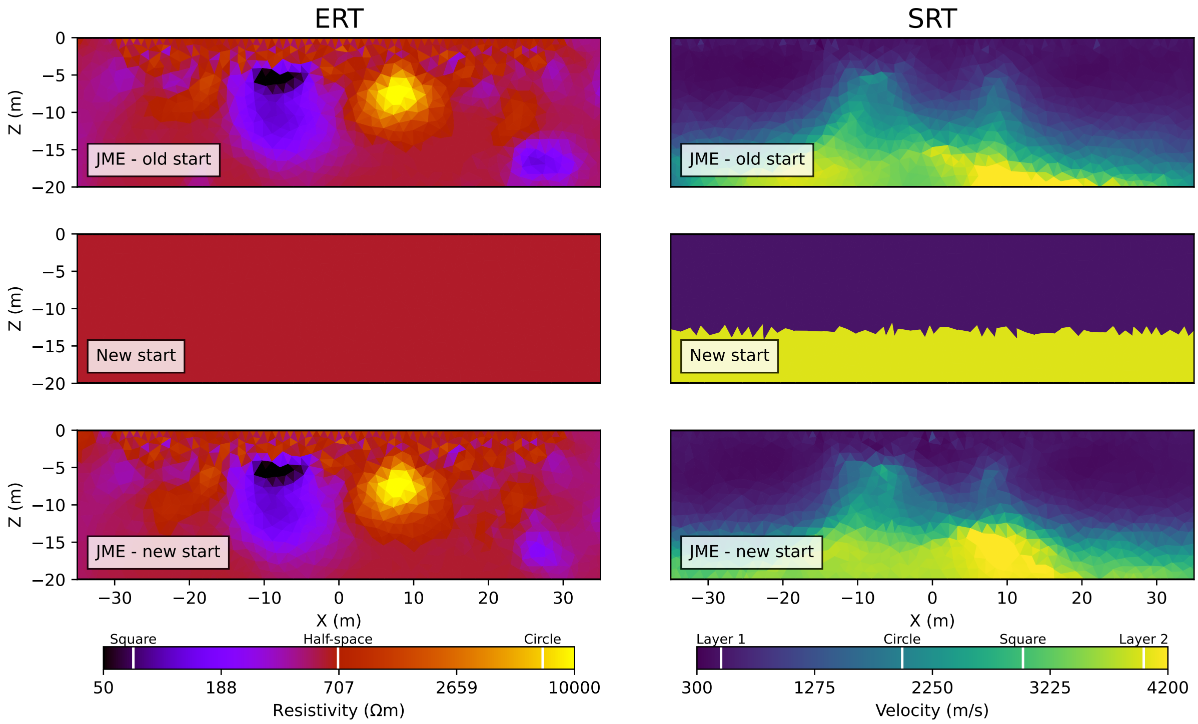

Figure 6.2: Comparison of the JME results of Figure 4.12 (top) and JME results with a new SRT starting model (bottom). In the middle the new starting models are shown. The ERT model stays the same but the SRT starting model represents an approximately correct background. Hyperparameters are same as in Figure 4.12 for equal weighting.

7
Conclusions and Outlook

Contents

This chapter summarizes the main findings of this thesis with respect to the initial research questions (see section 1.2). It will be rounded off with an outlook that suggests a list of possible objectives for further studies.

7.1 Conclusions

This thesis presents a successful implementation of the joint minimum entropy constrained SCCI (Zhdanov et al., 2022) and investigates its applicability on the ERT and SRT method. It also gives deeper insight in the functionality of the JME stabilizers and how hyperparameters affect the joint inversion and its results. The synthetic data study reveals that the approach can be applied to these geophysical methods, however, as described in Chapter 6 (Discussion) its success is strongly influenced by the chosen hyperparameters and reference models. Therefore, the search for suitable parameters is identified as the main challenge of the approach suggesting careful parameter tests to get a better control over the resulting models and the convergence of the inversion. Furthermore, this study is ruling out the MEG and JMEG stabilizers as useful inversion constraints in their original formulation provided by Zhdanov et al. (2022).

The new approach is not only applied to synthetic data but also to the magnetic and ERT data from Rockeskyller Kopf, Germany. As presented in Chapter 5 (Field study: Rockeskyller Kopf), the structural coupling of both methods with JME constraints improve the structural similarity between 3D magnetic susceptibility and electrical resistivity models and thus result in more consistent images. The results are used for an improved geologic interpretation of the diatreme structure as well as the surrounding host rock that is also in accordance with previously acquired data that is excluded in this work.

7.2 Outlook

The approach is relatively new, which already suggests additional research to explore and improve the method. The following are some ideas for future study objectives or adjustments in the implementation.

The method will benefit from more applications in synthetic and field data studies. It might be interesting to consider joint ERT and SRT studies in a cross-hole setting as the seismic starting model is generally speaking a homogeneous model, which might lead to improvements as the ERT and SRT starting and therefore reference models are more similar (see Figure 6.1b). This could be extended to a detailed reference model study that not only investigates the performance of the approach on changing reference models that equal the starting model, but also the effects of differing starting and reference models. Furthermore, since the JME inversion and its implementation provides a simple extension to numerous geophysical methods, a multi-method imaging study with three or even four methods is also of great interest. If possible, the Rockeskyller Kopf field data set could be considered as a suitable candidate as an additional 3D SRT data set is available that could be used alongside the 3D magnetic and ERT data of Chapter 5 (Field study: Rockeskyller Kopf).

In the research area of structurally-coupled joint inversion several approaches were developed in recent years, however, most publications solely focus on single methods (Gallardo and Meju, 2004; Gallardo et al., 2005; Günther and Rücker, 2006; Gallardo, 2007; Skibbe et al., 2021; Zhdanov et al., 2022) or a broad overview of different approaches (Moorkamp et al., 2016; Wagner and Uhlemann, 2021). Thus, future studies of the JME inversion should also consider a fair comparison to the well known cross-gradient approach as well as other SCCI approaches like Skibbe et al. (2021) which will reveal benefits and drawbacks of the joint minimum entropy constraints with respect to more established approaches and therefore will be decisive for a wide adoption of the approach.

It is important to mention that the implementation provided in this work is only a start. I believe that there are still conceptual improvements to make in different steps of the implementation. Especially, the normalization of model parameters in the weight calculation is chosen quite pragmatically with a simple linear min-max normalization (see Listing 3.1). It is possible that inclusion of sensitivity weighting or non-linear normalizations could have positive effects on the performance of the method. There are many possibilities on how to include sensitivities of different methods, which might come with new challenges and therefore this could fill a study for itself.

To conclude this outlook, I would like to propose an extension of the implementation of joint minimum entropy constraints. The original formulation by Zhdanov et al. (2022) was already extended by additional method weighting and smoothing in the frame of this research project. The latter involved the introduction of a first-order smoothing operator that currently has the same weight on all internal boundaries (see Listing 3.2, Figure 3.3). It could be possible to weight each internal boundary based on some roughness measure of the JME stabilizer map (see Figure 5.15) or on an adjusted MEG formulation. This could be interpreted as a combination of the SCCI approaches of Zhdanov et al. (2022) and Skibbe et al. (2021) and has the potential to introduce partially decoupled and therefore sharper boundaries along joint entropy anomalies. Of course, this combination of both approaches would most likely be not trivial but has the potential for major improvements. It would also be a step towards combining existing joint inversion approaches which is, in my opinion, something that currently is lacking in this field and should be investigated further in the future.

A

Appendix

Contents

This Appendix consists of a short description of the associated GitHub repository as well as tables that include the necessary inversion parameters to reproduce the results of Chapter 4 (Synthetic study) and 5. Furthermore, additional Figures of the 3D JME inversion results of Chapter 5 (Field study: Rockeskyller Kopf) are provided in section A.4.

A.1 Availability of data and scripts

This thesis project has a complementary GitHub repository under: https://github.com/ZiegAnt/APG-MSc-Project-Ziegon.

This directory consists of all Python scripts that are necessary to produce the figures of this work. It also contains the processed field data alongside the synthetic data, as well as field data inversion outputs that can be visualized using either PyVista (Sullivan and Kaszynski, 2019) or ParaView (Ahrens et al., 2005).

The directory is currently private as data and code are not published yet. Access to the repository can be requested at: anton.ziegon@rwth-aachen.de

A.2 Parameters of synthetic data study

Table A.1: Inversion parameters of the synthetic data study.

(a) Figures 4.3 to 4.10.

Figure	Parameter	Value
Figure 4.3	λ_{ERT}	2
	λ_{SRT}	6
	secNodes	1
Figure 4.4	λ_{ERT}	10^{-5}, 10^{-3}, 10^{-1}
	a_{ERT}	0, 50, 200
	q	1
	β	10^{-10}
Figure 4.5	λ_{SRT}	10^{-5}, 10^{-3}, 10^{-1}
	a_{SRT}	0, 25, 100
	q	1
	β	10^{-10}
	secNodes	1
Figure 4.6	λ_{ERT}	10^{-7}, 10^{-5}, 10^{-3}
	a_{ERT}	0, 50, 200
	q	1
	β	10^{-10}
Figure 4.7	λ_{SRT}	10^{-7}, 10^{-5}, 10^{-3}
	a_{SRT}	0, 25, 100
	q	1
	β	10^{-10}
	secNodes	1
Figure 4.8	λ_{ERT}	10^{-5}, 10^{-3}, 10^{-1}
	a_{ERT}	0, 50, 200
	q	2
	β	10^{-10}
Figure 4.9	λ_{SRT}	10^{-5}, 10^{-3}, 10^{-1}
	a_{SRT}	0, 25, 100
	q	2
	β	10^{-10}
	secNodes	1
Figure 4.10	λ_{ERT}	10^{-7}, 10^{-5}, 10^{-3}
	a_{ERT}	0, 50, 200
	q	2
	β	10^{-10}

(b) Figures 4.11 to 4.15.

Figure	Parameter	Value
Figure 4.11	λ_{SRT}	10^{-7}, 10^{-5}, 10^{-3}
	a_{SRT}	0, 25, 100
	q	2
	β	10^{-10}
	secNodes	1
Figure 4.12	λ_{ERT}	0.003
	λ_{SRT}	0.01
	a_{ERT}	15
	a_{SRT}	90
	q	1
	β	10^{-10}
	secNodes	1
Figure 4.13	λ_{ERT}	0.003
	λ_{SRT}	0.01
	a_{ERT}	15
	a_{SRT}	90
	q	2
	β	10^{-10}
	secNodes	1
Figure 4.14	λ_{ERT}	$5 \cdot 10^{-6}$
	λ_{SRT}	$5 \cdot 10^{-4}$
	a_{ERT}	20
	a_{SRT}	100
	q	1
	β	10^{-10}
	secNodes	1
Figure 4.15	λ_{ERT}	$5 \cdot 10^{-6}$
	λ_{SRT}	$5 \cdot 10^{-4}$
	a_{ERT}	20
	a_{SRT}	100
	q	2
	β	10^{-10}
	secNodes	1

A.3 Parameters of field data study

Table A.2: Inversion parameters of the field data study at Rockeskyller Kopf.

(a) Figures 5.5 to 5.9.

Figure	Parameter	Value
Figure 5.5	*For all lines*	
	λ	10
	paraMaxCellSize	2
	paraDepth	40
	quality	33.6
Figure 5.6	λ	15
	dPhi	0.1
Figure 5.7	λ	10
	dPhi	0.1
	startModel	1e-4
	Parameter range	[0,0.15]
Figure 5.8	λ_{ME1}	0.005
	λ_{ME2}	0.01
	a_{ME1}	35
	a_{ME2}	25
	β	10^{-10}
Figure 5.9	λ_{ME1}	0.05
	λ_{ME2}	0.01
	a_{ME1}	50
	a_{ME2}	60
	β	10^{-10}

(b) Figures 5.10 to 5.14.

Figure	Parameter	Value
Figure 5.10	λ_{ERT}	0.005
	λ_{MAG}	0.05
	a_{ERT}	35
	a_{MAG}	50
	mw_{ERT}	1, 100
	mw_{MAG}	1, 100
	q	1
	β	10^{-10}
Figures 5.11 to 5.14	$\lambda_{\mathrm{JME_{ERT}}}$	0.005
	$\lambda_{\mathrm{JME_{MAG}}}$	0.05
	$a_{\mathrm{JME_{ERT}}}$	35
	$a_{\mathrm{JME_{MAG}}}$	50
	$mw_{\mathrm{JME_{ERT}}}$	10
	$mw_{\mathrm{JME_{MAG}}}$	1
	q	1
	β	10^{-10}

A.4 Additional figures for field data study

A.4.1 3D Mesh

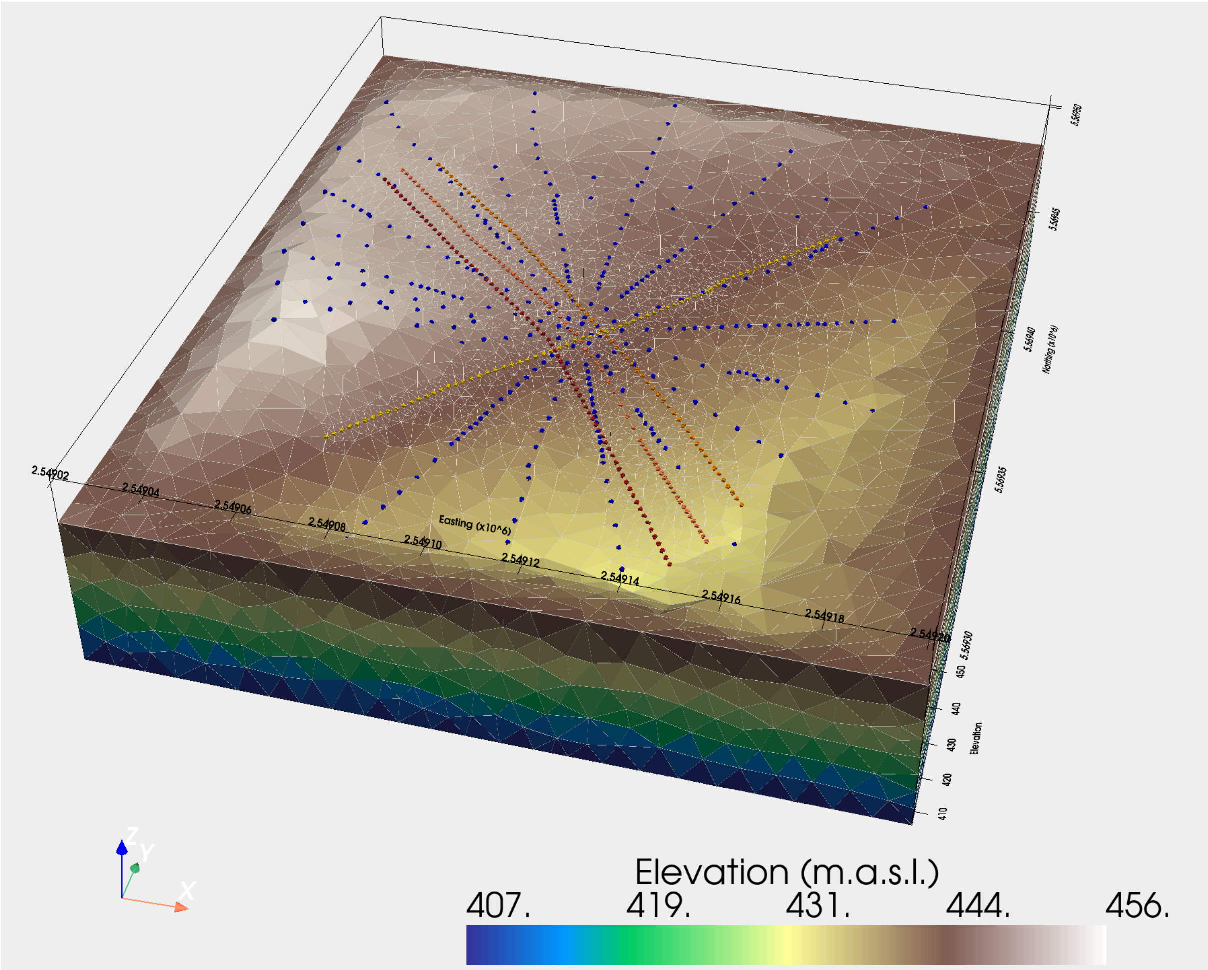

Figure A.1: 3D mesh that is used for the 3D inversions. The model is colored by the elevation of the cell centers. Created with PyVista (Sullivan and Kaszynski, 2019).

A.4.2 Joint ERT and magnetic results

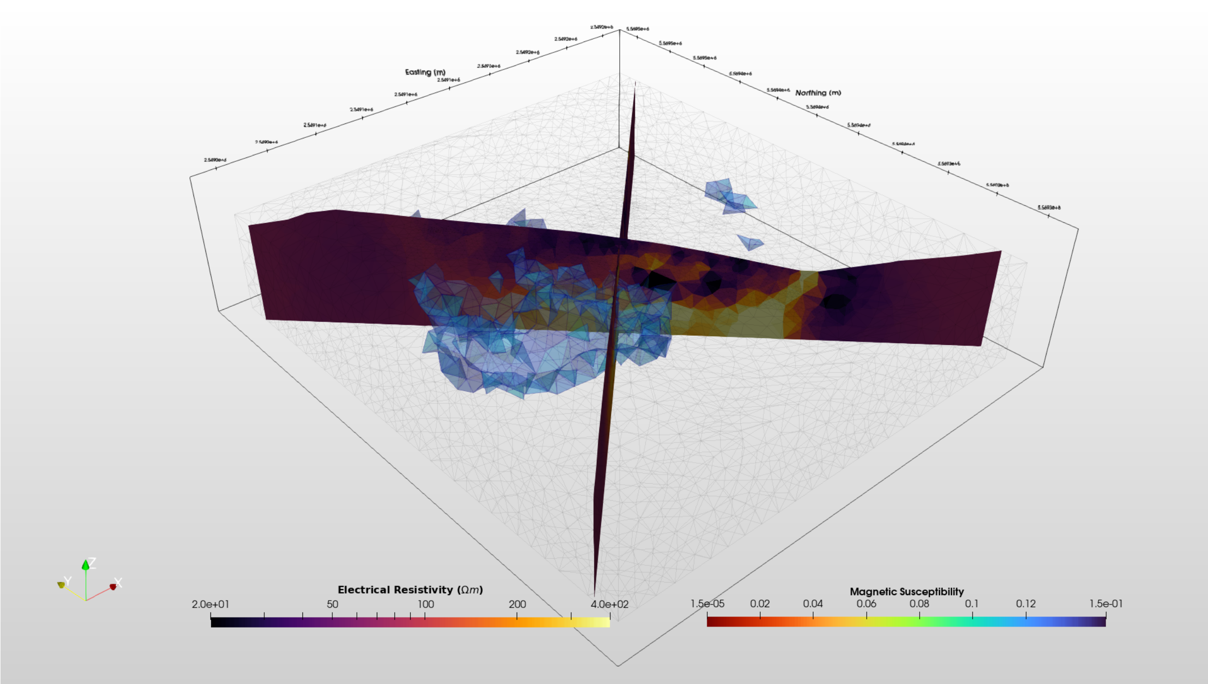

(a) View towards northeast.

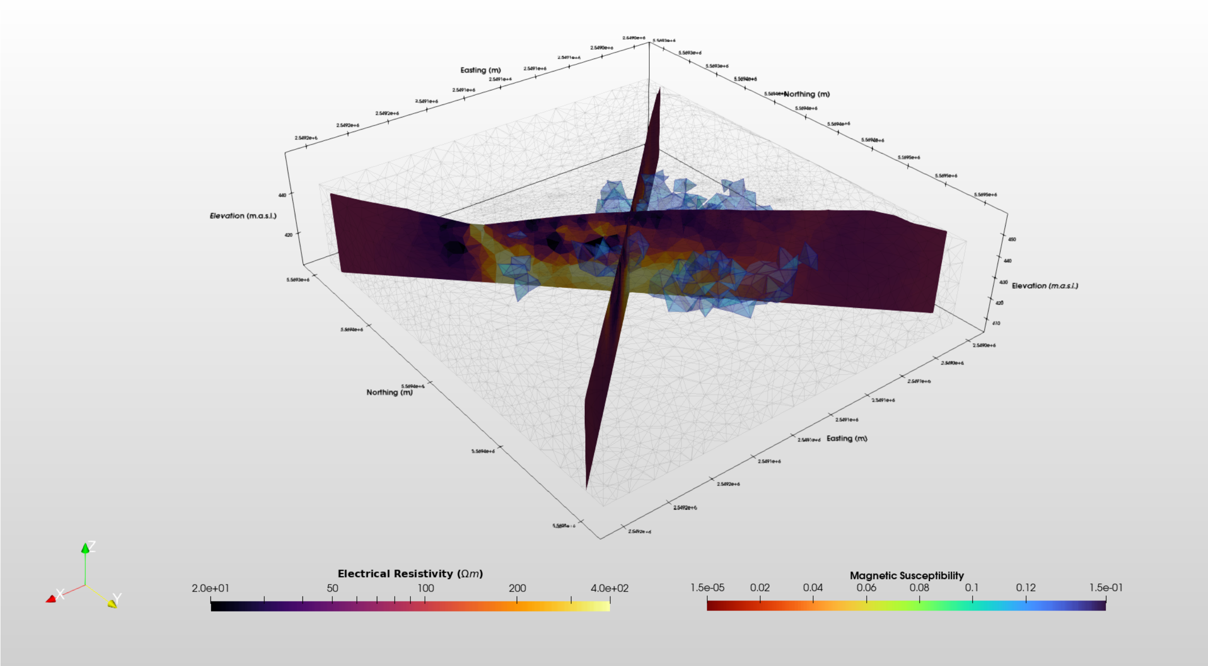

(b) View towards southwest.

Figure A.2: 3D view of JME inversion results. Cross sections show slices of the 3D resistivity volume and white-grey volume indicates the magnetic anomaly of a susceptibility of higher than 0.12. Figures created with ParaView (Ahrens et al., 2005).

A.4.3 Depth slices of JME results

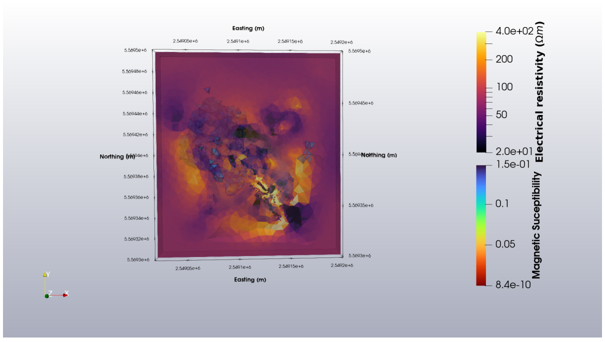

(a) Depth slice at Z = 440 m.a.s.l.

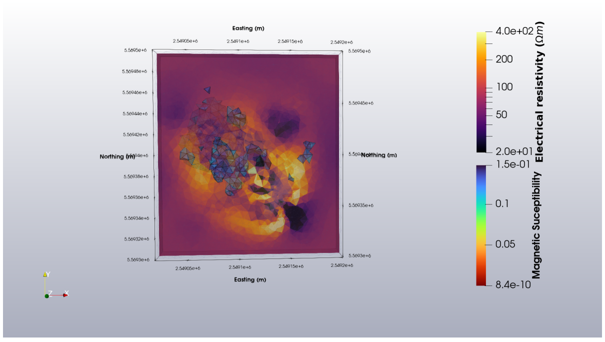

(b) Depth slice at Z = 430 m.a.s.l.

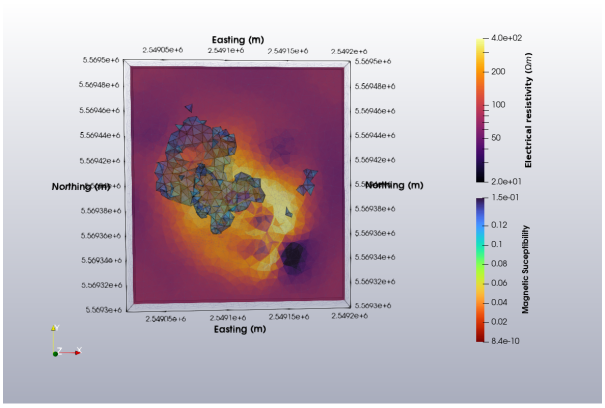

(c) Depth slice at Z = 420 m.a.s.l.

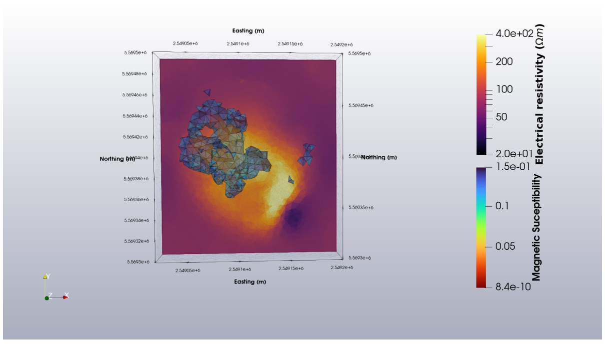

(d) Depth slice at Z = 410 m.a.s.l.

Figure A.3: Depth slices of 3D resistivity volume. The magnetic anomaly is represented as a semi-transparent volume. Figures created with ParaView (Ahrens et al., 2005).

References

Ahrens, J., Geveci, B., and Law, C.: ParaView: An End-User Tool for Large Data Visualization, in: Visualization Handbook, Elesvier, ISBN 978-0123875822, 2005.

Bergmann, P., Ivandic, M., Norden, B., Rücker, C., Kiessling, D., Lüth, S., Schmidt-Hattenberger, C., and Juhlin, C.: Combination of seismic reflection and constrained resistivity inversion with an application to 4D imaging of the CO2 storage site, Ketzin, Germany, Geophysics, 79, B37–B50, URL https://doi.org/10.1190/geo2013-0131.1, 2014.

Boxberg, M.: Magnetische Kartierung zur Bestimmung der Lage des Phonolith Diatrems bei Rockeskyll, Westeifel: Bachelorarbeit, Ruhr-Universität-Bochum, 2011.

Caticha, A.: Information and entropy, in: AIP conference proceedings, vol. 954, pp. 11–22, American Institute of Physics, URL https://doi.org/10.1063/1.2821253, 2007.

Constable, S. C., Parker, R. L., and Constable, C. G.: Occam's inversion: A practical algorithm for generating smooth models from electromagnetic sounding data, Geophysics, 52, 289–300, URL https://doi.org/10.1190/1.1442303, 1987.

Eilhard, M.: Die Entstehung und Förderung der Auswürflinge des Kyller Kopfes: Sanidinite: Bachelorarbeit, Ruhr-Universität-Bochum, 2009.

Eilhard, N.: Genese der Sanidin-Megakristalle aus den quartären Vulkanfeldern der Eifel, Deutschland: Dissertation, Ruhr-Universität-Bochum, 2018.

Gallardo, L. A.: Multiple cross-gradient joint inversion for geospectral imaging, Geophysical Research Letters, 34, URL https://doi.org/10.1029/2007GL030409, 2007.

Gallardo, L. A. and Meju, M. A.: Joint two-dimensional DC resistivity and seismic travel time inversion with cross-gradients constraints, Journal of Geophysical Research: Solid Earth, 109, URL https://doi.org/10.1029/2003JB002716, 2004.

Gallardo, L. A., Meju, M. A., and Pérez-Flores, M. A.: A quadratic programming approach for joint image reconstruction: mathematical and geophysical examples, Inverse problems, 21, 435, URL https://doi.org/10.1088/0266-5611/21/2/002, 2005.

Gilberti, T.: Integration eines aus photogrammetrischen Messungen erstellten Modells der Oberflächentopographie in bestehende Integration eines aus photogrammetrischen Messungen erstellten Modells der Oberflächentopographie in bestehende geophysikalische Modelle eines vulkanischen Diatrems am Rockeskyller Kopf: Bachelorarbeit, Ruhr-Universität-Bochum, 2020.

Gray, R. M.: Entropy and information theory, URL https://ee.stanford.edu/~gray/it.pdf, 2013.

Günther, T. and Rücker, C.: A new joint inversion approach applied to the combined tomography of DC resistivity and seismic refraction data, in: Symposium on the Application of Geophysics to Engineering and Environmental Problems 2006, pp. 1196–1202, Society of Exploration Geophysicists, URL https://doi.org/10.4133/1.2923578, 2006.

Günther, T., Rücker, C., Spitzer, K., et al.: 3-d modeling and inversion of DC resistivity data incorporating topography-Part II: Inversion, Geophys. J. Int, 166, 506–517, 2006.

Gupta, S.: Hidden layer problem in seismic refraction work, Geophysical Prospecting, 25, 385–387, URL https://doi.org/10.1111/j.1365-2478.1975.tb01550.x, 1977.

Haber, E. and Oldenburg, D.: Joint inversion: a structural approach, Inverse problems, 13, 63, URL https://doi.org/10.1088/0266-5611/13/1/006, 1997.

Hauburg, N.: 3D-refraktionstomographische Untersuchung eines vulkanischen Diatrems am Rockeskyller Kopf: Masterarbeit, Ruhr-Universität-Bochum, 2016.

Hinze, W. J., Von Frese, R. R., Von Frese, R., and Saad, A. H.: Gravity and magnetic exploration: Principles, practices, and applications, Cambridge University Press, 2013.

Holstein, H., Sherratt, E. M., and Reid, A. B.: Gravimagnetic field tensor gradiometry formulas for uniform polyhedra, in: 2007 SEG Annual Meeting, OnePetro, URL https://onepetro.org/SEGAM/proceedings/SEG07/All-SEG07/SEG-2007-0750/95584, 2007.

Hopmann, P.: Spuren eines Phonolithdurchbruches bei Rockeskyll in der Eifel, Zent. Mineral., Stutt., 35, 565, 1914.

Johnson, T. C. and Wellman, D.: Accurate modelling and inversion of electrical resistivity data in the presence of metallic infrastructure with known location and dimension, Geophysical Journal International, 202, 1096–1108, URL https://doi.org/10.1093/gji/ggv206, 2015.

Jordi, C., Doetsch, J., Günther, T., Schmelzbach, C., Maurer, H., and Robertsson, J. O.: Structural joint inversion on irregular meshes, Geophysical Journal International, 220, 1995–2008, URL https://doi.org/10.1093/gji/ggz550, 2020.

Kearey, P., Brooks, M., and Hill, I.: An introduction to geophysical exploration, vol. 4, John Wiley & Sons, 2002.

Loke, M. H. and Dahlin, T.: A comparison of the Gauss–Newton and quasi-Newton methods in resistivity imaging inversion, Journal of applied geophysics, 49, 149–162, URL https://doi.org/10.1016/S0926-9851(01)00106-9, 2002.

Lowrie, W. and Fichtner, A.: Fundamentals of geophysics, Cambridge university press, 2020.

Maack, S., Küttenbaum, S., Bühling, B., and Niederleithinger, E.: Low frequency ultrasonic dataset for pulse echo object detection in an isotropic homogeneous medium as reference for heterogeneous materials in civil engineering, Data in Brief, 42, 108 235, URL https://doi.org/10.1016/j.dib.2022.108235, 2022.

Marty, P., Boehm, C., and Fichtner, A.: Full-Waveform Inversion of Geological Structures in the Human Brain, in: AGU Fall Meeting Abstracts, vol. 2021, pp. S15E–0291, URL https://ui.adsabs.harvard.edu/abs/2021AGUFM.S15E0291M/abstract, 2021.

Menke, W.: Geophysical data analysis: Discrete inverse theory, Academic press, 2018.

Mertes, H.: Aufbau und genese des Westeifeler Vulkanfeldes, 9, Institut für Geologie der Ruhr-Universität-Bochum, 1983.

Moorkamp, M., Heincke, B., Jegen, M., Roberts, A. W., and Hobbs, R. W.: A framework for 3-D joint inversion of MT, gravity and seismic refraction data, Geophysical Journal International, 184, 477–493, URL https://doi.org/10.1111/j.1365-246X.2010.04856.x, 2011.

Moorkamp, M., Lelièvre, P. G., Linde, N., and Khan, A.: Integrated imaging of the earth: Theory and applications, vol. 218, John Wiley & Sons, 2016.

Mues, H.: Weiterführende magnetische Kartierung zur Ortung des Phonolith-Diatrems bei Rockeskyll, Westeifel: Bachelorarbeit, Ruhr-Universität-Bochum, 2013.

Okpoli, C. C. et al.: Sensitivity and resolution capacity of electrode configurations, International Journal of Geophysics, 2013, URL https://doi.org/10.1155/2013/608037, 2013.

Plumpe, N.: Geoelektrische Tomographie eines Diatrems am Rockeskyller Kopf und Reinterpretation eines seismischen Profils: Bachelorarbeit, Ruhr-Universität-Bochum, 2015.

Redlands, C. E. S. R. I.: ArcGIS Desktop: Release 10, 2011.

Rücker, C., Günther, T., and Wagner, F. M.: pyGIMLi: An open-source library for modelling and inversion in geophysics, Computers & Geosciences, 109, 106–123, URL https://doi.org/10.1016/j.cageo.2017.07.011, 2017.

Schmincke, H.-U.: Vulkane der Eifel: Aufbau, Entstehung und heutige Bedeutung, Springer, URL https://doi.org/10.1007/s00445-010-0380-9, 2009.

Schneider, D.: Oberflächennahe Reflexionsseismik über einem Diatrem am Rockeskyller Kopf: Bachelorarbeit, Ruhr-Universität-Bochum, 2017.

Shannon, C. E.: A mathematical theory of communication, The Bell System Technical Journal, 27, 379–423, URL https://doi.org/10.1002/j.1538-7305.1948.tb01338.x, 1948.

Shaw, C. S., Woodland, A. B., Hopp, J., and Trenholm, N. D.: Structure and evolution of the Rockeskyllerkopf Volcanic Complex, West Eifel Volcanic Field, Germany, Bulletin of volcanology, 72, 971–990, URL https://doi.org/10.1007/s00445-010-0380-9, 2010.

Skibbe, N., Günther, T., and Müller-Petke, M.: Improved hydrogeophysical imaging by structural coupling of 2D magnetic resonance and electrical resistivity tomography, Geophysics, 86, WB77–WB88, URL https://doi.org/10.1190/geo2020-0593.1, 2021.

Steiner, M., Wagner, F. M., Maierhofer, T., Schöner, W., and Flores Orozco, A.: Improved estimation of ice and water contents in Alpine permafrost through constrained petrophysical joint inversion: The Hoher Sonnblick case study, Geophysics, 86, WB61–WB75, URL https://doi.org/10.1190/geo2020-0592.1, 2021.

Sullivan, B. and Kaszynski, A.: PyVista: 3D plotting and mesh analysis through a streamlined interface for the Visualization Toolkit (VTK), Journal of Open Source Software, 4, 1450, doi: 10.21105/joss.01450, URL https://doi.org/10.21105/joss.01450, 2019.

Tu, X. and Zhdanov, M. S.: Joint Gramian inversion of geophysical data with different resolution capabilities: Case study in Yellowstone, Geophysical Journal International, 226, 1058–1085, URL https://doi.org/10.1093/gji/ggab131, 2021.

Wagner, F. M. and Uhlemann, S.: An overview of multimethod imaging approaches in environmental geophysics, Advances in Geophysics, 62, 1–72, URL https://doi.org/10.1016/bs.agph.2021.06.001, 2021.

White, J. D. and Ross, P.-S.: Maar-diatreme volcanoes: a review, Journal of Volcanology and Geothermal Research, 201, 1–29, URL https://doi.org/10.1016/j.jvolgeores.2011.01.010, 2011.

Zhdanov, M. S.: Geophysical inverse theory and regularization problems, vol. 36, Elsevier, 2002.

Zhdanov, M. S.: Inverse theory and applications in geophysics, vol. 36, Elsevier, 2015.

Zhdanov, M. S., Tu, X., and Čuma, M.: Cooperative inversion of multiphysics data using joint minimum entropy constraints, Near Surface Geophysics, 20, 623–636, URL https://doi.org/10.1002/nsg.12203, 2022.